Isotopic fingerprinting (Sr-Nd-Hf-Os-C-O) of mantle source regions to kimberlite magmatism beneath the eastern Superior craton, Canada

N. B. Brand

Student No.: 481655

Supervised by: Prof. S. Tappe and Prof. L. Ashwal

School of Geosciences,
University of the Witwatersrand,
Johannesburg,
South Africa,
Private Bag 3 2050 Wits,
South Africa
Tel: +27 (0)11 717 6547
Email: nats0203@gmail.com

A Dissertation submitted to the Faculty of Science, University of the Witwatersrand, in fulfilment of the requirements for the degree of Master of Science.

Johannesburg, 2016

Contents

Declaration

I, Natalie Bronwyn Brand (Student number: 481655) am a student registered for the degree of M.Sc. Geology during the academic period 2014-2015.

I hereby declare the following:

- I am aware that plagiarism (the use of someone else's work without their permission and/or without acknowledging the original source) is wrong.
- I confirm that the work submitted for assessment for the above degree is my own unaided work except where I have explicitly indicated otherwise.
- I have followed the required conventions in referencing the thoughts and ideas of others.
- I understand that the University of the Witwatersrand may take disciplinary action against me if there is a belief that this is not my own unaided work or that I have failed to acknowledge the source of the ideas or words in my writing.

Signature:

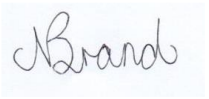

Date:

25 May 2016

ABSTRACT

The northern sector of the Archaean Superior Craton has been a significant region for diamond exploration, hosting numerous alkaline intrusions of Proterozoic age. The focus of this study is on two kimberlite fields that are situated in eastern Canada, 400 km apart. These are the diamond-rich Renard pipes and dykes, and the Wemindji field, consisting of barren sheeted dykes. The nine diamondiferous Renard igneous bodies were emplaced between 655-630 Ma in the eastern sector of Laurentia into Archaean metamorphic rocks. Thin, subhorizontal Wemindji kimberlite sills were emplaced into granitic gneiss terrane of the Superior Province near Wemindji, Quebec, at 629 ± 29 Ma, along the inferred extension of the Kapuskasing Structural Zone. These kimberlite fields are grouped with the extensive Late Neoproterozoic magmatism of ultramafic and volatile-rich character, which is said to be associated with the breakup of Rodinia. Despite overall compositional similarity of the studied magmatic kimberlites, the material from Renard has higher concentrations of SiO_2, Al_2O_3, MgO, and K_2O, which reflects higher phlogopite abundances. The Wemindji sills show higher CaO concentrations due to high primary carbonate contents. Renard and Wemindji kimberlite incompatible trace element distributions are similar, with differences in Cs, Rb, and Sr corresponding to variable modal mineralogy. The initial $^{87}Sr/^{86}Sr$ ratios for the Renard kimberlites range between 0.70241 and 0.70765, while the Wemindji kimberlites have values between 0.70361 and 0.70442. Initial ε_{Nd} values for the Renard kimberlites lie between +1.2 and +4.6, whereas the Wemindji kimberlite sills range between +0.2 and +4.8. Initial ε_{Hf} values for the Renard kimberlites lie between +1.7 and +6.3, whereas the Wemindji kimberlite sills yielded values between +1.1 and +6.5. The overlapping Sr-Nd-Hf isotope compositions of these kimberlite suites indicate melt derivation from moderately depleted mantle sources. Osmium isotope compositions fall at the unradiogenic end for global kimberlites, with initial $^{187}Os/^{188}Os$ ratios ranging between 0.11539 and 0.12620 for Renard kimberlites, and between 0.11078 and 0.11729 for Wemindji kimberlites, with Os concentrations all below 1.3 ppb. These Os values suggest that an additional input from the CLM (i.e., ancient refractory cratonic peridotite), which is not reflected in the Hf and Nd radiogenic isotopes, is

required. Both kimberlite suites depict mantle $\delta^{13}C$ values (ca. -6 to –4 ‰), with evidence of hydrothermal alteration in the $\delta^{18}O$ values (between 10 and 20 ‰ relative to SMOW). Production of an isotopically depleted melt occurred during the breakaway of Laurentia from Rodinia. Wemindji sits on the inferred extension of the Kapuskasing Structural Zone, which is suggested to have been a short-lived reactivated translithospheric rift-like feature, promoting CO_2-rich melting conditions during the Late Neoproterozoic. The data from this study suggest that this ascending sublithospheric depleted melt component (more CO_2-rich beneath Wemindji) interacted with a maximum input volume of 5% of the MARID-enriched CLM beneath the eastern Superior craton, and between 2% and 30% of ancient refractory cratonic peridotite. The lack of significant diamond in the Wemindji kimberlite dykes could be due to the resorption of the potential diamond in the CO_2-rich kimberlite melt.

Acknowledgements

Professor Sebastian Tappe (UJ) is gratefully acknowledged for the genesis of this project, along with consistent guidance and supervision throughout the workings. Professor Lewis Ashwal (Wits) is also acknowledged for his support and supervision of the project. Furthermore, Prof. Dr. Andreas Stracke (WWU) and Dr. David van Acken (Universität Bonn) are recognised for their instruction and assistance throughout laboratory work carried out in Germany. The stable C and O isotopic analysis by Prof. Dr. Harald Strauß is (WWU) greatly appreciated. Dr. Katie Smart (Wits) is also recognised for her explanation and discussion of C and O stable isotopic modelling. Samples from the Renard kimberlite suite used in this project were provided by John Armstrong (Vice President Mineral Resources Lucara Diamond Corp.) and Michael Patterson (Department of Earth and Planetary Science, McGill University). Samples from the Wemindji kimberlite suite used in this project were provided by Roger H. Mitchell (Department of Geology, Lakehead University). Gratitude is extended to Professor Allan Wilson and Marlin Patchappa for conducting XRF and ICP-MS analyses, as well as Caiphas Majola for the cutting and polishing of thin sections at the University of the Witwatersrand. The University of the Witwatersrand and the University of Johannesburg are acknowledged for the use of crushing and milling labs in the preparation stages of the project. This project would not have been possible without the financial support from the National Research Foundation of South Africa and the University of the Witwatersrand.

Gratitude is also extended to Prof. Allan Wilson and Dr. Hugh O'Brien for the examination and constructive criticism of this dissertation.

List of Figures and Tables

(Tappe *et al*., 2011; Gaffney *et al*., 2007) and other Canadian kimberlite dyke occurrences (Tappe *et al*., 2014; Agashev *et al*., 2008). All concentrations are normalised to the primitive mantle values given in Palme & O'Neill (2003).

Figure 6: Bulk rock Ba/Nb vs La/Nb for the Renard and Wemindji hypabyssal kimberlites. Fields are plotted for South African kimberlites (Group-1) and South African orangeites (previously known as Group-II kimberlites), along with the dashed lines separating these two kimberlite fields in a broader sense (all taken from Becker and Le Roex, 2006). The field for Greenland-Labrador ultramafic dykes is also shown for comparison (Tappe *et al*., 2008, 2011).

Figure 7: HSE compositions for Renard and Wemindji magmatic kimberlites, in comparison to mantle peridotite xenoliths from Somerset Island, Arctic Canada (Irvine *et al*., 2003) and West Greenland (Wittig *et al.*, 2010) as well as metasomatic mantle-derived MARID xenoliths from South Africa (Maier *et al*., 2012). Chondrite normalising values from Horan *et al*. (2003) and Fischer-Gödde *et al*. (2010).

Figure 8: A-B) Sr-Nd and C-D) Nd-Hf isotope diagrams for magmatic kimberlites from Renard and Wemindji. Global ocean island basalts (OIBs) (Stracke, 2012); Southern African kimberlites (Nowell *et al*., 2004); Southern African orangeites (Nowell *et al*., 2004; Coe *et al*., 2008); global kimberlites (Paton *et al*., 2009 - India; Kopylova *et al*., 2009 - Jericho; Yang *et al*., 2009 - China; Carlson *et al*., 2006 - Siberia; Yaxley *et al*., 2013 – Antarctica; Tappe *et al*., 2013 – Slave craton); "Laurentian" Neoproterozoic kimberlites, carbonatites and UMLs (Gaffney *et al*., 2007; Tappe *et al*., 2011 - West Greenland; Tappe *et al*., 2014 – Baffin Island; Tappe *et al*., 2007, 2008 – Labrador). Mantle array (red line) after Chauvel *et al*. (2008). The yellow star indicates an inferred low-degree carbonate-rich melt component of the convecting upper mantle that was widespread beneath cratonic Laurentia during the Late Neoproterozoic (Tappe *et al*., 2011).

Figure 9: Osmium isotope composition and concentration of Renard and Wemindji magmatic kimberlites, compared to global mantle-derived peridotite and eclogite/pyroxenite xenoliths (Meisel *et al*., 2001 – USA, Mexico, Alaska, Hawaii, Australia, Africa; Irvine *et al*., 2003 - Somerset Island peridotite xenoliths (Canada); Carlson *et al*., 2007 - Brazilian peridotite xenoliths; Aulbach *et al*., 2009 - eclogite and pyroxenite xenoliths (Slave Craton*)*; Wittig *et al*., 2010 - peridotite xenoliths (West Greenland); global magmatic kimberlites (Carlson *et al*., 2007 - Brazil; Rao *et al*., 2013 - India); Ugandan kamafugites (Rosenthal *et al*., 2009); olivine melilitites (Janney *et al*., 2002); ocean island basalts (OIBs) (Debaille *et al*., 2009 - Iceland; Jackson & Shirey, 2011 - Samoa). Osmium isotope compositions of xenoliths were

PREAMBLE

This document was originally prepared in manuscript format with the intention of journal submission to Chemical Geology. It includes a body of work with multiple co-authors and contributions as follows:

- Prof. Sebastian Tappe – Supervision of the project and performance U-Pb geochronological measurement.
- Prof. Lewis Ashwal – Co-supervision of the project.
- Prof. Andreas Stracke – Measurement of Sr-Nd-Hf isotopes.
- Dr. David Van Acken – Measurement of HSE and Os isotopes.
- Prof. Harald Strauss – Measurement of C and O isotopes.
- Prof. Fu-Yuan Wu – Assistance with U-Pb geochronology.

As Prof. Sebastian Tappe and Prof. Lewis Ashwal were supervisors of this project, they provided the most conversation and assistance with interpretation of data in this body of work. The U-Pb geochronological measurement was performed solely by Prof. Sebastian Tappe and Prof. Fu-Yuan Wu, in conjunction with a different project Prof. Tappe was simultaneously carrying out. The remaining authors on this list provided assistance purely with the analytical methods, along with minor data interpretation and advice directly to me.

A basic breakdown of analytical and intellectual contribution concerning the analysis of the data acquired is provided below:

		Contribution	
Analysis	Contributor	Analysis	Interpretation
Sample powder preparation	N. Brand	100%	-
Major Elements	N. Brand	10%	70%
	S. Tappe		30%
	Earth Lab (Wits)	90%	
Trace Elements	N. Brand		70%
	S. Tappe		30%
	Earth Lab (Wits)	100%	
Sr-Nd-Hf	N. Brand	50%	50%
	S. Tappe		38%
	L. D. Ashwal		5%
	A. Stracke	50%	8%
Os	N. Brand	30%	50%
	S. Tappe		25%
	D. van Acken	70%	25%
C-O	N. Brand		60%
	S. Tappe		40%
	H. Strauss	100%	
U-Pb	S. Tappe	50%	100%
	F.Y. Wu	50%	

Overview

Kimberlites are volatile-rich, silica-poor ultramafic igneous rocks that occur as hypabyssal intrusions and volcanic pipes and rarely as extrusive lavas (Mitchell, 1986, Dawson, 1994). Group I kimberlites are defined as olivine-rich rocks, crystallised from volatile-rich melts, and containing fragments of crustal and mantle material, set in a matrix of carbonates, olivine, phlogopite, spinel, ilmenite, perovskite, apatite and serpentine, along with other accessory phases (Mitchell, 1995). Group II kimberlites, generally referred to as orangeites (Mitchell, 1995), contain higher phlogopite and therefore K_2O contents, as well as containing K-Ba titanites, and typically K-richterite and sanidine (Mitchell, 1995). Group I kimberlites have radiogenic Nd isotope compositions and unradiogenic Sr isotope compositions comparable to ocean island basalts, while orangeites depict less

radiogenic Nd and more radiogenic Sr isotope compositions (Smith, 1983; Nowell *et al*., 2004).

Kimberlite magma generation has long been a topic of deliberation among scientists and economically-oriented groups. Kimberlites are characteristically enriched in incompatible trace elements (Le Roux *et al*., 2003). Suggested mechanisms of generation include subduction-related melting, mantle plume links, as well as continental rifting processes (Heaman *et al*., 2004; Tappe *et al*., 2012, and references therein). Besides being potential economic entities by transporting diamonds to the Earth's surface, kimberlites give insight into melting processes within deep Earth mantle reservoirs, which are commonly believed to be linked to large-scale tectonic processes (Jelsma *et al*., 2009; Tappe *et al*., 2013). It has also been suggested that kimberlites are derived from plumes at the core mantle boundary (Torsvik *et al*., 2010). Tracer isotope and geochronological data are therefore crucial in the determination of the deep Earth processes involved in the origin of these magmas.

According to Mitchell (2008), hypabyssal kimberlites are mineralogically and geochemically similar on a worldwide basis, irrespective of variable emplacement ages and eruption on distinct cratons. They also provide the best material for understanding the nature of kimberlite magma prior to magmatic degassing and the formation of pyroclastic kimberlite facies (Mitchell, 2008; Kjarsgaard *et al*., 2009; Brooker *et al*., 2011).

There is a suggested relationship between kimberlite bulk composition and possible diamond grade, where economically diamondiferous kimberlites contain low bulk iron and titanium contents (Patterson *et al*., 2009, and references therein). However, such claims have been challenged by Mitchell & Tappe (2010) due to inconsistencies of the above geochemical systematics.

Aims

- To geochemically contrast and compare kimberlites from Wemindji and Renard (Superior craton, Quebec, Canada).
- To determine possible kimberlite magma source(s).

- To geochemically constrain the reasons for diamond dissimilar grades of the Renard kimberlites and the barren Wemindji kimberlites.
- To improve emplacement age data for these kimberlites and hence better constrain tectonomagmatic processes that affected eastern Laurentia during the Late Neoproterozoic.

Hypotheses

Isotopic signatures should yield evidence of a depleted mantle source for the ultimate origin of these kimberlite magmas. Furthermore, the degree of melt interaction with enriched and ultra-depleted cratonic mantle can be evaluated by geochemical means.

The lack of macrodiamonds in the Wemindji kimberlites is due to their evolved nature, as stated in Zurevinski & Mitchell (2011). Alternatively, Wemindji and Renard kimberlite magmas may have passed through contrasting (i.e., barren versus diamondiferous) cratonic mantle domains of the eastern Superior craton.

Methodology

Ten samples from each locality discussed (20 samples in total) were examined petrologically, geochemically and geochronologically. A diverse range of analytical methods are proposed during the course of registration at the University of the Witwatersrand, Johannesburg, as well as at the Westfaelische Wilhelms University Münster, Germany, and the Steinmann-Institut, Universität Bonn.

Petrology:

- Polished thin section preparation, analysis, description and imaging on samples from each locality (University of the Witwatersrand).

Geochemistry:

- Laser ablation inductively coupled plasma mass spectrometry (LA-ICP-MS) for trace element analysis (Westfaelische Wilhelms Universität Münster).

- X-Ray Fluorescence (XRF) for major and minor element analysis (University of the Witwatersrand).
- ICP-MS for trace element analysis (University of the Witwatersrand).
- CS-Analyser for CO_2 quantification (Westfaelische Wilhelms Universität Münster)
- Sr-Nd-Hf isotope analysis (Westfaelische Wilhelms Universität Münster)
- Os isotope analysis (Steinmann-Institut, Universität Bonn)
- C and O isotope analysis (Westfaelische Wilhelms Universität Münster).

Geochronology:

- In-situ U/Pb dating of perovskite (SIMS and LA-ICPMS) (Chinese Academy of Sciences).

A comparative study of these analyses with literature data was then conducted, followed by full data integration and interpretation, geochemical modelling, tectonomagmatic modelling and manuscript/dissertation preparation.

Preamble references

Dawson, J.B. (1994). Quaternary kimberlitic volcanism on the Tanzania Craton. *Contribution to Mineral Petrology,* 116, 473-485.

Brooker, R.A., Sparks, R.S.J., Kavanagh, J.L. and Field, M. (2011). The volatile content of hypabyssal kimberlite magmas: some constraints from experiments on natural rock compositions. *Bulletin of Volcanology,* 73, 959-981.

Jelsma, H., Barnett, W., Richards, S., Lister, G. (2009). Tectonic setting of kimberlites. *Lithos* 112, 155–165.

Kjarsgaard, B.A., Pearson, D.G., Tappe, S., Nowell, G.M., Dowall, D. (2009). Geochemistry of hypabyssal kimberlites from Lac de Gras, Canada: comparisons to a global database and applications to the parent magma problem. *Lithos* 112, 236–248.

Heaman, L.M., Kjarsgaard, B.A. and Creaser, R.A. (2004). The temporal evolution of North American kimberlites. *Lithos* 76, 377-379.

Le Roex, A. P., Bell, D. R. & Davis, P. (2003). Petrogenesis of Group I kimberlites from Kimberley, South Africa: evidence from bulk rock geochemistry. *Journal of Petrology* 44, 2261-2286.

Mitchell, R.H. (1986). *Kimberlites: Mineralogy, Geochemistry, and Petrology.* Plenum Press, New York. 442 pp.

Mitchell, R.H. (1995). *Kimberlites, Orangeites and Related Rocks*, Plenum Press, New York.

Mitchell, R.H. (2008). Petrology of hypabyssal kimberlites: Relevance to primary magma compositions. *Journal of Volcanology and Geothermal Research,* 174, 1-8.

Mitchell, R. and Tappe. S. (2010). Discussion of "Kimberlites and aillikites as probes of the continental lithospheric mantle", by D Francis and M. Patterson (Lithos v. 109, p 72-80). *Lithos*, 115, 288-292.

Nowell, G.M., Pearson, D.G., Bell, D.R., Carlson, R.W., Smith, C.B., Kempton, P.D., Noble, S.R. (2004). Hf Isotope systematics of kimberlites and their megacrysts: new constraints on their source regions. *Journal of Petrology* 45, 1583–1612.

Patterson, M., Francis, D., McCandless, T. (2009). Kimberlites: magmas or mixtures? *Lithos* 112, 191-200.

Smith, C. B. (1983). Pb–Sr and Nd isotopic evidence for sources of southern African Cretaceous kimberlites. *Nature* 304, 51–54.

Tappe, S., Steenfelt, A. and Nielsen, T. (2012). Asthenospheric source of Neoproterozoic and Mesozoic kimberlites form the North Atlantic Craton, West Greenland: New high-precision U-Pb and Sr-Nd isotope data on perovskite. *Chemical Geology,* 320-321, 113-127.\

Tappe, S., Pearson, D.G., Kjarsgaard, B.A., Nowell, G. and Dowall, D. (2013). Mantle transition zone input to kimberlite magmatism near a subduction zone: Origin of anomalous Nd-Hf isotope systematic at Lac de Gras, Canada.

Zurevinski, S.E., Mitchell, R.H. (2011). Highly evolved hypabyssal kimberlite sills from Wemindji, Quebec, Canada: insights into the process of flow differentiation in kimberlite magmas. *Contributions to Mineralogy and Petrology* 161, 765-776.

1. Introduction

Continental intraplate magmatism results in the emplacement of primitive igneous rock suites with various radiogenic and stable isotope compositions, depending on mantle source regions and tectonic activity. The study of such rock suites allows insight into the interaction between mantle-derived melts and continental mantle lithosphere. Global kimberlites represent among the deepest probes into magmatic activity beneath thick continental plates, whilst contributing significantly to the global economy via the production of diamonds.

Kimberlite melt generation is commonly suggested to be linked to large-scale tectonic processes, including fracture zone propagation (Jelsma *et al*., 2004) and continental rifting (Tappe *et al*., 2012; Yaxley *et al*., 2013), which coincide with global supercontinent cycles (Jelsma *et al*., 2009; Tappe *et al*., 2014). It has also been suggested that kimberlites are derived from mantle plumes (Crough *et al*., 1980; Heaman *et al*., 2004; Collerson *et al*., 2010), and some authors envisage the core-mantle boundary as a kimberlite heat source region (Haggerty, 1994; Torsvik *et al*., 2010). Kimberlite melt generation in, and extraction from, the convecting upper mantle to mantle transition zone triggered by continental-scale subduction-induced mantle flow has also been suggested, in particular, to explain Mesozoic-Cenozoic kimberlite occurrences across western North America (McCandless *et al*., 1999; Tappe *et al*., 2013). Alternatively, kimberlites may be associated with melting mechanisms that occur at shallower levels, specifically the boundary between the continental lithospheric mantle (CLM) and asthenosphere, resulting in production of other primitive volatile-rich low-volume magma types such as carbonatites, melilitites, orangeites, and ultramafic lamprophyres (UMLs) (Alibert *et al*., 1983; Rogers *et al*., 1992; le Roex and Lanyon, 1998; Janney *et al*., 2002; Tappe *et al*., 2008, 2012; Giuliani *et al*., 2015).

Canada hosts an abundance of kimberlite occurrences, emplaced into various tectonic terranes, including Archean cratons (e.g., Slave, Rae, Superior), as well as Proterozoic mobile belts such as the Trans-Hudson and Torngat domains,

which consist partly of reworked Archean cratonic material (Hoffman, 1988; Scott-Smith, 2008). A prominent Late Neoproterozoic magmatic event (680-540 Ma; Fig. 1), resulting in the emplacement of multiple kimberlites, carbonatites, and UMLs across eastern and Arctic Canada and West Greenland, has been referred to as the "Laurentian Kimberlite Province" (Tappe *et al*., 2014). Although abundant isotope data have been collected for the Laurentian Kimberlite Province (e.g., West Greenland – Nelson, 1989; Gaffney *et al*., 2007; Tappe *et al*., 2011, 2012; Baffin Island - Tappe *et al*., 2014; Labrador - Tappe *et al*., 2006, 2007, 2008), comprehensive isotope datasets for Neoproterozoic kimberlites and related rocks from the eastern Superior craton in Canada are lacking, which hampers the understanding of this deeply sourced magmatism. For example, it remains controversial whether the Laurentian Kimberlite Province formed in response to mantle plume impingement beneath the Rodinia supercontinent (Puffer, 2002; Tachibana *et al*., 2006; Ernst and Bleeker, 2010), or whether the volatile-rich magmatism was related to deep melting events distal to prominent rift zones and the breakout margins along which Laurentia separated from Rodinia (Birkett *et al*., 2004; Heaman *et al.*, 2004; Tappe *et al.*, 2004, 2014).

In this study, the radiogenic Sr-Nd-Hf-Os and stable C-O isotope compositions of hypabyssal magmatic kimberlite samples have been analysed from the coeval Renard and Wemindji occurrences on the eastern Superior craton in Quebec, Canada. The 654 ± 6 Ma Renard (this study) and 629 ± 29 Ma Wemindji (Letendre *et al*., 2003) kimberlite clusters on the eastern Superior craton occur in the interior of the Canadian Shield, approximately 400 km apart (see Fig. 1 and Appendix C Fig. C1). These kimberlites are ideal probes into deep melting processes during global Late Neoproterozoic plate reorganisation (e.g., Rodinia supercontinent break-up) due to their fresh hypabyssal nature and critical position distal to recognized rift zones and breakout margins such as the St. Laurence rift and Labrador Sea, respectively.

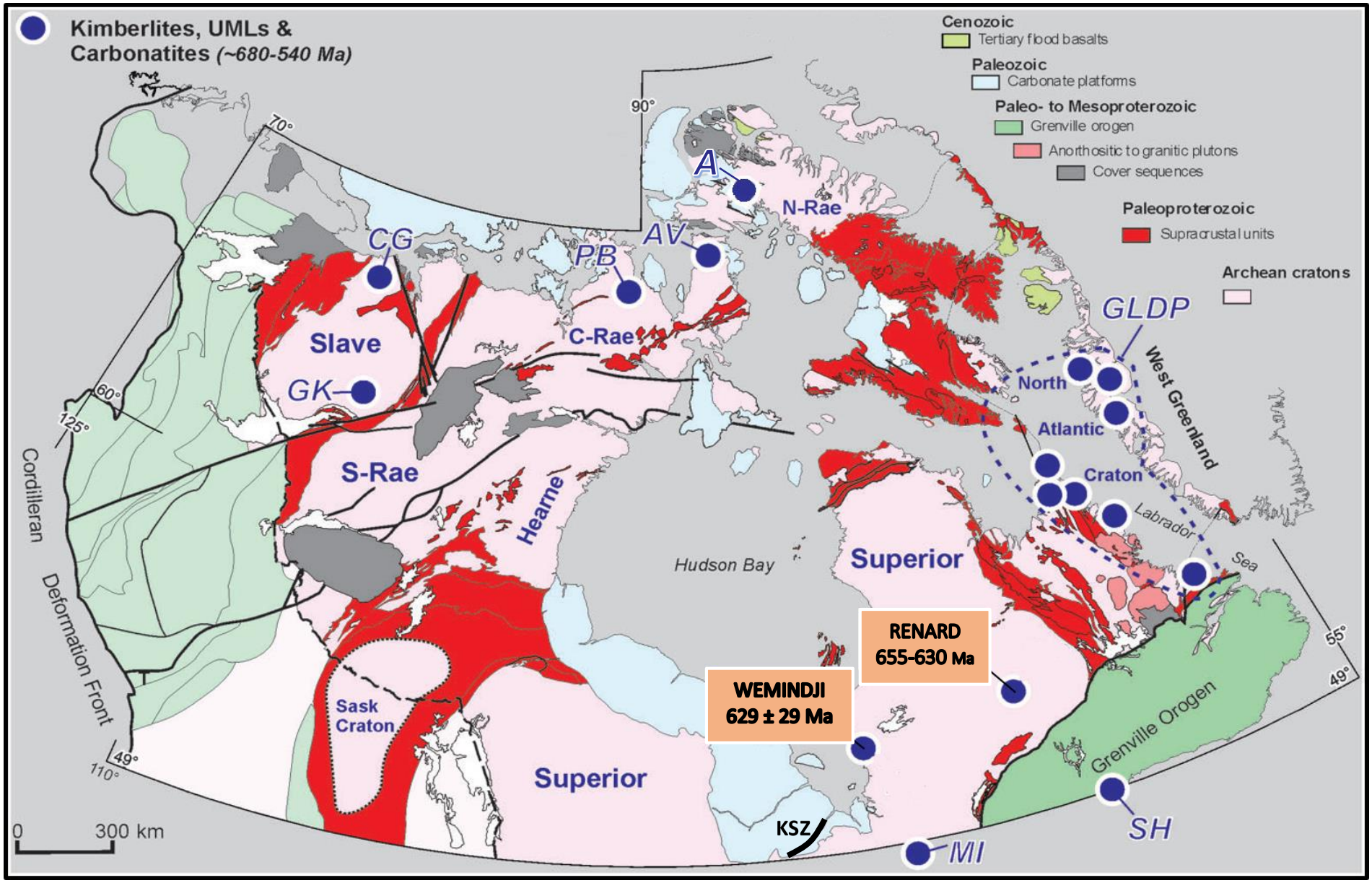

3 Figure. 1: Geological map of the Canadian-Greenland shield (modified from Tappe *et al.*, 2014; reconstruction after Corrigan *et al.*, 2009). The northern (N-Rae), central (C-Rae) and southern (S-Rae) divisions of the Rae craton follow Snyder *et al.* (2013). Blue circles represent a Neoproterozoic kimberlite, UML and carbonatite province, of which, the similarly aged Renard and Wemindji kimberlites are a part of. A – Amon Kimberlite Sill Complex, AV – Aviat kimberlites, CG – Coronation Gulf kimberlites, GK – Gahcho Kue kimberlites, GLDP – Greenland-Labrador diamond province (kimberlites, UMLs, carbonatites), MI – Manitou Island carbonatite, PB – Pelly Bay kimberlites, SH – St. Honore carbonatite. The Kapuskasing Structural Zone (KSZ) is also shown.

Despite significant petrographic variability of the Renard and Wemindji hypabyssal kimberlites, as also expressed by their major and trace element variability, the results show that their radiogenic isotope compositions are remarkably similar, suggesting a common moderately depleted convecting upper mantle source region, in alignment with global Group-1 kimberlite magmatism (Smith, 1983; Nowell *et al*., 2004; Carlson *et al*., 2006; Paton *et al*., 2009; Tappe *et al*., 2011, 2014; Griffin *et al*., 2014).

These new data for eastern Superior craton kimberlites of Neoproterozoic age, including scarce PGE and Os isotope analyses, suggest that no extreme mantle source components are required in the formation of these kimberlite magmas. Due to their similar major and trace element compositions to kimberlites worldwide, it would appear that in general, Group-1 kimberlite magma requires unusual melting conditions of common mantle components beneath thick continental lithosphere.

2. Background

2.1 Kimberlites of the Superior craton

The Superior craton is the largest exposed area of Archean crust on Earth (Hoffman, 1988; Percival *et al*., 2006). It comprises numerous continental fragments or terranes, separated by intrusive and supracrustal rock sequences (Percival *et al*., 2006). The accretion of these terranes took place during what is now collectively known as the Kenoran Orogeny, which culminated after a series of distinct orogenies at approximately 2.7 Ga (Hoffman, 1988). At ca. 1.8 Ga, these amalgamated terranes were involved in a Himalayan-style continent-continent collision with the Western Churchill province, known as the Trans-Hudson Orogeny (Hoffman, 1988).

The northern sector of the Superior craton has been a significant region for diamond exploration during the past 25 years (e.g., Moorhead *et al.*, 2003). Although most North American kimberlites are situated within stable Archean cratons, there is evident structural control on kimberlite magmatism as seen in the relationship between the distribution of kimberlite bodies and crustal scale fault

zones (Moorhead *et al.*, 2003; Snyder and Lockhart, 2005).

Superior craton kimberlite magmatism occurred between 1100 and 130 Ma (Heaman *et al*., 2004); however, the craton has a high residual potential for new discoveries of kimberlites and related rocks (Januszczak *et al*., 2013). Mesoproterozoic kimberlite and associated ultramafic lamprophyres, flood basalts, alkaline and carbonatite magmatism are linked to continued mantle upwelling beneath, and Mesoproterozoic mid-continental rifting of, the Lake Superior region, postdating the aforementioned Trans-Hudson Orogeny (Griffin *et al.*, 2004; Heaman *et al*., 2004). The failed Mesoproterozoic Midcontinent Rift System, occurring on the southern border of the Superior craton as a syncline-like feature, appears to be missing an "arm" of a possible triple junction in paleomagnetic anomaly studies (Perry *et al.*, 2004; Stein *et al.*, 2014), comparable to traditional continental rift systems (e.g. East African Rift System).

The oldest known kimberlites of the Superior craton are the 1100 Ma Bachelor Lake and Kyle Lake kimberlites, and the youngest are occurrences within the Kirkland Lake and Timiskaming kimberlite fields, ranging in age between 165 and 134 Ma (Heaman and Kjarsgaard, 2000; Heaman *et al*., 2004). Mesozoic kimberlites of the Superior craton have been linked to Great Meteor hotspot magmatism based on the progressive younging of kimberlite emplacement in eastern North America in southeasterly direction (Heaman and Kjarsgaard, 2000).

The Wemindji and Renard kimberlite occurrences on the eastern Superior craton in Quebec form part of a larger Late Neoproterozoic kimberlite province referred to as the "Labrador Sea Province" by Heaman *et al*. (2003). More recently, this magmatic province has been extended as the "Laurentian Kimberlite Province" to include kimberlites and related rocks (e.g., carbonatites and ultramafic lamprophyres) from Baffin Island and West Greenland (Tappe *et al*., 2014). The Laurentian Kimberlite Province (680-540 Ma; Tappe *et al*., 2014) has compositional and time analogues in northern Europe (e.g., Dahlgren, 1994; O'Brien and Tyni, 1999; Meert *et al*., 2007) (former Baltica within the Rodinia

supercontinent configuration), and this entire Late Neoproterozoic association of deeply derived volatile-rich magmatism is referred to as the North Atlantic Alkaline Province (Doig, 1970; Tappe *et al*., 2004; O'Brien *et al*., 2005).

2.1.1 Renard kimberlites

In 2001, diamond exploration in northern Quebec resulted in the discovery of the nine diamondiferous Renard kimberlite pipes, which form part of the Foxtrot kimberlite cluster (Moorhead *et al*., 2003; Birkett *et al*., 2004; Fitzgerald *et al*., 2009; Patterson *et al*., 2009). An unpublished radiometric age determination (i.e., no data were provided and discussed) suggested kimberlite magma emplacement in Renard Pipe-1 at ca. 630 Ma (Birkett *et al*., 2004). New U-Pb perovskite age determinations for hypabyssal kimberlite samples from Renard Pipe-2 and Pipe-3 suggest kimberlite magma emplacement at 653.8 ± 6 Ma (see Section 4.6).The kimberlite magmas erupted through Archean metamorphic basement rocks of the Opinaca Subprovince comprising migmatite, granite and gneiss, metamorphosed from a sedimentary succession of mostly meta-graywacke (Birkett *et al*., 2004; Percival *et al*., 2006; Fitzgerald *et al*., 2009).

Based on geophysical and drill hole information, the kimberlite pipes represent small irregular to elongate bodies with surface areas between 0.3 and 1.5 ha (Birkett *et al*., 2004; Fitzgerald *et al*., 2009; Muntener and Scott-Smith, 2013), suggesting pipe erosion down to lower diatreme or root zone levels. Two major dyke/sill systems (Lynx and Hibou) up to 3 m wide/thick are exposed approximately 1 to 3 km west of the nine Renard kimberlite pipes, together comprising the Foxtrot kimberlite cluster (Patterson *et al*., 2009; Appendix C Fig. C1). The Renard hypabyssal pipes, Lynx dyke and Hibou dyke will be collectively referred to as the Renard kimberlite suite in this study. An unpublished U-Pb ilmenite date (i.e., no data were provided and discussed) suggests an apparently younger age of 522 ± 30 Ma for the Lynx dyke (McCandless *et al*., 2008). The mineralogy and bulk rock major and trace element compositions of kimberlites from the Renard suite suggest an affinity to

archetypal Group-1 kimberlites (Table 1, 2 and 3; Birkett *et al*., 2004; Patterson *et al*., 2009).

At the time of kimberlite magma emplacement at Renard (653.8 ± 6 Ma), the eastern Superior craton lithospheric mantle had a minimum thickness of 200 km and a relatively cool xenolith-derived geotherm of 38 mWm^{-2} (Hunt *et al*., 2012). These combined characteristics suggest a 60 km thick diamond window beneath the Renard kimberlite suite during the Neoproterozoic, which is relatively narrow when compared with other kimberlite fields of the Laurentian Kimberlite Province (e.g., diamond window of 75 km beneath West Greenland; Sand *et al*., 2009).

A few Renard kimberlite pipes, namely 2, 3, 4 and 9, have proven to be economic diamond deposits, with a combined indicated reserve of 18 million carats, which is relatively small in comparison with Jwaneng Mine in Botswana (reserves of approximately 88 million carats after more than 30 years of mining; InfoMine, 2011). Conversely, the Wemindji kimberlites approximately 400 km west of Renard (see Section 2.1.2; and Fig. 1) have yielded minimal, inconsequential microdiamond contents (Moorhead *et al*., 2003; Zurevinski and Mitchell, 2011).

The Renard kimberlites sampled lithospheric mantle that was predominantly peridotitic (89%) and in particular lherzolite-rich (Hunt *et al.,* 2012). The significant garnet harzburgite subpopulation of the peridotitic portion (24%) suggests preservation of a cratonic mantle root that was highly depleted, relative to the 10% worldwide average of harzburgitic garnets from Archean cratonic mantle sections (Griffin *et al*., 2003b). Strong CLM depletion appears to be a common trait of the eastern Superior craton (Hunt *et al*., 2012). Spinel and phlogopite compositions from Renard Pipe 1, presented by Birkett *et al*. (2004), are indicative of these kimberlites being an intermediate between ultramafic lamprophyre and Group 1 kimberlite. Specific spinel compositional trends have

Table 1: Estimated modal mineral abundances (vol.%) of hypabyssal magmatic kimberlites from the Renard and Wemindji clusters, Superior craton, Quebec, Canada.

Sample ID	Kimberlite Cluster	Kimberlite Body	Sample Type	Longitude WGS84	Latitude WGS84	Olivine			Grdm. Phlogopite	Grdm. Spinel & Ilmenite	Grdm. Rutile	Grdm. Perovskite	Grdm. Carbonate		Garnet xenocrysts
						Fresh	Altered						Primary	Secondary	
							Carbonated	Serpentinized							
RD-R2 3	Renard	Pipe 2	Core	-72.1915	52.8139	9	-	15	5	30	-	1	30	10	-
RD-R2 19*	Renard	Pipe 2	Core	-72.1915	52.8139	5	5	20	25	8	-	2	25	10	-
RD-R3-07	Renard	Pipe 3	Core	-72.1886	52.8132	5	-	20	22	15	-	3	30	5	-
RD-11646	Renard	Pipe 3	Underground	-72.1982	52.8168	8	-	20	25	20	-	2	20	5	-
RD-11649	Renard	Pipe 3	Underground	-72.1982	52.8168	-	20	25	16	13	-	1	20	5	-
RD-11650	Renard	Pipe 3	Underground	-72.1982	52.8168	2	8	25	18	6	-	1	30	10	-
RD-L221-3	Renard	Lynx Dyke	Trench	-72.2267	52.8119	-	-	40	10	23	-	2	20	5	-
RD-L221-7	Renard	Lynx Dyke	Trench	-72.2267	52.8119	-	10	34	8	15	2	1	20	10	-
RD-L230-5	Renard	Lynx Dyke	Trench	-72.2239	52.8051	-	10	20	10	20	-	<1	30	10	-
RD-L230-6	Renard	Lynx Dyke	Trench	-72.2239	52.8051	-	10	45	5	10	-	<1	25	5	-
RD-H5	Renard	Hibou Sill	Trench	-72.2213	52.823	-	14	25	5	10	-	1	35	10	-
WEM-02-09 10/1A	Wemindji	Sheet	Core	-78.44576	53.03172	-	15	20	2	24	1	-	30	8	-
WEM-02-09 10/3	Wemindji	Sheet	Core	-78.44576	53.03172	-	10	40	-	15	-	-	30	5	<1
WEM-02-09 10/6	Wemindji	Sheet	Core	-78.44576	53.03172	-	15	20	2	23	-	-	30	10	-
WEM-02-09 10/10	Wemindji	Sheet	Core	-78.44576	53.03172	-	-	10	-	20	2	-	58	10	-
WEM-02-10	Wemindji	Sheet	Core	-78.44576	53.03172	-	10	25	10	5	-	-	45	5	-
WEM-02-22 24	Wemindji	Sheet	Core	-78.44576	53.03172	2	5	30	5	25	-	-	28	5	-
WEM-02-22 25	Wemindji	Sheet	Core	-78.44576	53.03172	-	12	25	2	16	-	-	35	10	<1
WEM-02-26 1	Wemindji	Sheet	Core	-78.44576	53.03172	2	5	40	1	21	1	-	20	10	<1
WEM-02-26 2	Wemindji	Sheet	Core	-78.44576	53.03172	2	15	35	1	15	2	-	20	10	<1
WEM-02-26 3	Wemindji	Sheet	Core	-78.44576	53.03172	-	-	-	-	-	-	-	-	-	-

Mineral abundances listed as <1 vol.% are accessory in nature.

*Sample RD-R2-19 was unsuitable for geochemical studies due to the high abundance of crustal material included in the sample and heterogeneity.
The presence of perovskite, however, alllows for geochronological analysis

since been proven inadequate in the classification of Group-1 kimberlites (Caro *et al*., 2004; Roeder & Schulze., 2008; Patterson *et al*., 2009).

The Renard kimberlite samples analysed in this study are derived from the hypabyssal root zones of pipes 2 and 3, as well as the Lynx and Hibou dykes. Due to the hypabyssal nature of these samples, they are referred to as "fresh", with the implication that they have been mantle-derived and relatively unaffected by devolatilisation and brecciation usually associated with pyroclastic kimberlite material of the diatreme facies. Low-temperature meteoric alteration is evident in the replacement of olivine by serpentine. The fresh kimberlite material contains sub- to anhedral relict olivine macrocrysts, ranging in size from 1 to 5 mm in diameter (Table 1; Fig. 2 A). The remainder of the olivine (macrocrysts and groundmass) in these samples has been replaced by serpentine and calcite. Phlogopite is a common microphenocryst phase (>200 μm), but is more prevalent as a groundmass constituent (Fig. 2 B). These kimberlite samples also contain euhedral groundmass perovskite grains at an average of 40 μm in size, allowing for successful geochronological analysis on samples RD-R2-19 and RD-11646 (Section 4.6). The groundmass comprises ilmenite, spinel, perovskite, phlogopite, serpentine, apatite, and calcite. For detailed petrographic descriptions see Appendix A.

2.1.2 Wemindji kimberlites

Thin, sub-horizontal kimberlite sills, emplaced into granitic gneisses of the La Grande subprovince of the eastern Superior craton, occur 45 km east of the village of Wemindji in Quebec (Letendre *et al*., 2003). The La Grande subprovince is composed of a succession of Neoarchean plutonic, volcanic, and metasedimentary rocks, overlying Mesoarchean basement rocks of the Superior Province (Percival *et al*., 2012, and references therein). A zone of crustal extension is represented by a system of fractures within the La Grande volcanic belt (Moorhead *et al*., 2003; Zurevinski and Mitchell, 2011), which may represent an extension of the Archean Kapuskasing tectonic zone to the northeast

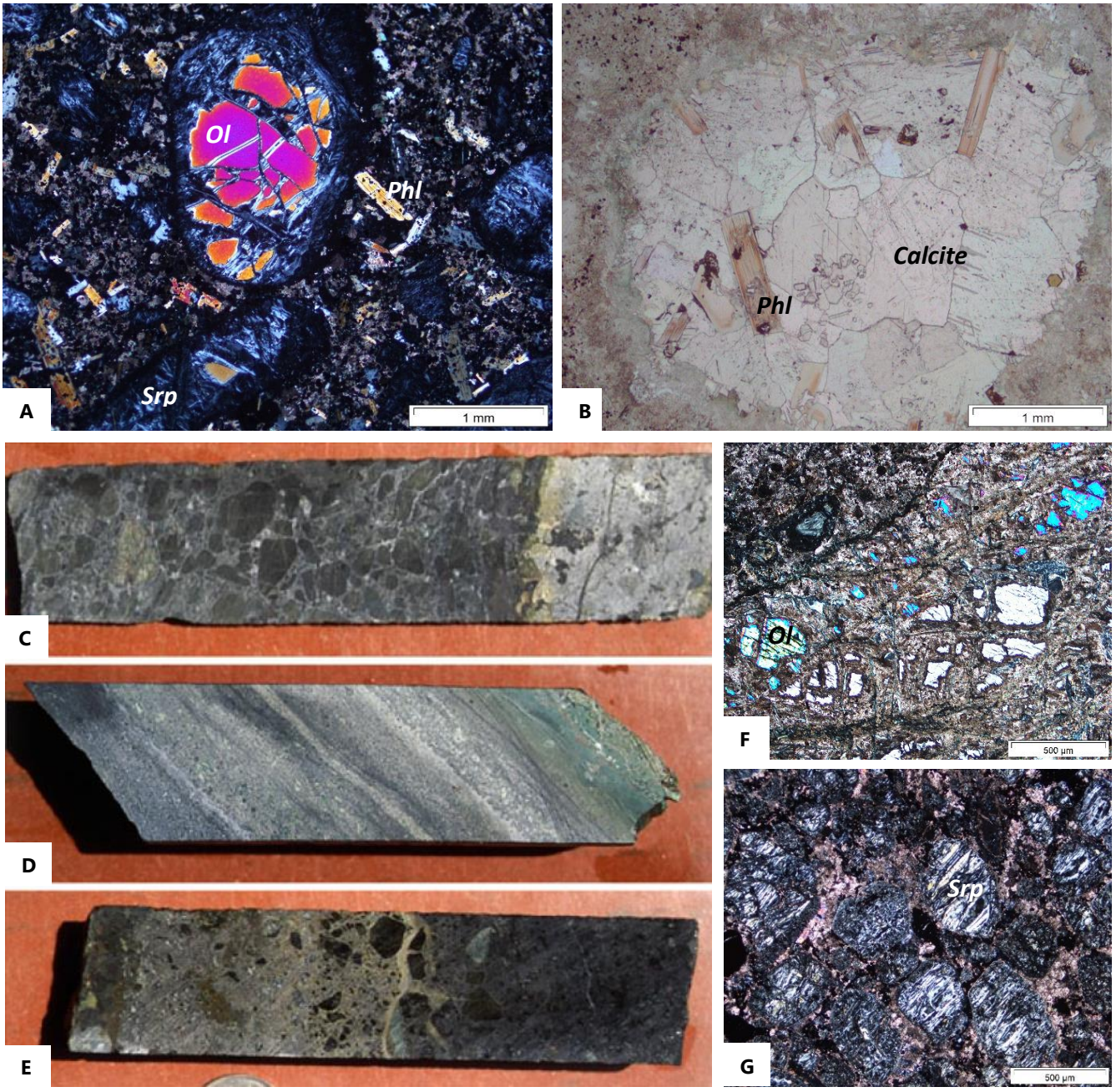

Figure 2: A-B) Photomicrographs of samples from the Renard kimberlites depicting the freshness of the samples. A: (XPL) Fresh olivine macrocryst in a groundmass of ilmenite, spinel, perovskite, phlogopite laths and calcite. B: Plane polarised light (PPL) image of primary calcite with large phlogopite and minor perovskite inclusions. C-E: Drill core images of Wemindji kimberlites taken from Zurevinski & Mitchell (2011), which are the exact same rock samples used for this study. C) Contact between a macrocryst-rich hypabyssal kimberlite and a harzburgite xenolith (core length: 25 cm). D: Sample showing flow differentiation prominent in Wemindji kimberlites (core length: 12 cm). E: Macrocryst–rich sample with zoning of different units (core length: 18 cm). F: Photomicrograph in XPL showing rare fresh olivine relicts. G: Serpentinised olivine macrocrysts shown in XPL of a Wemindji kimberlite sample in a groundmass dominated by calcite.

(Appendix C Fig. C2; Percival and Card, 1983; Zurevinski and Mitchell, 2011). The intracratonic Kapuskasing Structural Zone (KSZ) transects the central Superior Province and contains lower crustal rocks at surface reflecting a ~35 km palaeodepth (Percival and Card, 1983; Leclair *et al*., 1994; Percival *et al*., 1994). The KSZ also hosts numerous alkaline intrusions in Ontario, and it is interpreted as an east-verging thrust fault through 20 km of upper and middle crust of the Archean Superior craton (Percival and Card, 1983; Leclair *et al*., 1994).

The KSZ is bounded on the southeast by faults, and gradationally to the west near Lake Superior by low-grade metamorphic rocks of the Michipicoten belt (Percival and Card, 1983). The southeast faults are part of the Ivanho Lake cataclastic zone, as part of the Abitibi and Opatica subprovinces (Percival and Card, 1983). The KSZ is characterised by high-grade metamorphic rocks that cause positive aeromagnetic and gravity anomalies (Percival *et al*., 1994). The Kapuskasing uplift event is only poorly constrained, and it appears that uplift and thrusting occurred during the Neoarchaean (Percival and Card, 1983). Subsequent extension on the southern border of the Superior craton, resulting in the Mesoproterozoic Midcontinent Rift System, could have reactivated the KZS, shifting it into a more extensional tectonic environment, acting as the third "arm" of the possible triple junction of the continental rift (see Section 2.1).

An unpublished Rb-Sr phlogopite model age (i.e., no data were provided and discussed) of 629 ± 29 Ma for a Wemindji kimberlite sample (Letendre *et al*., 2003) is similar to the emplacement ages that were determined for the Renard 1, 2, and 3 kimberlite pipes (654-630 Ma; Birkett *et al*., 2004; this study). The Wemindji kimberlite sills are 2 m thick on average, occurring at 4-32 m depth below surface (Letendre *et al*., 2003). The sills are macrocrystal spinel-ilmenite-apatite-phlogopite-calcite kimberlite, and rock textures suggest that significant flow differentiation has occurred (Fig. 2 D; Zurevinski and Mitchell, 2011).

Wemindji kimberlite samples in this study can also be referred to as relatively "fresh", as described in Section 2.1.1. The Wemindji sample suite can be classified as typical kimberlite, based on its bulk rock geochemistry (as described

in Mitchell, 1986), as well as the spinel compositions and primary groundmass phlogopite-kinoshitalite (Mitchell, 1986, Zurevinski & Mitchell, 2011). However, the apparent lack of primary groundmass phlogopite (Table 1) is uncharacteristic of typical kimberlites, but this can be explained simply by separation of this phase before Wemindji sill emplacement during magma differentiation (Zurevinski & Mitchell, 2011). Flow differentiation textures and concentration of macrocrysts along flow differentiation planes can be attributed to a low viscosity magma (See Appendix B). The Kapuskasing Structural zone would have provided the ideal conditions and pathways for such differentiation to take place.

The abundant ilmenite and minor garnet contained in the Wemindji sample suite (Table 1; Appendix B) is indicative of sampling of material of lithospheric mantle origin (Letendre *et al*., 2003).. The presence G10 peridotitic and Group-1 eclogitic garnets (diamond-inclusion type), implies the sampling of diamondiferous mantle. Garnet Ni thermometry carried out in the same study by Letendre *et al.* (2003), showed that the majority of the garnet equilibrated at temperatures ranging from 1050 – 1300 °C. Approximately 50 % of the garnet samples are deduced to be of megacrystic origin, with the remaining garnets being derived from lherzolites in the cratonic lithospheric mantle (CLM), with minor to rare wehrlite and harzburgite origins, respectively (Letendre *et al*., 2003; Zurevinski & Mitchell, 2011). This information reaffirms a deep lithospheric mantle source for the Wemindji kimberlites. Unfortunately, diamond window information for beneath Wemindji at the time of kimberlite emplacement is not available in the present literature.

Wemindji kimberlite samples are generally finer-grained than the Renard kimberlite samples. Olivine is the dominant macrocryst phase of the Wemindji kimberlite sills, reaching up to 7 mm in diameter (Table 1, Fig. 2 D). It is typically serpentinised and concentrated along planes of magma flow differentiation. Minor fresh relict olivine macrocrysts have an average composition of Fo_{90} (Zurevinski and Mitchell, 2011) (Fig. 2, D-E). Wemindji kimberlite samples also contain 1-2 vol % ilmenite macrocrysts, which are >500 μm in size. Although the mineralogy

of the Wemindji sills is comparable to that of archetypal Group-1 kimberlites, monticellite and Cr-rich spinels are absent from the groundmass primary mineral assemblage. Additionally, the evolved spinel and phlogopite compositions they contain suggest late-stage crystallization from evolved carbonate-rich kimberlite magma (Zurevinski and Mitchell, 2011). Extensive flow differentiation texture and the highly evolved character preclude these carbonate-rich kimberlite sills from containing significant macrodiamond contents (Zurevinski and Mitchell, 2011; Fig. 2, C-F). For detailed petrographic descriptions see Appendix B.

3. Analytical Methods

3.1 Kimberlite sample preparation

Ten fresh hypabyssal kimberlite samples each from Renard and Wemindji were selected for this geochemical study (Table 1). The studied kimberlite material from Renard was provided as drill core (Pipe 2 and 3) and as hand specimens from underground shafts (Pipe 3). In addition, kimberlite trench samples from the Lynx dyke and Hibou sill were included, which occur approximately 1-3 km west of the Renard kimberlite pipes (Appendix C Fig. C1; Patterson *et al*., 2009). The kimberlite material from Wemindji was provided as drill core samples from several boreholes into the sill complex, as described in Zurevinski and Mitchell (2011).

The selected samples were cut into cm-thick rock slabs and material visibly free of crustal and mantle rock fragments was then washed with water and left to dry completely. The contamination-screened slabs were then wrapped in heavy-duty plastic bags and crushed with a hammer into mm-sized chips. Samples were split into 3 portions and milled using an agate mill for 10 minutes each, and then collated and milled again for a further 5 minutes. All new analyses reported herein (bulk rock major- and trace elements, Sr- Nd-Hf-Os-C-O isotopes) were conducted on the same homogenous rock powders produced for each kimberlite sample.

3.2 Major and trace element analysis

Fusion disks for major element analysis were prepared at the University of the Witwatersrand, South Africa. Cleaned Pt crucibles and porcelain LOI (loss on ignition) dishes were placed in a furnace at 1020^{o}C for 30 minutes to remove any organic residues. Sample powders (1 g per sample) were then placed into each cooled LOI dish (weights of the LOI dishes were recorded before and after sample addition), which were then ignited at 1020^{o}C for 40 minutes, and subsequently placed in a desiccator to cool to room temperature. The cooled LOI dishes were weighed to determine sample LOI.

Approximately 1.75 g Johnson Matthey Spectroflux 105 (lithium tetraborate, lithium carbonate, lanthanum oxide 47:37:16 w/w %) was placed into each Pt crucible (weights of the Pt crucible were recorded before and after this addition), which were then ignited at 1020^{o}C for 40 minutes, and subsequently placed in a desiccator to cool. The cooled Pt crucibles were then weighed to determine the actual flux weights (LOI – loss on ignition). Approximately 0.34 g of pre-ignited sample material was added into each corresponding Pt crucible, with the weight having been recorded after the addition. The sample was then ignited at 1020^{o}C for 50 minutes, and subsequently placed in a desiccator to cool. Any fused samples still containing solid particles after cooling were added back to the furnace and reignited for 60 minutes. The Pt crucibles were then weighed and returned to the furnace at 1020^{o}C. Fusion beads were individually poured and pressed on a hotplate. Any beads that contained bubbles or solid particles were broken and re-poured. Beads were allowed to set on the hotplate for 90 minutes. The hotplate was then turned off to allow the beads to anneal overnight. Sample glass beads were analyzed for major and selected trace elements on a Pananalytical Axios XRF spectrometer instrument at the University of the Witwatersrand.

Sample dissolution for ICP-MS analysis using microwave digestion was completed at the University of the Witwatersrand. Sample powder (50 mg of each

sample) was weighed into a weighing boat and transferred to a microwave Teflon vessel. Approximately 6 ml 3:2 concentrated HF:HNO_3 was added to each vessel and powders were dissolved in an ultraprep microwave digester for 60 minutes. Each sample was then transferred to a 15 ml Savillex beaker. The Savillex beakers were then placed on a hotplate at 60^{o}C for 24 hours and subsequently dried down at 70^{o}C. Approximately 2 ml 65% HNO_3 was then added to each beaker, beakers were capped and were left at 60^{o}C for 24 hours and then dried down again at 70^{o}C. A further 2 ml 65% HNO_3 was added to the samples and dried down at 75^{o}C. Once dry, 100 µl 65% HNO_3 was added to the samples, beakers were capped and stored until ICP-MS analysis with a Perkin Elmer ELAN Drc instrument.

3.3 Sample digestion for Hf-Sr-Nd ion exchange chromatography

Sample powder digestion for Sr-Nd-Hf isotope analysis was completed at Westfälische Wilhelms-Universität Münster (WWU), Germany. Approximately 125 mg powder of each sample was loaded into pre-cleaned 15 ml Savillex beakers, with approximately 5 drops of Milli-Q H_2O added to form a slurry. Concentrated HF and HNO_3 were then added to each sample in an approximate 3:1 ratio, and the beakers were subsequently placed in an ultrasonic bath.
The sealed and sonicated beakers were then placed on a hotplate for at least 2 days at 130°C. The beaker lids were then opened, and the sample solutions were dried down at 100°C. Approximately 10 ml 6N HCl was then added to the dry sample residues, and the converted and sonicated sample solutions were then placed again on a hotplate at 120°C overnight. Approximately 360 µl concentrated H_3BO_3 was added to each sample solution in order to inhibit fluoride formation. Sample solutions were placed back on a hotplate to ensure complete dissolution and subsequently dried down for the last time. Finally, 1.5 ml 3N HCl was added to the dried samples, and the sonicated solutions were transferred into 1.5 ml pre-cleaned centrifuge tubes and centrifuged for 10 minutes. Approximately 1 ml of each clear sample solution was further processed during sequential Hf-Sr-Nd ion

exchange chromatography (see Section 3.4). The remaining 0.5 ml of each sample solution were set aside for repeat analyses.

3.4 Hf-Sr-Nd ion exchange chromatography

Ion exchange chromatography for the separation and concentration of Hf, Sr, and Nd for isotope ratio determinations was performed at Westfälische Wilhelms-Universität Münster (WWU), Germany. Samples used for Sr-Nd-Hf measurement were not spiked. The Hf column chemistry was carried out using anion columns, with LN Spec resin (100-150 mesh), following the procedure outlined in Münker *et al*. (2001). Prior to loading of sample solutions, columns were cleaned and preconditioned using alternating 2N HF and 3N HCl. The 1 ml sample solutions were treated with ascorbic acid to reduce the contained ferric iron prior to column chemistry. Subsequent to sample solution loading onto the columns, the rare earth element (REE) cut was collected using a wash of 3N HCl. A series of 6N HCl, H_2O, citric acid, HNO_3, and hydrogen peroxide washes were applied to remove Ti. The Hf cut was then collected in 8 ml of mixed 3N HCl - 0.2N HF. The dried down REE cut was then re-dissolved in 6N HCl and minimal HNO_3 in order to eradicate organic material inherited from the Hf chemistry. These cuts were once again dried down and re-dissolved in 0.5 ml 2.5 N HCl. The Sr ion exchange chromatography was carried out using cation resin columns (AG50W-X8, 200-400 mesh). Columns were pre-cleaned using 6N HCl, and then conditioned in 2.5 N HCl. A purified Sr cut was collected from the loaded REE cut in 8 ml 2.5 N HCl following a 16 ml wash with 2.5 N HCl. Following collection of the Sr cut, and a 4 ml wash with 6N HCl, the final REE cut was collected in 6 ml 6N HCl. The REE cut was dried down and re-dissolved in 1 ml 0.18N HCl prior to the Nd ion exchange chromatography. The Nd ion exchange chromatography was carried out using LN Spec resin (50-100 mesh). The resin was pre-cleaned using 6N HCl. Neodymium was collected in 8 ml 0.25N HCl, following a 19 ml wash with 0.18N HCl.

Strontium isotope ratio determinations were performed on a Thermo Scientific

Triton thermal ionization mass spectrometer (TIMS). Hf and Nd isotope ratio determinations were conducted using a Thermo Scientific Neptune Plus multi-collector inductively coupled plasma mass spectrometer (MC-ICPMS). All isotope ratios were measured with a 2σ uncertainty. For standards used see footnotes on Table 5.

3.5 Os and HSE extraction procedure

Three hypabyssal kimberlite samples each from Renard and Wemindji were analysed for their Os isotope compositions and highly siderophile elements (HSE) concentrations at the Universität Bonn, Germany. Approximately 50 mg of a ^{190}Os-^{185}Re-^{99}Ru-^{106}Pd-^{191}Ir-^{194}Pt spike was added to 500 mg of each sample powder. Basalt standard BIR 1-a was included in this batch of kimberlite samples, as well as a total procedural blank. Approximately 1 g of sample powder was digested for 12 hours in 2.5 ml 10 M HCl and 5 ml 14 M HNO_3 in quartz glass tubes under 2 atm. pressure in an AntonPaar High Pressure Asher. Osmium was extracted following the procedure by Cohen and Waters (1996), where OsO_4 was separated into an organic phase and subsequently back-extracted into concentrated HBr. The enriched sample solution was then dried down on a hotplate. The microdistillation process of Birck *et al.* (1997) was then applied in an inverted PFA conical vial in order to purify the Os for mass spectrometry. Ion exchange chromatography was then necessary over anion columns (AG 1-X8, 100-200 mesh) for the extraction of HSEs from the digested samples (i.e. the remainder of the digested samples after organic phase extraction). The HSE chemistry is outlined in detail in Chu *et al.* (2014), and involves a series of HCl and HNO_3 rinses through 10 ml anion exchange resin columns. Osmium concentrations and isotope compositions were measured by ID-N-TIMS on a ThermoFisher Triton instrument. Concentrations of all HSEs were determined using a ThermoFisher Element XR ICP-MS instrument. A glass cyclonic spray chamber with a Micromist glass nebulizer (100 µl/min) was used for the measurement of Re, Ir and Pt. For the ICP-MS analysis of Ru and Pd, an ESI Apex desolvation system with a Teflon microflow nebulizer (200 µl/min) was used. Acid background

correction was accomplished by measuring wash solutions before each sample. Samples were corrected for respective procedural blanks analysed. All analyses were measured with a 2σ uncertainty.

3.6 C and O isotope analysis

Carbon and oxygen isotope analyses on bulk kimberlite carbonates were carried out at Westfälische Wilhelms-Universität Münster (WWU), Germany. Enriched phosphoric acid was reacted with the hypabyssal kimberlite sample powders for 7 days at 25°C in a temperature controlled water bath as described by Wachter and Hayes (1985). Liberated CO_2 from this process was then cryogenically purified and collected into 6 ml break-seal pyrex tubes. Isotope ratios were measured using a ThermoFinnigan Delta Plus gas source mass spectrometer fitted with a duel inlet. Replicate measurements of standards demonstrate a reproducibility of 0.15 ‰ for $\delta^{13}C$ and 0.20 ‰ for $\delta^{18}O$ analyses. Oxygen isotope ratios were corrected for temperature and mineral fractionation during sample preparation using a factor of $\alpha = 1.00925$ for calcite at 50°C (Friedman and O'Neil, 1977).

3.7 In-situ U-Pb perovskite isotope analysis by secondary ion mass spectrometry (SIMS)

The U/Pb perovskite isotope analyses were performed on the Cameca IMS-1280 ion-microprobe mass spectrometer at the Institute of Geology and Geophysics at the Chinese Academy of Sciences in Beijing. Isotope data for groundmass perovskites from hypabyssal kimberlites of Renard Pipe-2 (RD-R2-19) and Pipe-3 (RD-11646) was collected. Photomicrographs of the two Renard kimberlite samples that were used for U-Pb geochronology are provided in Figure 3, showing perovskite crystals in petrographic context. The complete dataset, including the various analysed perovskite mineral standards, is provided in Appendix D. Li *et al*. (2010) provide a detailed account on Beijing SIMS instrument performance and the U/Pb isotope analytical protocol for perovskite is described. Below, only a method summary is given.

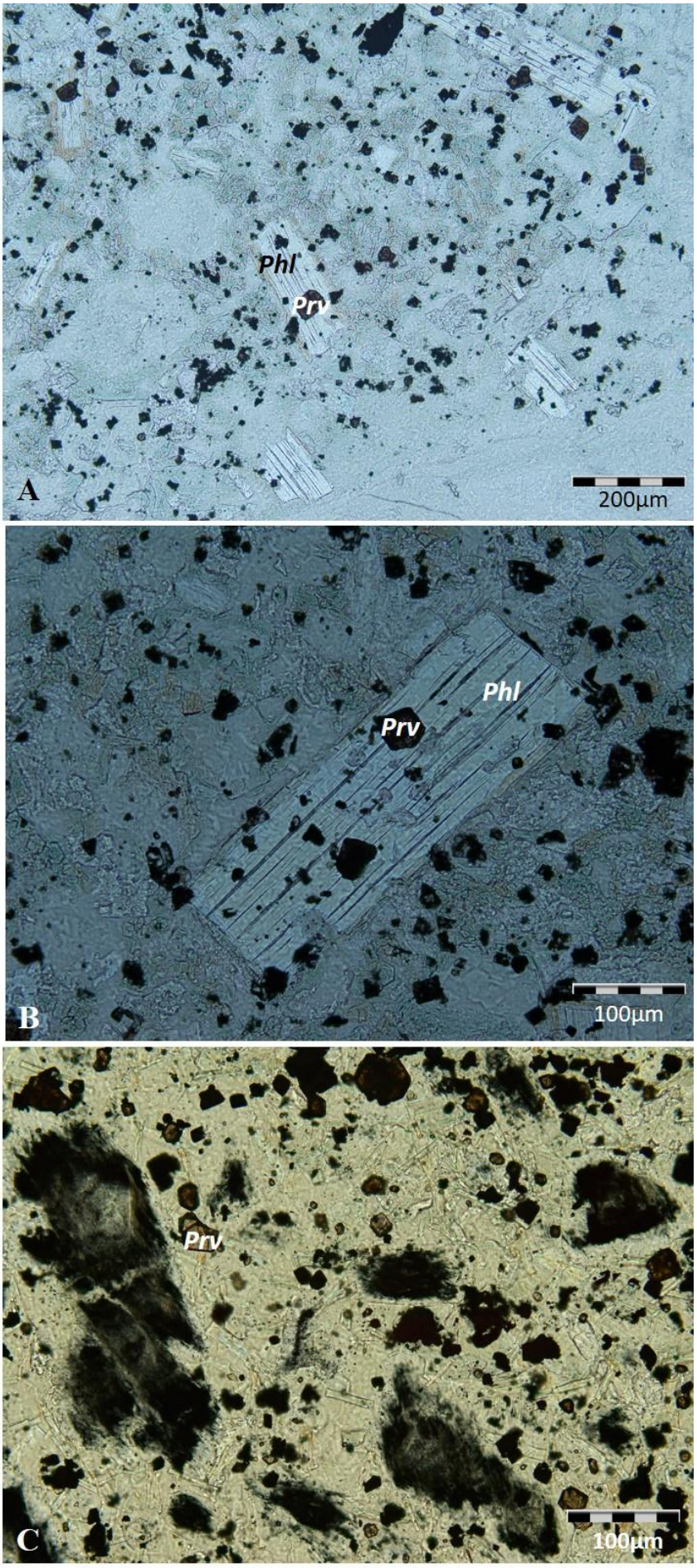

Figure 3: Photomicrographs of Renard samples RD-R2 19 (A-B) and RD-11646 (C) used for U-Pb geochronological measurements. A-B: Renard Pipe 2 sample RD-R2 19 depicting microphenocrystic phlogopite laths hosting sub- to euhedral perovskite grains (30-50 µm) in a poikilitic texture. C: Renard Pipe 3 sample showing brown subhedral perovskite grains (30-50 µm) in a calcite-serpentine-phlogopite groundmass.

The O^{2-} primary ion beam was accelerated at 13 kV, with 10 to 18 nA intensity. Analysis spot size was approximately 20×30 μm, i.e., an oval spot shape. Positive secondary ions were extracted in a 10 kV potential. The analyzed perovskite grains had been liberated from the kimberlite samples by a mineral separation procedure that is described in Tappe *et al*. (2012). For each sample, 16 fresh euhedral and visibly inclusion-free perovskite grains (30-50 μm across) were mounted in epoxy resin and polished to expose the grain centers as a flat surface. The epoxy mounts were coated with 30 nm of high-purity gold to ensure sample resistance below 20Ω. $^{40}Ca^{48}Ti_2{}^{16}O_4$ was used as the matrix reference peak to center secondary ion beams and to adjust elemental masses. Transmission at high mass resolution was increased by activation of rectangular lenses in the secondary ion optics. A mass resolution of approximately 8,000 at 50% peak height was used to separate U, Th, and Pb isotopes from isobaric interferences such as REE oxides (Ireland *et al*., 1990; Williams, 1998).

Secondary ion beam intensities were measured with a single electron multiplier in ion-counting mode by a peak jumping sequence. Each spot analysis on a single perovskite crystal consisted of 10 cycles, and data were collected for approximately 16 minutes. Previous studies demonstrated that the mass fractionation of Pb isotopes and Pb hydrides is negligible, and that these two effects cancel each other out to a large degree (Ireland *et al*., 1990; Whitehouse *et al*., 1997; Williams, 1998). Therefore, high- resolution of these effects, which would require a mass resolution of >30,000, is not applied on the Beijing Cameca IMS-1280 ion-microprobe (Li *et al*., 2010). The U-Th-Pb isotope ratios and elemental abundances of the 'unknowns' were calibrated against the Tazheran-3 perovskite standard *(March 2012 Session)* with a TIMS-determined $^{206}Pb/^{238}U$ age of 463 ± 2 Ma (Kinny *et al*., 1997), and against the Afrikanda-5 perovskite standard *(November 2014 Session)* with a TIMS- determined $^{206}Pb/^{238}U$ age of 381.6 ± 1.4 Ma (Wu *et al*., 2013).

These primary matrix-matched calibration standards were measured at the beginning and at the end of the analytical sessions, as well as after every three

unknown perovskite crystals. The analytical uncertainties of the $^{206}Pb/^{238}U$ measurements for the calibration standards, as well as other known sources of error, were propagated into our results for unknown perovskite crystals (Li *et al*., 2010). The U-Pb ages reported in Table 6 (Section 4.6) and Appendix D were calculated in Isoplot 2.2 (Ludwig, 2000) using the decay constants recommended in Steiger and Jäger (1977): $9.8485*10^{-10}$ a^{-1} for ^{235}U and $1.55125*10^{-10}$ a^{-1} for ^{238}U. The presence of initial common Pb was corrected utilizing the measured amount of ^{204}Pb and the terrestrial Pb evolution model of Stacey and Kramers (1975). In general, we report final U-Pb perovskite age results as $^{206}Pb/^{238}U$ dates, because this decay scheme is less sensitive to the initial common lead correction, which can be significant for perovskite analyses (Kramers and Smith, 1983; Heaman, 1989; Tappe and Simonetti, 2012).

The following age results were obtained for perovskite mineral standards that were analyzed as unknowns in March 2012 and November 2014 (all uncertainties are reported at the 2-sigma level): $^{206}Pb/^{238}U$ age of 378.4 ± 5.5 Ma for Afrikanda-5 (recommended age: 381.6 ± 1.4 Ma; Wu *et al*., 2013); $^{206}Pb/^{238}U$ age of 464.8 ± 4.8 Ma for Tazheran-3 (recommended age: 463 ±2 Ma; Kinny *et al*., 1997); $^{206}Pb/^{238}U$ age of 357.2 ± 10.6 Ma for Ice River (recommended ages: 356.5 ± 1.0 Ma and 361.7 ± 1.0 Ma; Heaman, 2009; Tappe and Simonetti, 2012).

4. Results

4.1 Bulk rock major and trace element compositions

Bulk rock major element data are presented in Table 2 and Figure 4. Hypabyssal kimberlite major element data are suitable to use as a simple analytical tool to quantify degrees of crustal contamination using, for example, the contamination index (C.I.) of Clement (1982), which is defined as:

$$C.I. = (SiO_2+Al_2O_3+Na_2O)/(MgO+2*K_2O)$$

Renard kimberlites have C.I. values ranging from 0.93 to 1.08, whereas Wemindji kimberlite C.I. values range from 0.63 to 1.58, with an outlier of 2.55).

Table 2: Major element concentrations (wt.%) of hypabyssal magmatic kimberlites from the Renard and Wemindji clusters, Superior craton, Quebec, Canada.

Sample ID	Kimberlite Cluster	Kimberlite Body	SiO_2	TiO_2	Al_2O_3	Fe_2O_3	FeO	MnO	MgO	CaO	Na_2O	K_2O	P_2O_5	Cr_2O_3	NiO	LOI	Total	CO_2	Contamination Index (Clement, 1982)
RD-R2 3	Renard	Pipe 2	30.5	1.09	1.79	0.89	7.2	0.12	34.0	7.3	0.07	0.42	0.35	0.26	0.18	15.6	99.9	5.06	0.93
RD-R3-07	Renard	Pipe 3	30.5	0.86	2.34	0.75	6.1	0.12	32.6	7.3	0.07	0.88	0.26	0.25	0.17	17.3	99.6	5.42	0.96
RD-11646	Renard	Pipe 3	33.6	1.14	2.40	0.87	7.1	0.11	34.7	4.6	0.07	1.03	0.35	0.28	0.19	13.4	99.7	2.64	0.98
RD-11649	Renard	Pipe 3	31.9	0.82	2.04	0.77	6.3	0.12	31.3	8.6	0.06	0.61	0.16	0.24	0.18	17.0	100.1	6.12	1.04
RD-11650	Renard	Pipe 3	29.9	0.85	1.84	0.80	6.5	0.15	30.1	10.6	0.03	0.51	0.16	0.25	0.18	18.4	100.2	7.73	1.02
RD-L221-3	Renard	Lynx Dyke	19.5	5.76	6.11	1.27	10.3	0.35	25.2	11.5	b.d	0.31	0.77	0.86	0.12	17.5	99.5	7.84	0.99
RD-L221-7	Renard	Lynx Dyke	26.1	1.97	2.09	0.91	7.3	0.26	26.2	14.2	0.01	0.36	0.38	0.34	0.17	19.9	100.2	10.44	1.05
RD-L230-5	Renard	Lynx Dyke	25.4	2.65	2.61	0.98	8.0	0.22	24.8	14.3	0.01	0.48	0.41	0.42	0.15	19.4	99.8	10.85	1.08
RD-L230-6	Renard	Lynx Dyke	29.2	2.53	2.22	0.74	6.0	0.20	29.2	10.3	0.04	0.45	0.16	0.38	0.18	17.8	99.4	7.95	1.04
RD-H5	Renard	Hibou Sill	28.9	2.05	1.55	0.93	7.6	0.23	29.0	10.5	0.02	0.38	0.38	0.29	0.19	18.2	100.2	7.77	1.03
WEM-02-09 10/1A	Wemindji	Sheet	20.9	3.39	1.64	0.75	6.1	0.20	21.9	16.4	0.15	0.12	0.46	0.19	0.09	26.5	98.9	20.56	1.02
WEM-02-09 10/3	Wemindji	Sheet	17.1	3.61	0.98	0.53	4.3	0.20	18.2	23.2	0.13	0.11	0.64	0.21	0.12	28.9	98.2	25.36	0.99
WEM-02-09 10/6	Wemindji	Sheet	22.9	2.54	1.24	0.79	6.4	0.16	25.9	13.7	0.14	0.14	0.44	0.18	0.12	24.8	99.4	18.36	0.93
WEM-02-09 10/10	Wemindji	Sheet	15.2	1.45	1.09	0.44	3.6	0.18	24.5	19.5	0.15	0.10	0.56	0.07	0.02	31.6	98.4	26.16	0.67
WEM-02-10	Wemindji	Sheet	23.5	1.64	0.96	0.35	2.9	0.09	9.4	31.8	0.12	0.12	0.56	0.11	0.08	27.9	99.4	24.99	2.55
WEM-02-22 24	Wemindji	Sheet	16.6	2.81	1.36	1.04	8.4	0.17	28.8	13.7	0.10	0.04	0.32	0.14	0.07	25.8	99.3	20.96	0.63
WEM-02-22 25	Wemindji	Sheet	24.4	6.61	0.89	1.28	10.3	0.16	29.6	7.4	0.05	0.08	0.27	0.18	0.18	18.1	99.6	7.91	0.85
WEM-02-26 1	Wemindji	Sheet	26.6	2.81	1.03	1.12	9.1	0.14	31.2	7.4	0.07	0.05	0.26	0.18	0.15	20.4	100.4	8.68	0.88
WEM-02-26 2	Wemindji	Sheet	37.2	3.63	0.73	0.61	5.0	0.13	23.9	10.9	0.27	0.13	0.46	0.12	0.12	16.5	99.6	9.82	1.58
WEM-02-26 3	Wemindji	Sheet	23.7	9.15	0.83	1.71	13.8	0.14	28.1	5.7	0.03	0.05	0.21	0.23	0.13	16.2	100.0	6.12	0.87

Major element concentrations are XRF data determined at the University of the Witwatersrand, Johannesburg.

Fe_2O_3 is calculated as 10 % of the total Fe

b.d. = below detection.

LOI is defined as the difference in weight of the sample after ignition at 1020°C for 40 minutes

CO_2 content was determined separately upon sample digestion at WWU, Münster

Contamination Index = $(SiO_2+Al_2O_3+Na_2O)/(MgO+2*K_2O)$, (Clement, 1982).

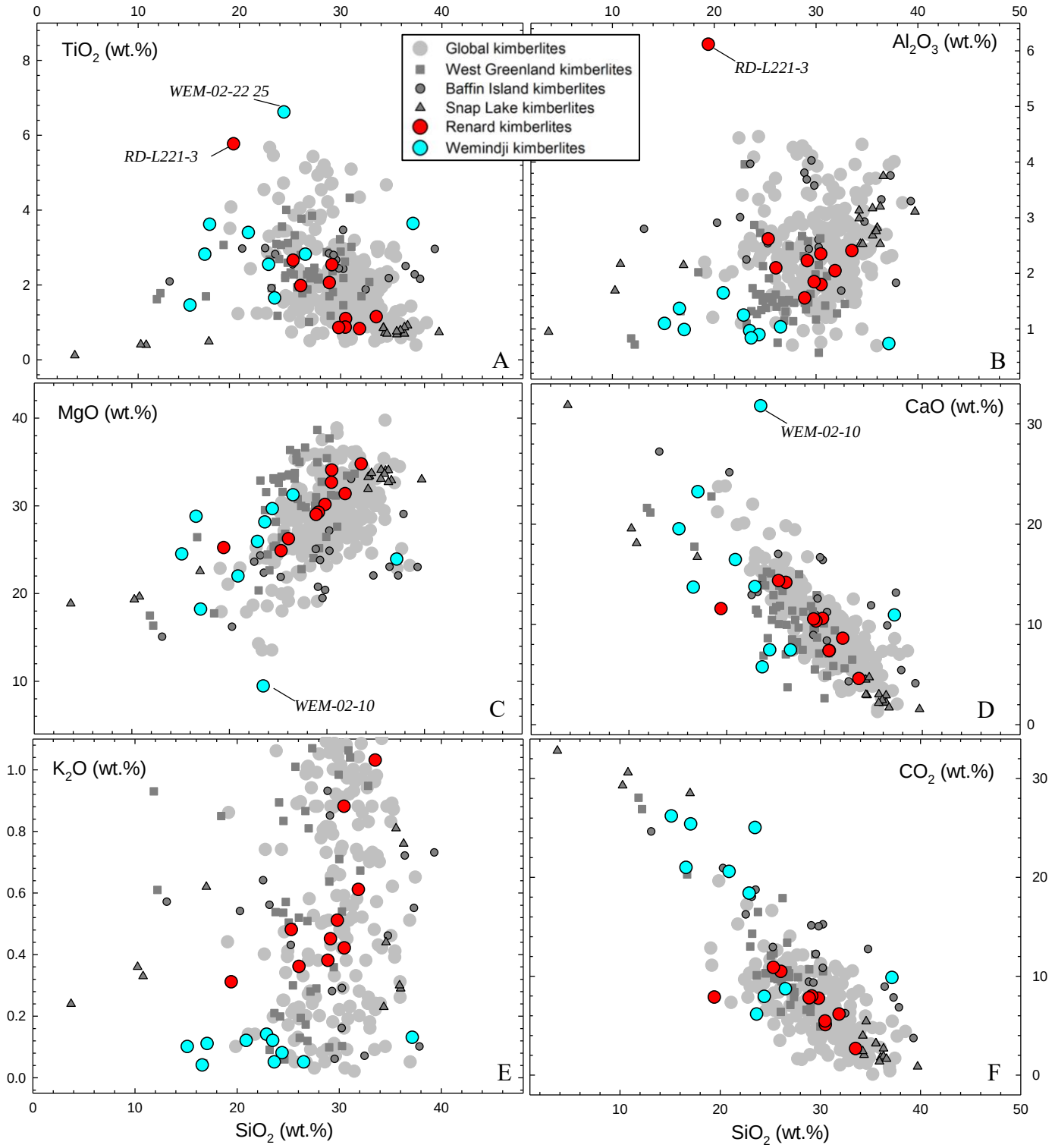

Figure 4: Whole rock major element compositions of the Renard and Wemindji magmatic kimberlites, compared to global magmatic kimberlites (Kjarsgaard *et al*., 2009), including West Greenland kimberlite dykes (Tappe *et al*., 2011; Gaffney *et al*., 2007) and other Canadian kimberlite dyke occurrences (Tappe *et al*., 2014; Agashev *et al*., 2008).

Conventionally, samples with C.I. values <1 are considered to be uncontaminated (Clement 1982; Mitchell, 1986). However, it is important to examine other geochemical parameters for magmatic kimberlite suites, such as radiogenic and stable isotopes, to fully assess the possible influence of crustal materials (le Roex *et al*., 2003; Kjarsgaard *et al*., 2009).

Silica contents of Wemindji and Renard kimberlites show a wide range of values, with Wemindji samples having a lower SiO_2 composition on average (~23 wt. % compared to ~29 wt. % in the Renard kimberlites). The SiO_2 content in the Renard kimberlite samples range between 19-33 wt. %, whereas Wemindji samples range between 15-37 wt. % (Fig. 4). The majority of the Renard samples depict a clustered TiO_2 range of 0.82-5.7 wt. % TiO_2 (Fig. 4 A), whereas the TiO_2 content is widely spread through the Wemindji samples, ranging from 1.45-9 wt. % TiO_2. The extremely high TiO_2 values can be attributed to ilmenite macrocrysts present in both kimberlite suites, but particularly abundant in the Wemindji kimberlites. Aluminium contents of the two sample suites show a more restricted range compared with other major elements (Fig. 4 B). The Renard kimberlite samples contain between 1.5 and 6 wt. % Al_2O_3. The 6 wt. % Al_2O_3 value for sample RD-L221-3 is an outlier from the Lynx dyke (Fig. 4 B), with the second highest value being 2.6 wt. % Al_2O_3. The Wemindji kimberlites have significantly lower Al_2O_3 contents, with values ranging between 0.73 and 1.6 wt. % Al_2O_3, with little to no overlap in Al_2O_3 contents between the Renard and Wemindji kimberlite suites.

The magnesium content of the two kimberlite suites largely overlaps and is relatively constrained, disregarding minimal outliers (Fig. 4 C). The Renard samples show MgO values between 24.8-34.7 wt. %. The Wemindji kimberlite sills show a wider range between 9.41 and 31.2 wt. % MgO.

The CaO content in each kimberlite suite correlates negatively with MgO (Appendix C Fig. C3). Renard kimberlites have a much lower range of CaO than the Wemindji kimberlites, from 4.6 to 14.3 wt. % CaO. Wemindji kimberlites once again have a wide range of values, between 5.7 and 31.7 wt. % CaO.

Sample WEM-02-10 has an elevated C.I. value (2.55), as well as the lowest MgO and highest CaO contents in the entire dataset. It can therefore be assumed that this sample is a crustally contaminated outlier (Fig. 4 D). The highest concentration for CaO in the remaining Wemindji kimberlite suite is therefore 23.2 wt. % CaO.

Potassium content is typically low, with Renard kimberlites containing slightly higher abundances than the Wemindji kimberlites, with ranges of 0.31-1.03 wt. % and 0.05-0.14 wt. % K_2O, respectively. There is no overlap in K_2O content between Renard and Wemindji kimberlites (Fig. 4 E).

The CO_2 contents are the most notable difference between the two kimberlite suites (Fig. 4 F). The Wemindji kimberlite sills contain significantly more CO_2 (up to 26.1 wt. %) than the Renard magmatic kimberlites (up to 10.8 wt. %). The elevated CO_2 content of the Wemindji kimberlite sills is evident at a macroscopic scale, with prominent carbonate-rich layers due to flow differentiation (see Section 2.1.2).

For completeness, the following summary is provided of the minor differences in bulk rock analyses between the Renard hypabyssal pipe material and the Lynx and Hibou dyke material. The hypabyssal pipe material contains higher abundances of SiO_2 (30-35 wt. % SiO_2) and MgO (30-34 wt. % MgO), lower abundances of TiO_2 (0.85- 1.14 wt. % TiO_2), CaO (4.6-8.6 wt. % CaO) and CO_2 (2.64-7.73 wt. % CO_2), than the Lynx and Hibou dykes. The hypabyssal pipe material also contains slightly higher abundances of K_2O (0.50-1.03 wt. % K_2O). Compositionally, the Hibou dyke is more comparable to the Renard hypabyssal pipe material than the Lynx dyke material.

Trace element data for the Renard and Wemindji magmatic kimberlites are listed in Table 3. In general, the incompatible element distributions of the Renard and Wemindji magmatic kimberlites are similar (Fig. 5).

The Renard kimberlites have higher concentrations of Rb and K compared to the Wemindji kimberlite sills, which correlates with the modal abundance of phlogopite (see Section 2.1.1; Fig. 2; Table 1). The Pb abundances are erratic in both Renard and Wemindji kimberlite suites, ranging between 2.9-46.7 and 3.7-79.8 ppm, respectively.

Table 3: Trace element concentrations (ppm) of hypabyssal magmatic kimberlites from the Renard and Wemindji clusters, Superior craton, Quebec, Canada.

Sample ID	Kimberlite Cluster	Kimberlite Body	Cs	Rb	Ba	Sr	Th	U	Nb	Ta	Pb	Zr*	Hf	Y*	La	Ce	Pr	Nd	Sm	Eu
RD-R2 3	Renard	Pipe 2	0.77	45.5	901	668	21.7	2.5	219	12.1	6.4	67.6	1.43	5.80	169	248	29.5	89.3	11.7	2.8
RD-R3-07	Renard	Pipe 3	1.15	89.2	5053	1055	24.8	2.6	229	13.0	12.6	75.8	1.48	5.06	176	259	30.3	88.2	13.2	3.9
RD-11646	Renard	Pipe 3	0.68	78.4	1504	361	21.6	2.3	190	10.0	4.8	90.5	1.56	5.00	167	246	29.2	86.1	12.2	3.0
RD-11649	Renard	Pipe 3	1.25	64.9	479	392	17.7	2.5	192	11.0	4.1	62.7	1.20	6.18	157	224	25.9	74.8	9.9	2.1
RD-11650	Renard	Pipe 3	1.38	48.7	360	271	15.0	1.9	197	11.3	2.9	66.5	1.09	3.85	162	222	25.6	74.2	9.8	2.0
RD-L221-3	Renard	Lynx Dyke	0.15	23.6	1323	789	43.3	5.1	499	31.9	16.6	139.2	4.02	12.46	304	475	57.0	207.8	23.1	5.2
RD-L221-7	Renard	Lynx Dyke	0.24	37.8	955	408	13.1	2.6	201	11.3	10.5	56.9	1.20	5.95	124	162	18.2	52.8	7.5	2.0
RD-L230-5	Renard	Lynx Dyke	0.34	43.2	1134	414	16.9	3.3	280	15.6	12.9	82.7	1.69	7.79	151	236	26.9	80.3	11.8	2.3
RD-L230-6	Renard	Lynx Dyke	0.18	28.8	1249	131	14.3	3.3	202	11.5	46.7	79.1	1.58	5.76	202	289	29.4	78.3	9.1	2.2
RD-H5	Renard	Hibou Sill	0.38	45.5	653	312	11.6	2.5	184	11.1	10.9	48.6	1.19	6.06	94	138	15.6	46.2	7.1	1.5
WEM-02-09 10/1A	Wemindji	Sheet	2.44	20.0	1508	1421	28.4	9.0	292	15.1	36.4	162.2	2.96	17.11	298	392	42.9	139.4	18.2	4.4
WEM-02-09 10/3	Wemindji	Sheet	1.31	19.6	2577	1720	21.5	5.6	330	15.5	79.8	155.4	2.03	16.72	344	466	50.7	190.5	20.7	5.0
WEM-02-09 10/6	Wemindji	Sheet	1.56	23.9	1089	1090	24.2	3.6	284	15.3	13.5	104.1	1.91	13.38	324	494	54.6	197.0	19.8	4.6
WEM-02-09 10/10	Wemindji	Sheet	0.86	21.5	2141	1190	42.1	8.1	422	6.7	6.7	78.4	1.24	23.00	237	438	45.4	182.2	30.6	8.9
WEM-02-10	Wemindji	Sheet	0.96	12.4	317	952	22.5	9.6	252	7.5	3.7	110.3	1.54	20.58	299	376	42.8	138.2	18.2	4.1
WEM-02-22 24	Wemindji	Sheet	0.30	5.9	1352	956	19.0	3.5	326	18.8	14.0	127.6	2.42	15.72	170	255	27.5	84.2	13.7	3.7
WEM-02-22 25	Wemindji	Sheet	0.60	11.1	500	455	11.5	2.0	331	27.9	35.8	80.1	1.92	7.34	82	134	14.5	46.8	6.8	1.8
WEM-02-26 1	Wemindji	Sheet	0.39	7.3	347	538	12.6	2.1	230	15.2	60.9	72.5	1.62	7.69	83	129	14.7	45.1	7.0	1.7
WEM-02-26 2	Wemindji	Sheet	3.26	20.8	1198	758	18.2	3.6	277	15.7	16.4	57.2	1.37	7.79	226	297	32.1	89.9	12.5	3.0
WEM-02-26 3	Wemindji	Sheet	0.74	6.1	434	336	7.4	1.4	329	31.4	38.7	73.2	2.05	5.69	64	103	11.7	39.5	5.3	1.5

Sample ID	Gd	Tb	Dy	Ho	Er	Tm	Yb	Lu	Co*	Cu*	Zn*	Li	Sc*	V*	Ga*	Mo*	W
RD-R2 3	11.1	0.90	3.03	0.37	0.73	0.09	0.49	0.06	89.5	19.3	45.5	1.993	17.23	44.1	3.64	0.05	1.18
RD-R3-07	10.7	0.85	2.82	0.34	0.71	0.09	0.53	0.07	68.0	b.d.	56.5	1.456	11.79	56.4	3.77	0.98	0.69
RD-11646	10.9	0.88	2.94	0.34	0.65	0.07	0.40	0.05	93.2	54.0	85.0	0.614	14.83	47.5	3.26	b.d	0.48
RD-11649	9.9	0.79	2.70	0.33	0.64	0.08	0.44	0.05	82.9	b.d.	36.5	1.886	16.74	35.8	2.32	b.d	0.56
RD-11650	9.4	0.78	2.62	0.33	0.64	0.08	0.43	0.05	91.2	b.d.	34.1	2.395	14.46	32.5	2.65	1.03	0.86
RD-L221-3	20.7	1.71	5.48	0.64	1.26	0.14	0.72	0.09	90.3	199.6	75.1	1.269	37.00	213.5	10.93	0.52	0.87
RD-L221-7	7.1	0.59	2.07	0.26	0.50	0.06	0.36	0.04	108.0	42.6	27.6	0.306	22.22	131.9	4.52	0.53	0.88
RD-L230-5	10.6	0.92	3.19	0.39	0.74	0.09	0.50	0.06	91.6	b.d.	9.3	2.668	26.19	132.6	4.84	0.57	0.98
RD-L230-6	10.0	0.71	2.26	0.26	0.57	0.06	0.33	0.04	90.9	196.1	353.6	0.479	20.87	146.2	3.56	0.85	0.92
RD-H5	6.6	0.56	1.98	0.25	0.46	0.06	0.36	0.05	100.0	b.d.	8.2	0.652	16.63	121.7	3.76	b.d	0.69
WEM-02-09 10/1A	17.5	1.48	5.24	0.68	1.25	0.17	0.87	0.11	105.5	119.6	13.5	15.483	30.70	214.5	5.34	3.28	2.28
WEM-02-09 10/3	19.3	1.54	5.25	0.66	1.30	0.16	0.84	0.11	128.4	205.3	10.4	11.425	33.77	168.1	2.75	2.01	2.93
WEM-02-09 10/6	19.7	1.60	5.31	0.65	1.31	0.17	0.92	0.12	105.8	100.9	14.2	15.074	20.64	143.4	3.15	2.08	3.36
WEM-02-09 10/10	27.2	2.77	10.23	1.24	1.74	0.21	1.00	0.12	33.1	43.6	2.7	7.013	25.73	121.5	6.49	1.11	0.50
WEM-02-10	18.1	1.58	5.91	0.81	1.47	0.22	1.16	0.16	116.0	98.7	17.6	37.374	32.30	118.0	4.07	1.28	1.84
WEM-02-22 24	13.0	1.22	4.79	0.66	1.11	0.17	0.84	0.11	79.3	88.4	67.2	0.464	21.99	154.5	3.73	4.02	2.69
WEM-02-22 25	6.7	0.59	2.14	0.28	0.58	0.07	0.34	0.05	117.2	169.1	34.8	0.645	14.24	149.4	3.90	0.31	1.72
WEM-02-26 1	6.7	0.64	2.48	0.34	0.60	0.09	0.47	0.06	98.8	120.4	90.7	1.035	14.18	106.7	2.55	0.12	3.25
WEM-02-26 2	12.0	0.93	3.01	0.36	0.73	0.08	0.48	0.06	114.9	92.7	6.6	108.43	15.84	131.6	4.09	15.11	1.48
WEM-02-26 3	5.2	0.47	1.71	0.23	0.45	0.06	0.29	0.04	91.4	157.8	212.8	1.374	11.36	182.2	4.25	0.19	0.91

Trace element data are ICP-MS and XRF data determined at the University of the Witwatersrand
*XRF
b.d. = below detection limit.

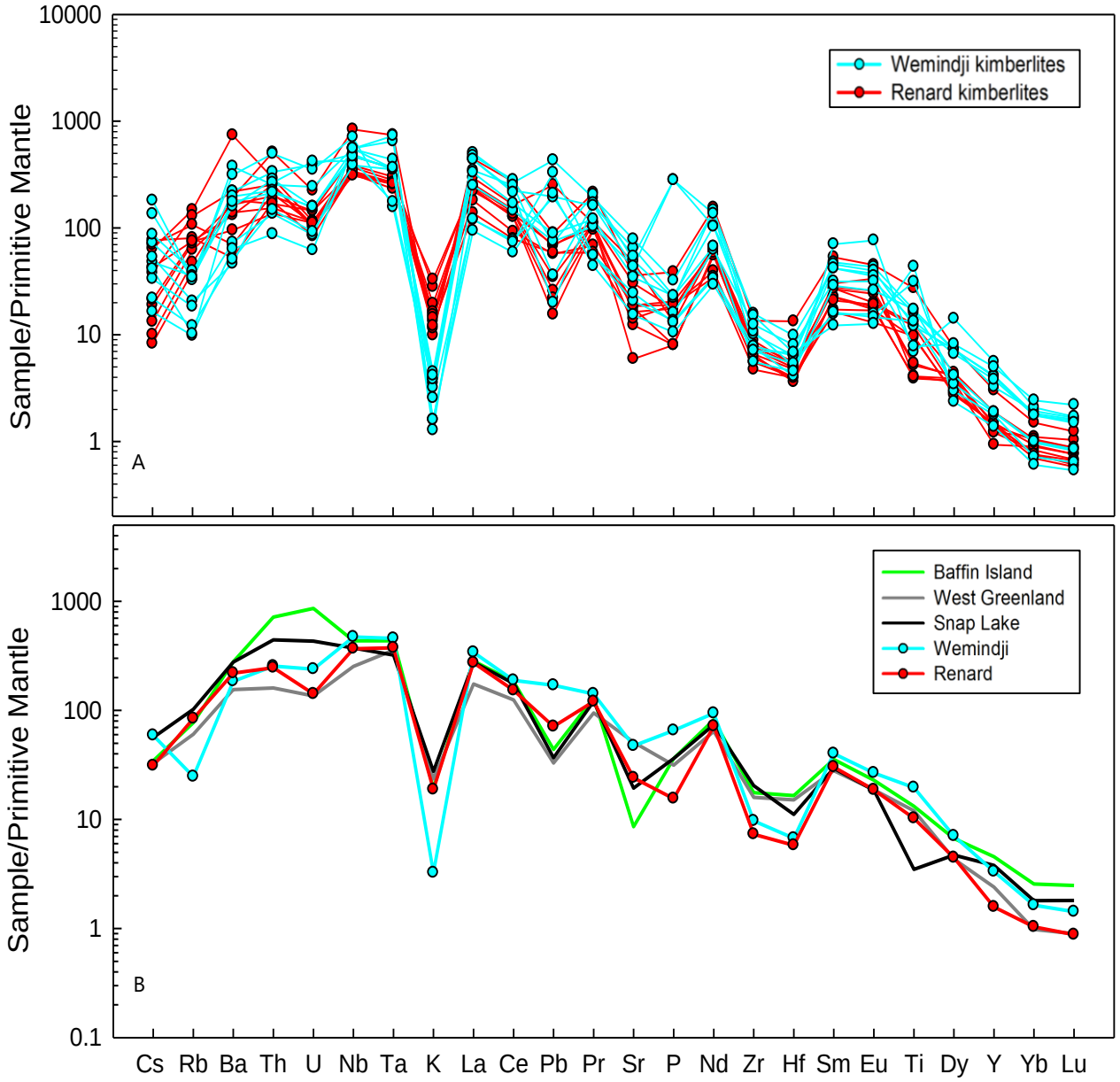

Figure 5: A) Spidergram showing whole rock incompatible element concentrations of magmatic kimberlites from Renard and Wemindji, Quebec. B) Average incompatible element concentrations of the Renard and Wemindji magmatic kimberlite suites compared to averages for West Greenland kimberlite dykes (Tappe *et al*., 2011; Gaffney *et al*., 2007) and other Canadian kimberlite dyke occurrences (Tappe *et al*., 2014; Agashev *et al*., 2008). All concentrations are normalised to the primitive mantle values given in Palme & O'Neill (2003).

Renard kimberlite sample RD-R3-07 has anomalously high Ba (5053 ppm); Lynx kimberlite dyke sample RD-L230-6 contains anomalously low Sr (131 ppm); and Wemindji kimberlite samples WEM-02-09 10/10 and WEM-02-10 contain anomalously high P (~2008 and 2444 ppm, respectively) (Fig. 5 A). Troughs at Zr-Hf in primitive mantle normalized multi-element diagrams are prominent in both kimberlite suites, with Wemindji samples depicting slightly higher abundances of these trace elements (Fig. 5).

The strong Group-1 kimberlite affinity of the Renard and Wemindji kimberlites is further demonstrated by their overlapping Ba/Nb (4.2±1.9 vs. 3.6±2.2) and La/Nb (0.7±0.2 vs. 0.7±0.4) ratios, respectively, which fall within the range of archetypal South African kimberlites and of other members of the Laurentian Kimberlite Province (Fig. 6).

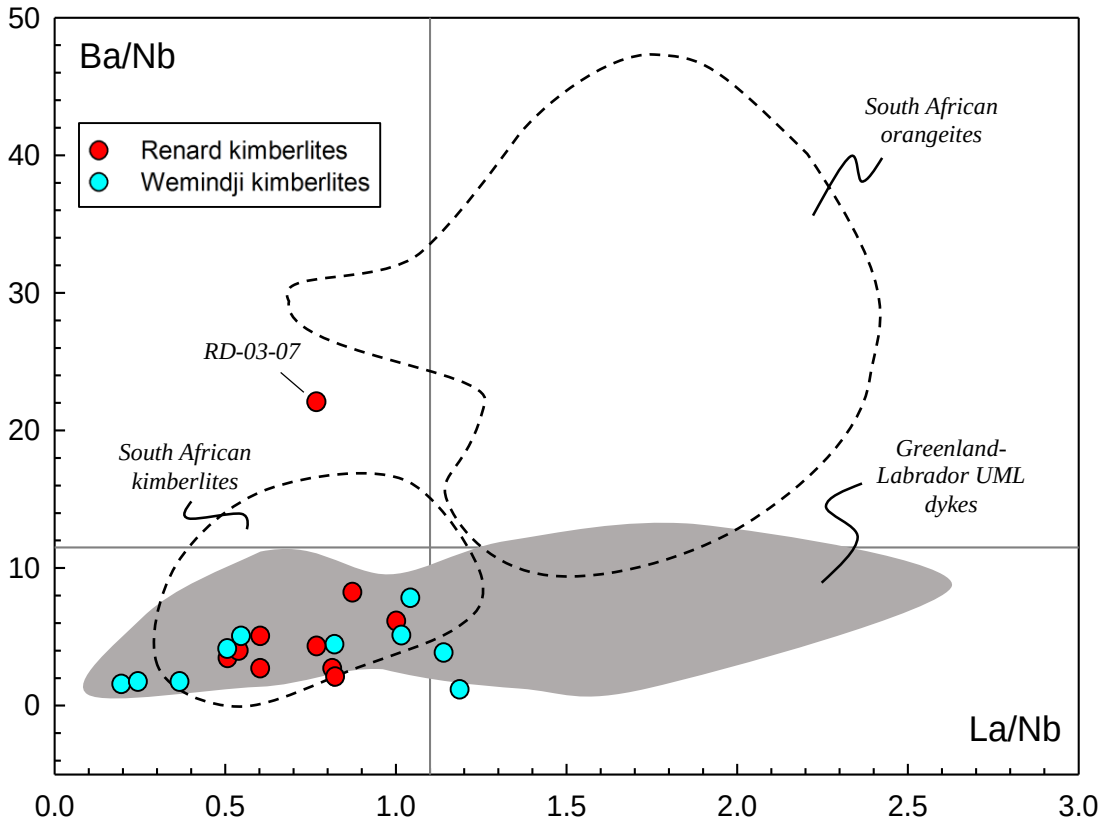

Figure 6: Bulk rock Ba/Nb vs La/Nb for the Renard and Wemindji hypabyssal kimberlites. Fields are plotted for South African kimberlites (Group-1) and South African orangeites (previously known as Group-II kimberlites), along with the dashed lines separating these two kimberlite fields in a broader sense (all taken from Becker and Le Roex, 2006). The field for Greenland-Labrador ultramafic dykes is also shown for comparison (Tappe *et al*., 2008, 2011).

4.2 Bulk rock Highly Siderophile Element concentrations

Highly Siderophile Element (HSE) concentrations were determined for 6 out of the 20 magmatic kimberlite samples from Renard and Wemindji (3 samples each; Table 4, Fig. 7).

Table 4: HSE concentrations (ppb) of hypabyssal magmatic kimberlites from the Renard and Wemindji clusters, Superior craton, Quebec, Canada.

Sample ID	Kimberlite Cluster	Kimberlite Body	Re	Os	Ir	Ru	Pt	Pd
RD-R2 3	Renard	Pipe 2	0.075	0.809	0.581	0.735	0.949	0.381
RD-R3-07	Renard	Pipe 3	0.044	1.118	0.917	1.503	1.369	0.703
RD-11650	Renard	Pipe 3	0.106	0.953	0.684	0.832	1.371	0.270
WEM-02-22 24	Wemindji	Sheet	0.016	0.150	0.146	0.210	0.181	0.173
WEM-02-26 1	Wemindji	Sheet	0.060	0.755	0.652	1.520	2.041	1.005
WEM-02-26 2	Wemindji	Sheet	0.045	1.259	1.189	1.299	0.705	0.405

Osmium concentration was determined by N-TIMS at the University of Vienna, all other Highly Siderophile Element (HSE) concentrations were determined by ICP-MS at the University of Bonn.

The chondrite-normalized HSE patterns are similar for both kimberlite suites, with a general lack of fractionation, apart from a trough at Pd for Renard kimberlite samples RD-R2-3 and RD-R3-07 (normalised Pd values below 0.001). Kimberlite sample WEM-02-22-24 from Wemindji has significantly lower HSE concentrations compared with the Wemindji and Renard kimberlite sample suites. Os concentration is in the Renard kimberlites ranges from 0.809 to 1.118 ppb Os and from 0.150 to 1.259 ppb in the Wemindji kimberlites. Renard also has higher concentrations of Re and Ir. Besides this, there is no clear distinction between the two kimberlite suites in HSE concentration.

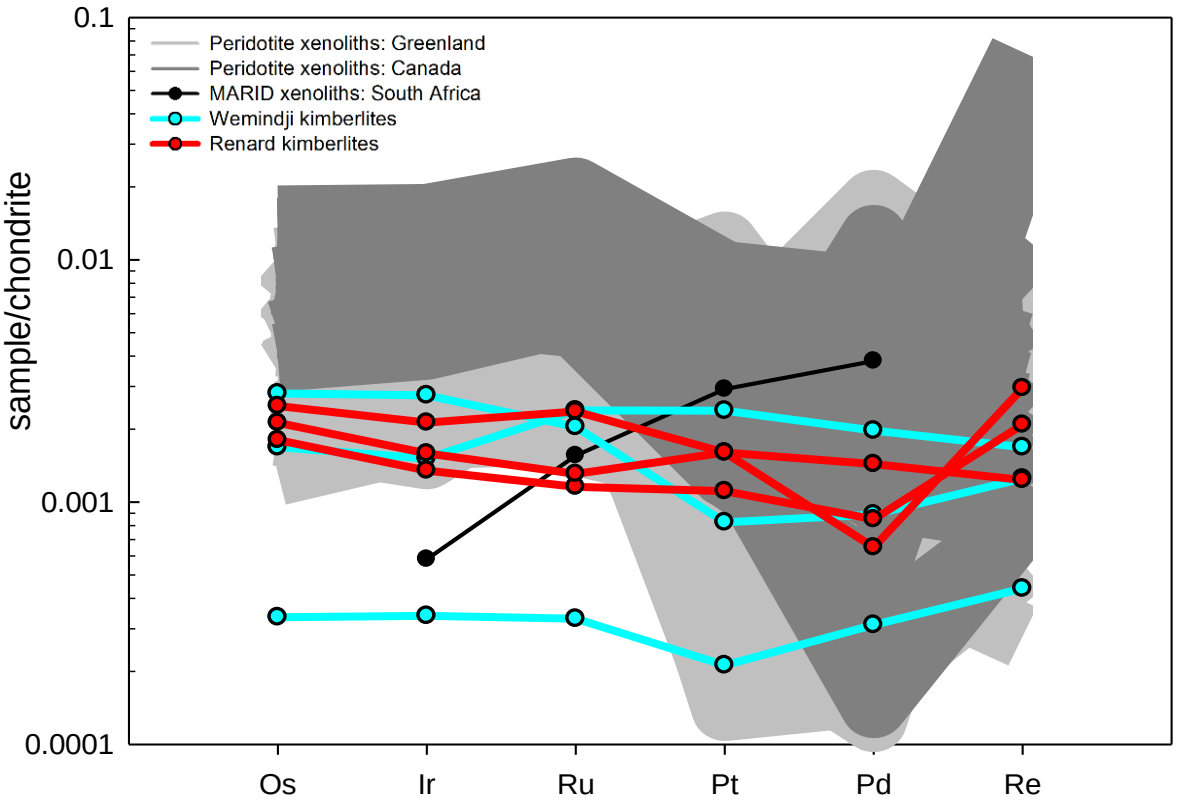

Figure 7: HSE compositions for Renard and Wemindji magmatic kimberlites, in comparison to mantle peridotite xenoliths from Somerset Island, Arctic Canada (Irvine *et al*., 2003) and West Greenland (Wittig *et al.*, 2010) as well as an average for metasomatic mantle-derived MARID xenoliths from South Africa (Maier *et al*., 2012). Chondrite normalising values from Horan *et al*. (2003) and Fischer-Gödde *et al*. (2010).

4.3 Bulk rock Sr-Nd-Hf-Os isotope compositions

All radiogenic Sr-Nd-Hf-Os isotope ratios were calculated at 654 Ma and 629 Ma for the Renard and Wemindji magmatic kimberlites, respectively (Table 5, Fig. 8).

The initial $^{87}Sr/^{86}Sr$ ratios for the Renard kimberlites range between 0.70241 and 0.70765, whereas the Wemindji kimberlites have values between 0.70318 and 0.70970, with significant overlap between both sample suites.

Table 5: Bulk-rock Sr-Nd-Hf-Os as well as carbonate C and O isotope compositions of hypabyssal magmatic kimberlites from the Renard and Wemindji clusters, Superior craton, Quebec, Canada.

Sample ID	Kimberlite Cluster	Kimberlite Body	Age (Ma)	$^{87}Sr/^{86}Sr_m$	2σ	$^{*87}Sr/^{86}Sr_i$	$^{143}Nd/^{144}Nd_m$	2σ	$^{*143}Nd/^{144}Nd_i$	$^{**}\varepsilon Nd_i$	2σ	$^{176}Hf/^{177}Hf_m$	2σ	$^{*176}Hf/^{177}Hf_i$	$^{***}\varepsilon Hf_i$	2σ	$^{187}Os/^{188}Os_m$	2σ	$^{*187}Os/^{188}Os_i$	$^{****}gOs_i$	2σ	$\delta^{13}C$ (‰, VPDB)	2σ	$\delta^{18}O$ (‰, VSMOW)	2σ
RD-R2 3	Renard	Pipe 2	654	0.704744	0.000016	0.70290	0.512298	0.000008	0.51196	3.3	0.48	0.282622	0.000004	0.28255	6.3	0.60	0.121817	0.000414	0.11693	-8.9	0.5	-4.99	0.02	10.05	0.036
RD-R3-07	Renard	Pipe 3	654	0.705767	0.000014	0.70348	0.512242	0.000010	0.51185	1.2	0.46	0.282503	0.000006	0.28242	1.7	0.61	0.117479	0.000403	0.11539	-10.1	0.4	-5.64	0.02	12.54	0.019
RD-11646	Renard	Pipe 3	654	0.708276	0.000013	0.70241	0.512279	0.000011	0.51191	2.4	0.48	0.282518	0.000004	0.28247	3.3	0.62						-8.64	0.01	10.50	0.039
RD-11649	Renard	Pipe 3	654	0.706987	0.000018	0.70252	0.512280	0.000008	0.51194	2.8	0.48	0.282528	0.000006	0.28245	2.8	0.62						-5.16	0.01	18.66	0.021
RD-11650	Renard	Pipe 3	654	0.707393	0.000015	0.70253	0.512292	0.000008	0.51195	3.1	0.47	0.282581	0.000004	0.28250	4.4	0.59	0.132075	0.000488	0.12620	-1.6	0.6	-5.22	0.02	18.53	0.034
RD-L221-3	Renard	Lynx Dyke	654	0.704170	0.000014	0.70336	0.512315	0.000008	0.51203	4.6	0.51	0.282563	0.000005	0.28253	5.4	0.65						-5.24	0.02	11.07	0.035
RD-L221-7	Renard	Lynx Dyke	654	0.705933	0.000015	0.70343	0.512323	0.000006	0.51195	3.2	0.45	0.282567	0.000005	0.28251	4.7	0.62						-4.32	0.02	17.25	0.022
RD-L230-5	Renard	Lynx Dyke	654	0.707183	0.000015	0.70437	0.512327	0.000007	0.51194	3.0	0.44	0.282535	0.000006	0.28247	3.6	0.63						-4.20	0.01	17.34	0.030
RD-L230-6	Renard	Lynx Dyke	654	0.713599	0.000015	0.70765	0.512245	0.000007	0.51194	3.0	0.50	0.282541	0.000005	0.28250	4.4	0.64						-4.22	0.02	19.66	0.027
RD-H5	Renard	Hibou Sill	654	0.706682	0.000016	0.70274	0.512324	0.000008	0.51192	2.6	0.44	0.282578	0.000004	0.28251	4.9	0.61						-4.23	0.01	19.30	0.035
WEM-02-09 10/1A	Wemindji	Sheet	629	0.704791	0.000016	0.70442	0.512221	0.000019	0.51189	1.4	0.45	0.282634	0.000004	0.28257	6.5	0.39						-4.63	0.02	13.37	0.039
WEM-02-09 10/3	Wemindji	Sheet	629	0.704466	0.000016	0.70417	0.512204	0.000006	0.51193	2.1	0.28	0.282620	0.000005	0.28253	5.0	0.40						-4.44	0.02	15.76	0.024
WEM-02-09 10/6	Wemindji	Sheet	629	0.704154	0.000015	0.70358	0.512170	0.000008	0.51192	1.9	0.30	0.282631	0.000003	0.28253	5.0	0.38						-4.08	0.02	13.25	0.024
WEM-02-09 10/10	Wemindji	Sheet	629	0.703673	0.000014	0.70320	0.512486	0.000025	0.51207	4.8	0.54	0.282579	0.000002	0.28258	1.1	0.37						-4.18	0.02	11.15	0.040
WEM-02-09 10/10d	Wemindji	Sheet	629								0.54	0.282557	0.000004	0.28256	0.3	0.38									
WEM-02-10	Wemindji	Sheet	629	0.710043	0.000014	0.70970	0.512200	0.000009	0.51187	0.9	0.30	0.282338	0.000005	0.28217	-7.7	0.40						-3.88	0.02	18.97	0.023
WEM-02-22 24	Wemindji	Sheet	629	0.703339	0.000016	0.70318	0.512369	0.000005	0.51196	2.7	0.26	0.282592	0.000005	0.28252	4.7	0.39	0.122607	0.000177	0.11729	-10.0	0.5	-4.81	0.02	13.26	0.027
WEM-02-22 25	Wemindji	Sheet	629	0.703868	0.000015	0.70324	0.512360	0.000007	0.51200	3.4	0.28	0.282585	0.000005	0.28255	5.6	0.40						-4.50	0.01	14.94	0.042
WEM-02-26 1	Wemindji	Sheet	629	0.703740	0.000015	0.70339	0.512366	0.000010	0.51198	3.0	0.30	0.282600	0.000005	0.28254	5.4	0.39	0.119562	0.000654	0.11550	-13.7	0.6	-4.79	0.02	13.97	0.031
WEM-02-26 2	Wemindji	Sheet	629	0.705136	0.000013	0.70442	0.512177	0.000009	0.51183	0.2	0.30	0.282542	0.000002	0.28254	2.9	0.36	0.112584	0.000305	0.11078	-8.6	0.3	-3.95	0.02	16.62	0.031
WEM-02-26 3	Wemindji	Sheet	629	0.704269	0.000015	0.70380	0.512351	0.000007	0.51201	3.8	0.28	0.282591	0.000005	0.28256	6.1	0.40						-4.55	0.02	14.29	0.022

d=duplicate

Sr isotope compositions were determined by TIMS, and Nd and Hf isotope compositions were determined by MC-ICPMS at WWU Münster.

Os isotope compositions were determined by TIMS at the University of Vienna. C and O isotope compositions of bulk rock carbonates were determined at WWU Münster.

Measured Sr, Nd, and Hf isotope ratios are normalized to the following standard values:

NBS987 = 87Sr/86Sr value of 0.710243 (Thirlwall, 1991); La Jolla 143Nd/144Nd value of 0.511840; AMES = 176Hf/177Hf value of 0.282160 (Blichert-Toft et al., 1997).

Average standard values obtained during this study are:

NBS987 = 87Sr/86Sr value of 0.710245(32), n=11.

La Jolla = 143Nd/144Nd value of 0.511824(32), n=20; AGV-2 = 143Nd/144Nd value of 0.512770(25), n=7; BCR-2 = 143Nd/144Nd value of 0.512622(19), n=7; BHVO-2 = 143Nd/144Nd value of 0.512958(19), n=7.

AMES = 176Hf/177Hf value of 0.282148(16), n=19; AGV-2 = 176Hf/177Hf value of 0.282980(3), n=3; BCR-2 = 176Hf/177Hf value of 0.282867(3), n=3; BHVO-2 = 176Hf/177Hf value of 0.283104(15), n=3.

The standard value measured for Os was BIR-1 = 187Os/188Os value of 0.1218(3), n=1.

*Initial isotope ratios calculated for the emplacement ages of 654 Ma for the Renard kimberlite cluster (see Section 4.6) and 629 Ma for the Wemindji kimberlite sills (Letendre et al., 2003).

**Initial epsilon Nd values were calculated using 147Sm decay constant of 6.54*10-12 a-1 (Lugmair and Marti, 1978); (143Nd/144Nd)CHUR = 0.512630 and (147Sm/144Nd)CHUR = 0.1960 (Bouvier et al., 2008).

***Initial epsilon Hf values were calculated using 176Lu decay constant of 1.865*10-11 a-1 (Scherer et al., 2001); (176Hf/177Hf)CHUR = 0.282785 and (176Lu/177Hf)CHUR = 0.0336 (Bouvier et al., 2008).

****Initial gamma Os values were calculated using 187Re decay constant of 1.6668*10-11 (Selby et al., 2007), (187Os/188Os)Mantle = 0.1283 and (187Re/188Os)Mantle = 0.422 (Walker et al., 2002).

The 2-sigma uncertainties of the epsilon Nd and Hf values, as well as of the gamma Os values, entail a full error propagation following Ickert (2013). The uncertainties of the emplacement age and parent-daughter element ratios were set at 10%.

However, sample RD-L230-6 from the Lynx kimberlite dyke of the Renard cluster has the highest initial $^{87}Sr/^{86}Sr$ ratio (0.70765) of the respective kimberlite suite, which corresponds to an elevated Pb concentration (46.7 ppm Pb), suggestive of some minor crustal contamination (Fig. 8 B). This reduces the primary Sr isotope compositional range for the Renard kimberlites to 0.70241-0.70437. Furthermore, the maximum initial $^{87}Sr/^{86}Sr$ ratio for the Wemindji kimberlites corresponds with other evidence of crustal contamination (sample WEM-02-10; Fig. 8 B; Section 4.1), which reduces the primary Sr isotope compositional range to 0.70318-0.70442.

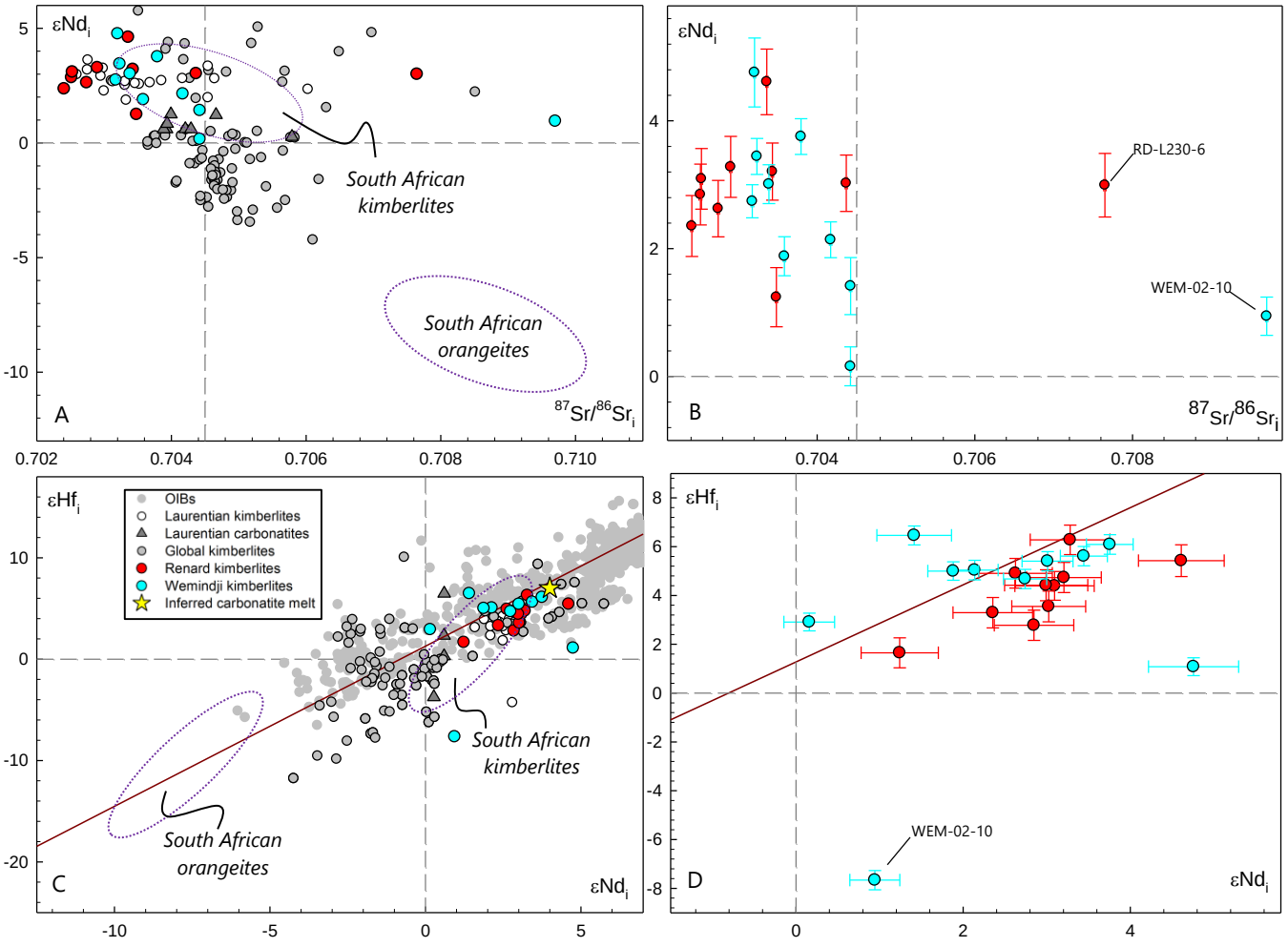

Figure 8: A-B) Sr-Nd and C-D) Nd-Hf isotope diagrams for magmatic kimberlites from Renard and Wemindji. Global ocean island basalts (OIBs) (Stracke, 2012); Southern African kimberlites (Nowell *et al.*, 2004); Southern African orangeites (Nowell *et al.*, 2004; Coe *et al.*, 2008); global kimberlites (Paton *et al.*, 2009 - India; Kopylova *et al.*, 2009 - Jericho; Yang *et al.*, 2009 - China; Carlson *et al.*, 2006 - Siberia; Yaxley *et al.*, 2013 – Antarctica; Tappe *et al.*, 2013 – Slave craton); "Laurentian" Neoproterozoic kimberlites, carbonatites and UMLs (Gaffney *et al.*, 2007; Tappe *et al.*, 2011 - West Greenland; Tappe *et al.*, 2014 – Baffin Island; Tappe *et al.*, 2007, 2008 –Labrador). Mantle array (red line) after Chauvel *et al.* (2008). The yellow star indicates an inferred low-degree carbonate-rich melt component of the convecting upper mantle that was widespread beneath cratonic Laurentia during the Late Neoproterozoic (Tappe *et al.*, 2011).

Initial ε_{Nd} values for the Renard kimberlites lie between +1.2 and +4.6, whereas values for the Wemindji kimberlite sills range between +0.2 and +4.8, with significant overlap between both sample suites. In Sr-Nd isotopic space, both the Renard and Wemindji kimberlites are mildly depleted (Fig. 8 A, B).

Initial ε_{Hf} values for the Renard kimberlites lie between +1.7 and +6.3, whereas the Wemindji kimberlite sills yielded values between +0.3 and +6.5, again, with significant overlap between sample suites (excluding sample WEM-02-10 with an initial ε_{Hf} value of -7.7, most likely caused by crustal contamination – see Section 4.1). Both the Renard and Wemindji kimberlites suites fall within the mantle array in Nd-Hf isotopic space (Fig. 8 C, D), with the Renard kimberlites exhibiting a less scattered trend than the Wemindji kimberlites.

Osmium isotope compositions of the Renard and Wemindji magmatic kimberlites fall at the unradiogenic end for global kimberlites (cf., Pearson *et al*., 2007), with initial $^{187}Os/^{188}Os$ ratios ranging between 0.11539 and 0.12620 and between 0.11078 and 0.11729, respectively (Fig. 9).

Calculated γOs_i values for the Renard and Wemindji kimberlites range between -10.1 and -1.6, and between -13.7 and -9.6, respectively. Renard sample RD-11650 contains the highest concentration of Re (0.106 ppb) among the analysed samples. This kimberlite sample also has the highest measured $^{187}Os/^{188}Os$ ratio (0.13208) and the highest initial γOs value (-1.6) among the six samples analysed. Crustal contamination can be excluded as the cause of this slightly more radiogenic Os isotope composition based on the fact that the major- and trace element compositions, as well as Sr-Nd-Hf isotope compositions do not reveal any evidence for crustal input to the kimberlite magma.

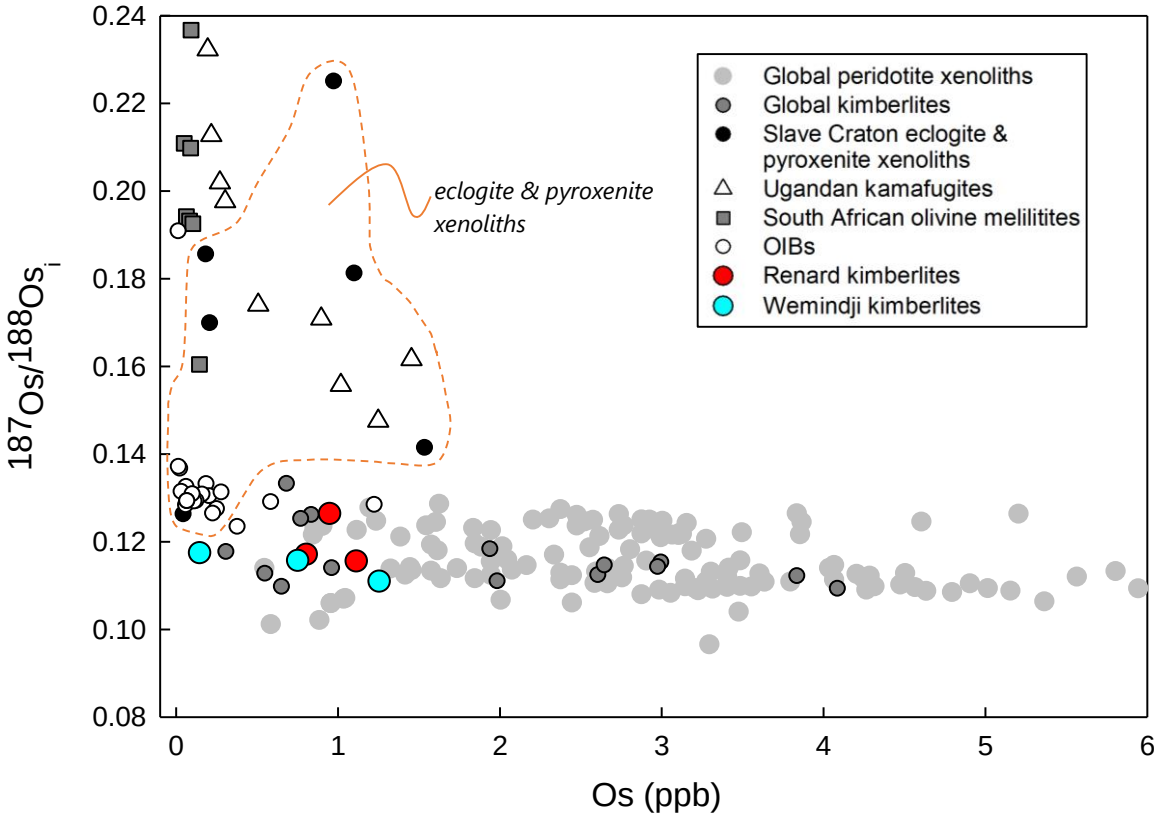

Figure 9: Osmium isotope composition and concentration of Renard and Wemindji magmatic kimberlites, compared to global mantle-derived peridotite and eclogite/pyroxenite xenoliths (Meisel *et al*., 2001 – USA, Mexico, Alaska, Hawaii, Australia, Africa; Irvine *et al*., 2003 - Somerset Island peridotite xenoliths (Canada); Carlson *et al*., 2007 - Brazilian peridotite xenoliths; Aulbach *et al*., 2009 - eclogite and pyroxenite xenoliths (Slave Craton); Wittig *et al*., 2010 - peridotite xenoliths (West Greenland); global magmatic kimberlites (Carlson *et al*., 2007 - Brazil; Rao *et al*., 2013 - India); Ugandan kamafugites (Rosenthal *et al*., 2009); olivine melilitites (Janney *et al*., 2002); ocean island basalts (OIBs) (Debaille *et al*., 2009 - Iceland; Jackson & Shirey, 2011 - Samoa). Osmium isotope compositions of xenoliths were calculated for 650 Ma in order to be comparable with the Late Neoproterozoic kimberlites studied here.

4.4 Bulk rock carbonate C-O isotope compositions

The $\delta^{13}C$ values of the carbonate fractions of the Renard kimberlites (-5.6 to -4.2 ‰; RD-11646 at -8.6 ‰ $\delta^{13}C$ with very low CO_2 content of 2.64 wt. %) are slightly lower compared with the Wemindji kimberlite carbonates (-4.8 to -3.9 ‰), falling within the range of mantle carbon isotope compositions

(Deines, 2002) (Table 5; Fig. 10). In contrast, Renard and Wemindji magmatic kimberlite carbonates have overlapping $\delta^{18}O$ values between 10.1 and 19.7 ‰, and between 11.2 and 19.0 ‰, respectively, clearly outside the range of pristine mantle values (Fig. 10

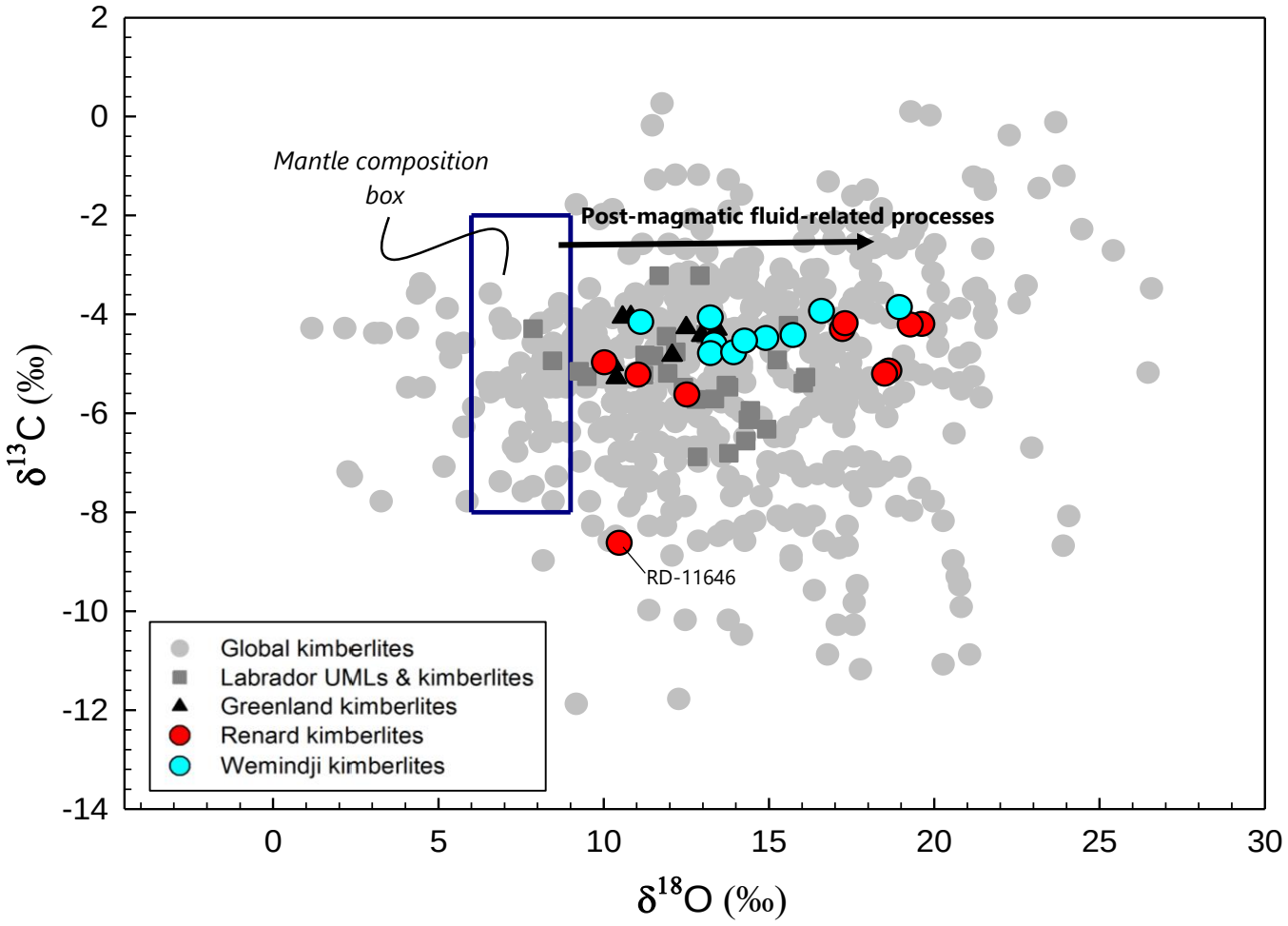

Figure 10: Carbon and oxygen isotope compositions of groundmass carbonates from the Renard and Wemindji magmatic kimberlites, as compared to global kimberlites (data compilation from Giuliani *et al*., 2014). Data for Greenland kimberlites (Tappe *et al*., 2011) and Labrador UMLs and carbonatites (Tappe *et al*., 2006, 2008) as part of the Laurentian Kimberlite Province are also shown. The black arrow is indicative of expected variation in $\delta^{18}O$ due to post-magmatic hydrothermal or low-temperature meteoric fluid interaction (Demeny *et al*., 1998). Mantle carbonate box from Giuliani *et al.*, 2014, after Clarke *et al*, 1994 and Demeny *et al.*, 1998).

4.5. U-Pb perovskite age measurements

More than 15 years after its discovery, the timing of magma emplacement in the Renard kimberlite suite of the eastern Superior craton is surprisingly poorly constrained. Birkett *et al*. (2004) mentioned a $^{206}Pb/^{238}U$ perovskite age of 631.6 ± 3.5 Ma for hypabyssal kimberlite material from Renard Pipe-1, but no data and no supporting documentation were provided.

McCandless *et al*. (2008) mentioned emplacement ages between 645-630 Ma for the Renard kimberlite cluster in a conference abstract, without any detail provided. These authors also cite an undocumented 522 ± 30 Ma U-Pb isochron age for groundmass ilmenite from the Lynx kimberlite dyke, which occurs only 2 km west of the nine known Renard kimberlite pipes. Muntener and Scott-Smith (2013) mentioned a $^{206}Pb/^{238}U$ perovskite age of 640.5 ± 2.8 Ma for Renard Pipe-2 and Pipe-3, but in the absence of any documentation and data tables, it is impossible to assess the quality and geological meaning of the quoted U-Pb date.

Two new U-Pb perovskite ages for hypabyssal kimberlite material from Renard Pipe-2 and Pipe-3 by ion-microprobe analysis have been determined (Table 6). For Pipe-2, kimberlite sample RD-R2-19 yielded a weighted average $^{206}Pb/^{238}U$ perovskite age of 655.8 ± 6.0 Ma, which is identical within analytical uncertainty to the U/Pb Concordia age of 652.6 ± 5.7 Ma (Fig. 11 A, B). For Pipe-3, kimberlite sample RD-11646 yielded a weighted average $^{206}Pb/^{238}U$ perovskite age of 653.8 ± 5.9 Ma, which is identical to the U/Pb Concordia age of 653.7 ± 6.0 Ma (Fig. 11 C, D).

The analysed perovskite fractions from Pipe-2 (11 single grains) and Pipe-3 (10 single grains) have similar U contents between 68 and 153 ppm and similar common Pb contents (6.6-13.8% of ^{206}Pb is composed of common Pb). However, groundmass perovskite from Pipe-2 has on average higher Th/U ratios compared with perovskite from Pipe-3 (33-116 vs. 2.8-85.3 Th/U). In any case, the Th/U ratios of the perovskites from Renard magmatic kimberlites are very

Table 6: SIMS U-Pb perovskite age results for hypabyssal kimberlite samples from Renard Pipe-2 and Renard Pipe-3, Superior craton, Quebec, Canada.

Sample ID / Spot#	SIMS Session	Apparent Ages (Ma)											Wetherill Concordia (TCPb corrected)				
		$^{207}Pb/^{206}Pb$	±σ	$^{207}Pb/^{235}U$	±σ	$^{206}Pb/^{238}U$	±σ	U (ppm)	Th (ppm)	Th/U	$^{206}Pb/^{204}Pb$(m)	f_{206}%	$^{207}Pb/^{235}U$	±σ %	$^{206}Pb/^{238}U$	±σ %	rho
Renard Pipe-2																	
WA $^{206}Pb/^{238}U$ Age = 655.8±6.0 Ma (2 σ)																	
RD-R2-19@1	25/26 Nov. 2014	422.2	362.5	609.2	87.5	660.7	9.7	83	3280	39.7	144.0	13.0	0.8221	18.3	0.1079	1.6	0.0848
RD-R2-19@3	25/26 Nov. 2014	644.4	185.0	648.6	45.4	649.8	9.3	126	4201	33.3	188.4	9.9	0.8942	9.3	0.1061	1.5	0.1625
RD-R2-19@4	25/26 Nov. 2014	913.1	168.6	717.7	46.2	656.7	9.5	108	7687	71.5	179.6	10.4	1.0275	8.8	0.1072	1.5	0.1724
RD-R2-19@6	25/26 Nov. 2014	909.9	192.8	724.5	53.6	666.1	9.7	94	10956	116.3	156.1	12.0	1.0412	10.1	0.1088	1.5	0.1517
RD-R2-19@7	25/26 Nov. 2014	526.5	247.4	639.5	60.2	672.0	10.3	109	11473	105.2	145.4	12.9	0.8773	12.3	0.1099	1.6	0.1306
RD-R2-19@8	25/26 Nov. 2014	575.3	244.2	641.5	59.9	660.5	9.5	96	8853	92.6	146.9	12.7	0.8810	12.2	0.1079	1.5	0.1233
RD-R2-19@9	25/26 Nov. 2014	676.4	223.2	636.1	55.0	624.8	9.2	123	11173	90.5	139.4	13.4	0.8709	11.3	0.1018	1.5	0.1362
RD-R2-19@11	25/26 Nov. 2014	411.9	247.4	606.4	56.6	659.7	9.4	110	10585	95.9	151.5	12.4	0.8170	12.1	0.1077	1.5	0.1246
RD-R2-19@12	25/26 Nov. 2014	248.0	290.6	563.4	62.0	644.6	9.3	107	11221	105.3	142.9	13.1	0.7418	13.9	0.1052	1.5	0.1085
RD-R2-19@13	25/26 Nov. 2014	743.1	138.1	664.4	34.7	641.4	9.2	151	10623	70.1	224.7	8.3	0.9239	7.0	0.1046	1.5	0.2147
RD-R2-19@14	25/26 Nov. 2014	240.9	294.2	566.9	63.1	651.4	9.3	105	11251	107.5	138.0	13.6	0.7478	14.1	0.1063	1.5	0.1065
Renard Pipe-3																	
WA $^{206}Pb/^{238}U$ Age = 653.8±5.9 Ma (2 σ)																	
RD-11646@1	8/9 March 2012	806.5	141.7	694.3	37.1	660.1	9.4	153	426	2.8	275.2	6.8	0.9813	7.2	0.1078	1.5	0.2074
RD-11646@3	8/9 March 2012	956.2	205.5	737.9	58.6	668.1	9.6	68	2854	41.7	177.6	10.5	1.0683	10.9	0.1092	1.5	0.1387
RD-11646@4	8/9 March 2012	494.6	248.4	620.0	58.7	654.9	9.4	87	4657	53.4	171.2	10.9	0.8416	12.3	0.1069	1.5	0.1222
RD-11646@5	8/9 March 2012	491.1	247.2	613.1	57.9	646.6	9.3	89	1092	12.2	190.4	9.8	0.8290	12.2	0.1055	1.5	0.1231
RD-11646@6	8/9 March 2012	933.0	136.8	721.4	37.5	655.3	9.4	147	5967	40.6	281.7	6.6	1.0350	7.1	0.1070	1.5	0.2105
RD-11646@9	8/9 March 2012	590.1	243.6	636.7	59.6	649.8	9.3	94	3809	40.6	177.9	10.5	0.8720	12.2	0.1061	1.5	0.1230
RD-11646@10	8/9 March 2012	*infinite*	333.1	520.9	64.6	649.2	9.4	110	9375	85.3	160.9	11.6	0.6704	15.4	0.1060	1.5	0.0991
RD-11646@11	8/9 March 2012	629.4	282.9	642.5	71.3	646.2	9.3	92	1314	14.3	170.9	10.9	0.8828	14.5	0.1054	1.5	0.1040
RD-11646@12	8/9 March 2012	953.2	207.7	721.4	58.3	649.2	9.3	117	8848	75.4	221.0	8.5	1.0350	11.0	0.1059	1.5	0.1374
RD-11646@13	8/9 March 2012	822.5	200.0	697.5	53.5	659.4	9.4	114	650	5.7	212.1	8.8	0.9876	10.3	0.1077	1.5	0.1456

U/Pb ages were calculated using Isoplot 2.2 (Ludwig, 2000); TCPB - total initial common Pb.

Uncertainties are quoted at 1-sigma except for the final age results, where uncertainties are given at the 2-sigma level; WA - weighted average.

The f_{206}% values denote the percentage of initial common ^{206}Pb on Pb mass 206 as estimated from the measured ^{204}Pb contents and the terrestrial Pb evolution model of Stacey & Kramers (1975).

Natural perovskite mineral standards (Ice River, Tazheran-3, Afrikanda-5; see Supplementary Data Table 1) were analyzed as secondary reference materials to ensure accuracy of the in-situ SIMS method (Cameca IMS-1280; Li et al., 2010).

Photomicrographs of Renard hypabyssal kimberlite samples RD-R2-19 (Pipe-2) and RD-11646 (Pipe-3) are shown in Figure 3 to document the petrographic context of the analyzed groundmass perovskite grains.

typical for kimberlitic perovskites (see compilation of perovskite trace element data from global kimberlite occurrences, Wu *et al.*, 2010).

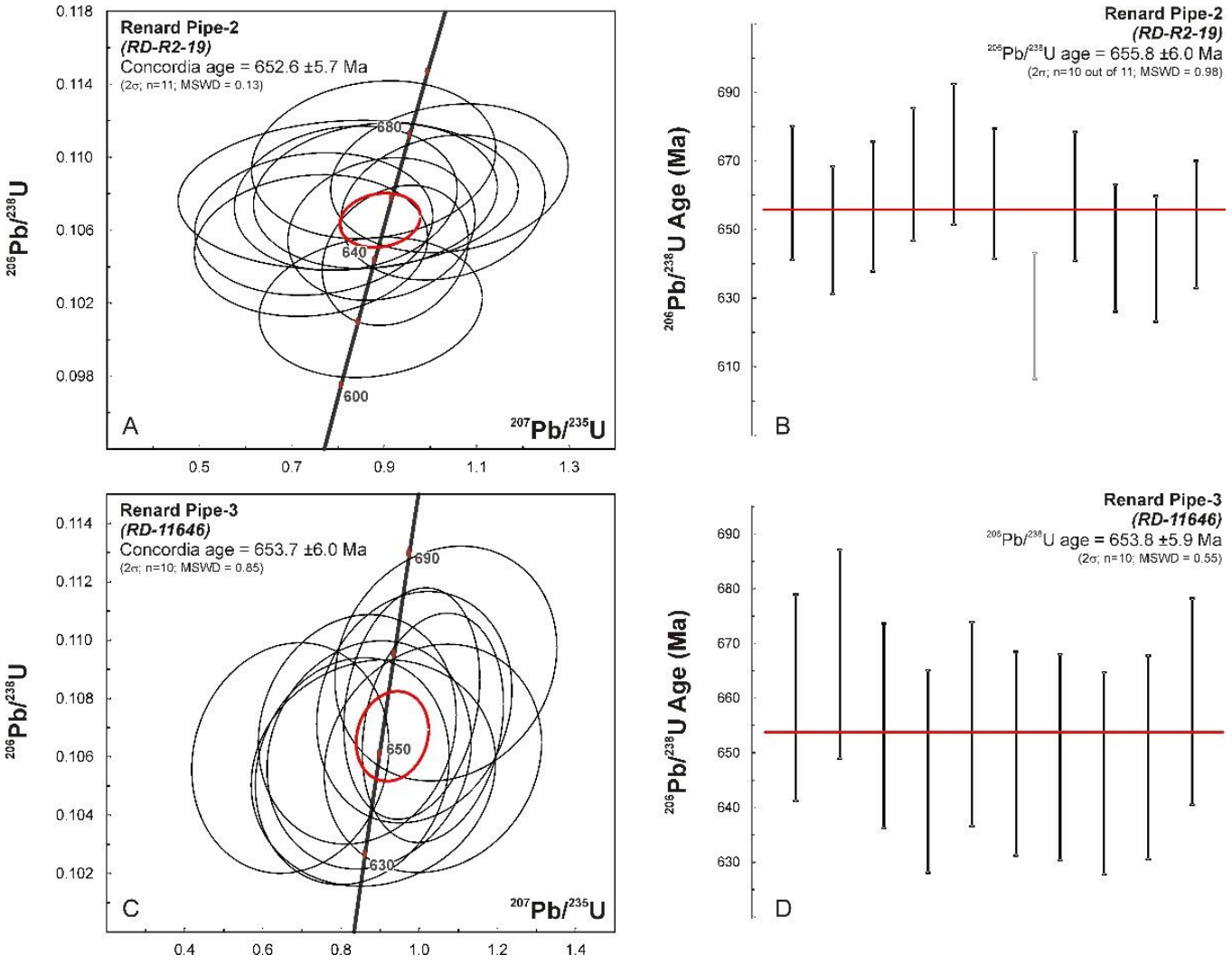

Figure 11: U-Pb Concordia age diagrams for perovskites from kimberlites from Renard Pipe-2 (A, B) and Renard Pipe-3 (C, D). All analyses displayed are listed in Table 6, with measured standard material available in Appendix D.

5. Interpretation of Geochemical and Isotopic Data

5.1 Bulk rock major- and trace element geochemical features

Hypabyssal kimberlite samples from the Renard pipes and dykes and the Wemindji sills fall consistently within the range of major element compositions for kimberlites from worldwide occurrences including other localities of the Laurentian Kimberlite Province in Canada and West Greenland (Fig. 1). The Wemindji kimberlite samples lie on the very low end of SiO_2 and Al_2O_3 global concentrations, and they have elevated TiO_2. Elevated bulk kimberlite TiO_2 concentrations can be attributed to presence of abundant groundmass and xenocrystic ilmenite (Appendix B). In detail, there are subtle differences in the bulk rock major- and trace element compositions between the Renard and Wemindji kimberlite sample suites.

The Renard kimberlite samples are geochemically more tightly constrained, which is in good agreement with their relatively petrographically homogenous nature compared with the more diverse, flow-differentiated Wemindji kimberlite sill samples (cf., Zurevinski and Mitchell, 2011). The only major element characteristic that is completely distinct, with no overlap, is the K_2O content of the Renard magmatic kimberlites studied here (0.31-1.03 wt. % K_2O; Fig. 4 E), which shows a larger spread compared with the Wemindji kimberlite sills (0.04-0.14 wt. % K_2O). These concentrations coincide with the higher abundance of groundmass phlogopite in the Renard kimberlites than in the Wemindji kimberlites (see Appendix A and B). However, the observed K_2O spread for the Renard kimberlites is comparable to other kimberlite sample suites from worldwide occurrences (Kjarsgaard *et al*., 2009) including examples from the Laurentian Kimberlite Province in Canada (Tappe *et al*., 2014; Agashev *et al*., 2008) and West Greenland (0-1.76 wt. % K_2O; Fig. 4 E) (Gaffney *et al*., 2007; Tappe *et al*., 2011).

Due to the high primary magmatic carbonate abundances in the Wemindji kimberlite sills, the Wemindji samples have distinctly higher CO_2 concentrations

compared with the Renard hypabyssal kimberlite samples (Fig. 4 F). In contrast, the higher concentrations of SiO_2, Al_2O_3, MgO, and K_2O in the Renard kimberlites correspond to elevated modal abundances of olivine and phlogopite compared to the Wemindji sheets (Fig. 4; Appendix A).

The Renard and Wemindji hypabyssal kimberlites show overall similar primitive mantle-normalized incompatible element distributions, which are comparable to other worldwide hypabyssal kimberlite suites (Fig. 5). Although both the Renard and Wemindji sample suites exhibit negative K anomalies relative to neighbouring HFSEs and LREEs, the Wemindji kimberlites show a more pronounced K depletion compared with their Renard analogues. As mentioned above, the Wemindji kimberlite sills are flow-differentiated, have more evolved microphenocryst compositions, and show more variable major- and trace element compositions compared with the Renard hypabyssal kimberlites. Consequently, only the incompatible element distributions for the Renard samples are near primary, and may be used to reveal insights into the mantle source mineralogy and the kimberlite melt formation process beneath the eastern Superior craton during the Late Neoproterozoic.

Relative K depletions are common among primitive, mantle-derived low-volume magmas such as kimberlites, UMLs, and melilitites, and may be caused by residual phlogopite in the peridotitic mantle source region (Rogers *et al*., 1992; Wilson *et al*., 1995; Le Roex *et al*., 2003; Tappe *et al*., 2006). Residual amphiboles in the mantle source may also play a role in relative K depletions of primitive melts, but known amphibole/melt trace element partitioning would result in high Rb/Ba ratios (Class and Goldstein, 1997), which is not observed in the Renard magmatic kimberlites. This cannot be applied to the Wemindji kimberlites due to their differentiated nature.

Based on geochemical modelling, the relative Zr-Hf depletions or “troughs” relative to concentrations of neighbouring LREE have been suggested to be produced by low-degrees of partial melting of fertile peridotitic upper mantle in the presence of CO_2 (Tappe *et al*., 2011, 2013).

Importantly, the relatively immobile Ba/Nb and La/Nb trace element systematics (Fig. 6) rule out, or greatly restrict, kimberlite melt origins from potassic metasomes beneath the eastern Superior craton (i.e., Renard and Wemindji) as was demonstrated for South African orangeites (Ba/Nb = 10-40; La/Nb = 1.2-2.2; Becker and Le Roex, 2006) and the majority of Greenland-Labrador ultramafic lamprophyres (Ba/Nb = 2-14; La/Nb = up to 2.7; e.g., Tappe *et al*., 2008, 2011) of the Laurentian Kimberlite Province.

The Renard and Wemindji magmatic kimberlites have HSE concentrations that overlap with the lower end of the concentration range of kimberlite-borne peridotite xenoliths from Arctic Canada (Tappe *et al*., 2014; Agashev *et al*., 2008) and West Greenland (Tappe *et al*., 2011; Gaffney *et al*., 2007). Unfortunately, HSE concentration data for hypabyssal kimberlites are lacking in the international literature, which is mainly due to the assumption that HSE-budgets of kimberlites are largely derived from entrained mantle peridotite xenoliths and, thus, have only limited value for kimberlite magma petrogenesis (see Os isotope modelling in Section 5.2.1).

However, the chondrite-normalized HSE patterns of Renard and Wemindji magmatic kimberlites differ from those of mantle-derived peridotite xenoliths (Fig.7). They are relatively flat and suggest that only little to no HSE fractionation has occurred during mantle melting. The similar normalized HSE distributions point to a similar degree of partial melting of comparable peridotitic mantle source material.

Scarce HSE patterns for type MARID (mica-amphibole-rutile-ilmenite-diopside) xenoliths from South Africa show an opposite slope compared with the chondrite-normalized HSE patterns of kimberlites and mantle-derived peridotites (average MARID values from Maier *et al*., 2012; Fig. 7). Moreover, Os concentrations are assumed to be below detection or near the detection limit based on extrapolation of the slope (Maier *et al*., 2012), which additionally rules out strongly melt-metasomatized cratonic mantle lithologies, such as MARID, as a significant kimberlite source component.

Olivine crystal-liquid fractionation is modelled in Figure 12 (after Le Roex *et al*., 2003) utilizing hypabyssal kimberlite Ni contents and Mg/Fe ratios (i.e., Mg-number). Le Roex *et al*. (2003) used this model to demonstrate the evolutionary differences between aphanitic and macrocrystic hypabyssal kimberlite samples from Kimberley, South Africa.

Olivine fractionation curves in Figure 12 were calculated by Le Roex *et al.* (2003), assuming equilibrium crystallisation. The aphanitic kimberlites in their study demonstrate a near-perfect relationship between fractionated aphanitic kimberlites and the olivine fractionation curve. Applied to this study, the Renard and Wemindji magmatic kimberlite samples fall somewhat along the olivine fractionation/accumulation trends. However, it is clear that the visually more differentiated Wemindji kimberlite samples, with significantly less olivine macrocrysts (Appendix B), have lower Ni concentrations compared to Renard kimberlites. The Wemindji kimberlite sill samples fall within the range and slightly above and below an inferred parental kimberlite magma composition and more toward the olivine fractionation trend (Fig. 12). In contrast, the Renard hypabyssal kimberlite samples contain significantly more Ni, and they follow a trend of olivine and/or peridotite accumulation according to Le Roex *et al*. (2003).

This is consistent with the abundance of olivine macrocrysts in the Renard kimberlites (Appendix A). As illustrated in Figure 12, the majority of kimberlite samples from both Renard and Wemindji have Mg-numbers within the range of proposed parental kimberlite magmas (Mg# between 82 and 89; le Roex *et al*., 2003; Kjarsgaard *et al*., 2009). This suggests that despite the observed flow textures and olivine removal/ accumulation, the investigated hypabyssal kimberlites from the eastern Superior craton are not far removed from primitive magma compositions.

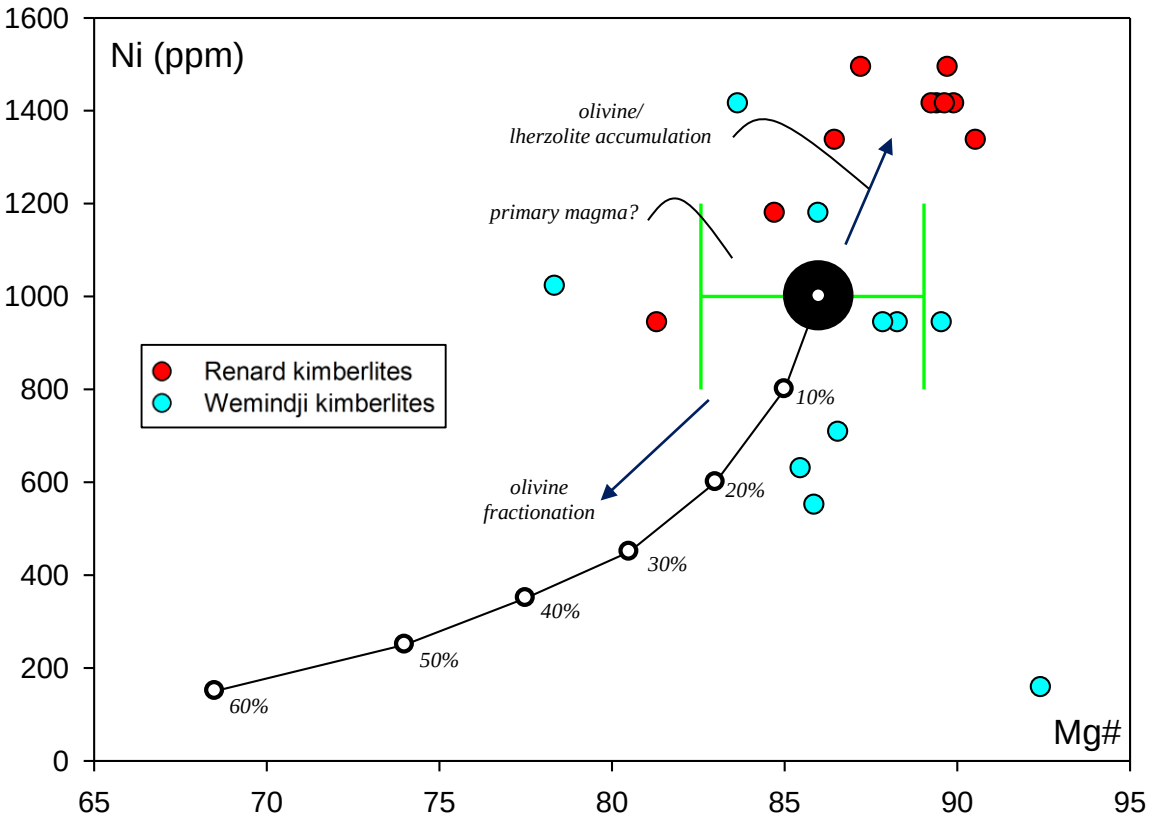

Figure 12: Ni vs. Mg# plot for Renard and Wemindji magmatic kimberlites. Major element fractionation model after Le Roex *et al*. (2003) demonstrating the effect of olivine fractionation vs. olivine/lherzolite accumulation from a parent kimberlite magma. Mg# is calculated as $(Mg/(Mg+Fe^{2+}))$ x 100. Black circle represents a composition of an inferred primary magma (saturated in ~Fo_{95} olivine; with a calculated Ni content of ~950-1000 ppm, further explained in Section 5.1 and le Roex *et al*., 2003). The green bar represents a range of Mg numbers calculated from parent magma compositions for worldwide kimberlite localities from Kjarsgaard *et al*. (2009). The lower end-member, with an Mg# of 82.6 is from a Greenland sample (Nielsen & Sand, 2008), and the upper end-member, with an Mg# of 89, comes from a Russian kimberlite (Kamenetsky *et al*., 2007). Percentage increments represent the volume of olivine fractionation from Le Roex *et al*. (2003).

5.2 Radiogenic isotope fingerprinting of kimberlite magma sources

Isotopic studies on kimberlite magma origin require fresh, uncontaminated hypabyssal kimberlite sample material. These requirements are fulfilled by the Renard and Wemindji hypabyssal kimberlite samples analysed in this study, which represent fresh material from discrete dykes and sills, as well as from small magmatic bodies within the root zones of kimberlite diatremes.

A common misconception is that reliable radiogenic isotope data for kimberlitic rocks can only be obtained through the analysis of constituent groundmass minerals such as perovskite and apatite (e.g., Yang *et al*., 2009; Malarkey *et al*., 2010). Although this is largely correct for ratio determinations on kimberlitic materials (Paton *et al*., 2007; Donnelly *et al*., 2012; Tappe and Simonetti, 2012; Sun *et al*., 2014), more robust isotope systems such as Sm-Nd and Lu-Hf, measured on suitable samples, usually do not reveal resolvable differences between bulk rock and mineral derived data (e.g., Nowell *et al*., 2004; Kopylova *et al*., 2009; Tappe *et al*., 2011, 2012).

Initial $^{87}Sr/^{86}Sr$ values for the Renard and Wemindji kimberlites are relatively clustered, with significant overlap between the two suites. The horizontal spread of $^{87}Sr/^{86}Sr_i$ values in the Renard (0.70241-0.70437) and Wemindji (0.70361-0.70442) kimberlites in Sr-Nd isotope space is most likely a result of low temperature influx of meteoric fluids into the cooling kimberlite magmatic system, resulting in more radiogenic $^{87}Sr/^{86}Sr$ (Le Roex *et al*., 2003; Paton *et al*., 2006; Tappe *et al*., 2012). There is a similar horizontal spread, more so in the Wemindji kimberlites, for $\delta^{18}O$ compositions (see Section 4.4). A subset of Renard samples of hypabyssal pipe origin exhibit low $^{87}Sr/^{86}Sr$ ratios (0.70241-0.70348), identical to those of Late Neoproterozoic kimberlites from Greenland, confirmed by perovskite analysis (Fig. 8 A, B; Nelson, 1989; Tappe *et al*., 2012).

There is a significant overlap in positive ε_{Ndi} values between both the Renard (+1.2 to +4.6 ε_{Ndi}) and Wemindji (+0.2 to +3.4 ε_{Ndi}) kimberlites. Renard (+1.7 to +6.3 ε_{Hfi}) and Wemindji (+1.1 to +6.5 ε_{Hfi}) kimberlites depict a relatively clustered range of positive ε_{Hfi} values, again with significant overlap. All Renard kimberlite samples fall within the mantle array but slightly below the mantle regression line in Hf-Nd isotopic space (Fig. 8 C, D). Wemindji kimberlite samples fall within the mantle array and below the mantle regression line, except sample WEM-02-10 and WEM-02-09 10/10 (below the line) and sample WEM-02-09-10/10A (above the line; Fig. 8 C, D). Wemindji samples have a larger range of values than the Renard kimberlites, but overall their Sr-Nd-Hf isotope compositions are similar.

Renard samples do, however, show slightly more enriched ε_{Hfi} values at similar ε_{Ndi} values, compared with the Wemindji kimberlite sills (Fig. 8 C, D). In general, these compositions are indicative of kimberlite melt derivation largely from moderately depleted convecting upper mantle sources.

Both the Renard and Wemindji hypabyssal kimberlites fall within the depleted quadrant of global ocean island basalts (OIB) Nd-Hf isotope compositions. They tend to have more radiogenic Nd and Hf isotope compositions than southern African kimberlites (Fig.8 C). Note that members of the Laurentian Kimberlite Province, including the Renard and Wemindji kimberlites studied here, lack the prominent Nd-Hf isotope decoupling that has been reported from "young" Mesozoic-Cenozoic Kaapvaal and Slave craton kimberlites (Nowell *et al*., 2004; Tappe *et al*., 2013).

Importantly, the Nd-Hf isotope compositions of the Renard and Wemindji kimberlites fall in close proximity to the inferred low-degree carbonate-rich melt component (Fig. 8 C) of convecting upper mantle origin that was likely widespread beneath cratonic Laurentia during the Late Neoproterozoic (Tappe *et al*., 2008, 2011, 2014).

If correct, this could imply that Late Neoproterozoic kimberlite magmas beneath the eastern Superior craton were derived from the convecting upper mantle with little to no interaction with old cratonic mantle metasomes. This type of interaction between carbonate-rich sublithospheric melts and MARID-type metasomes has been previously proposed to explain Sr-Nd-Hf isotopic trends toward long-term enriched K-rich components in Late Neoproterozoic kimberlites and related magmas from the North Atlantic craton segment of Laurentia (Tappe *et al*., 2008, 2011).

The Renard and Wemindji magmatic kimberlites have initial Os isotope compositions similar to other hypabyssal kimberlites from worldwide occurrences (e.g., Carlson *et al*., 2007; Rao *et al*., 2013), but again, this database is still very limited ($^{187}Os/^{188}Os_i$ = 0.11078-0.12260 vs. global kimberlite range of 0.05162-1.29511; Fig. 9). The Renard and Wemindji kimberlites have less radiogenic

$^{187}Os/^{188}Os_i$ ratios compared with global OIBs (see Day, 2013), and their Os concentrations are slightly higher than for OIBs, but significantly lower than typically observed for cratonic mantle peridotites from worldwide occurrences (see Pearson and Wittig, 2014). Also, the Renard and Wemindji kimberlites have less radiogenic $^{187}Os/^{188}Os_i$ ratios compared with eclogitic and pyroxenitic materials from cratonic mantle lithosphere (e.g., Aulbach *et al*., 2009). These data suggest that the Late Neoproterozoic kimberlite magmas of the eastern Superior craton formed from similar convecting upper mantle peridotite sources with only limited interaction between the ascending sublithospheric kimberlite melts and refractory cratonic mantle materials (Fig. 9; see also Section 5.2.1 for modeling). Most importantly, however, it can be ruled out that eclogitic to pyroxenitic materials within the cratonic mantle contributed to kimberlite melt generation, as has been suggested for the formation of primitive alkaline magmas (e.g., kamafugites and olivine melilitites) in circumcratonic settings based on their elevated initial $^{187}Os/^{188}Os$ ratios (Janney *et al*., 2002; Carlson *et al*., 2007; Rosenthal *et al*., 2009).

6. Sr-Nd-Hf-Os Isotope Modelling

In general, Nd and Hf isotope compositions are more robust tracers to identify kimberlite magmatic sources. However, it is useful to model in Sr-Nd-Hf-Os isotope space as a holistic approach to the melting mechanisms under investigation.

Two models using new radiogenic isotope data have been developed in order to constrain melt contributions from isotopically enriched components to the kimberlite magmas, which are largely derived from depleted peridotitic convecting upper mantle sources in the presence of CO_2 (see discussion above). Table 7 summarises the input parameters used in the binary mixing calculations.

Table 7: Model parameters for binary mixing modelling

ISOTOPICALLY DEPLETED COMPONENT								
	$^{87}Sr/^{86}Sr$	Sr ppm	εNd	Nd ppm	εHf	Hf ppm	$^{187}Os/^{188}Os$	Os ppm
Model-1	*Proxy for mildly depleted carbonatite*				*Mantle array projection*		*OIB*	
	0.70278	450	3.6	300	7.0	4	0.13370	0.00021
	Tappe et al (2012)		Tappe et al (2012)		Chauvel (2008)		Day (2013)	
Model-2	*Most depleted carbonatite of the Kola Alkaline Province*				*Mantle array projection*		*OIB*	
	0.70302	600	7.1	200	12.6	3	0.13370	0.00021
	Kramm (1993)		Kramm (1993)		Chauvel (2008)		Day (2013)	

ISOTOPICALLY ENRICHED COMPONENT								
	$^{87}Sr/^{86}Sr$	Sr ppm	εNd	Nd ppm	εHf	Hf ppm	$^{187}Os/^{188}Os$	Os ppm
Model-1	*West Greenland lamproite #5611(time integrated to 650 Ma)*				*Mantle array projection*		*Ugandan Kamafugite #C6098*	
	0.70763	2500	-34.5	1000	-53.5	15	0.16158	0.001454
	Nelson (1989)		Nelson (1989)		Chauvel (2008)		Rosenthal et al (2009)	
Model-2	*Central Labrador lamproite #L68 (time integrated to 650 Ma)*				*Mantle array projection*		*Ugandan Kamafugite #C6098*	
	0.70669	2300	-15.1	1550	-22.7	35	0.16158	0.001454
	Tappe (2007)		Tappe (2007)		Chauvel (2008)		Rosenthal et al (2009)	

Each model (Fig. 13) consists of an isotopically depleted carbonatite proxy for Sr-Nd isotopes based on the fact that the most CO_2-rich kimberlite and UML magmas of the Laurentian Kimberlite Province tend to have the most depleted isotope compositions (Tappe *et al*., 2008, 2011). In contrast, the isotopically enriched component for Sr-Nd isotope modelling is represented by olivine lamproites from the North Atlantic craton segment of Laurentia (Tappe *et al*., 2007). Olivine lamproites have been shown to be derived from long-term enriched components within refractory cratonic mantle lithosphere, which are K-rich metasomatic sources that mineralogically resemble the MARID suite of xenoliths from the Kaapvaal craton in South Africa (Waters, 1987; Foley, 1992; Konzett *et al*., 1997).

The Hf isotope compositions of the end-members in both models were determined by projection of the respective ε_{Nd} values onto the Nd-Hf isotope mantle array of Chauvel *et al*. (2008).

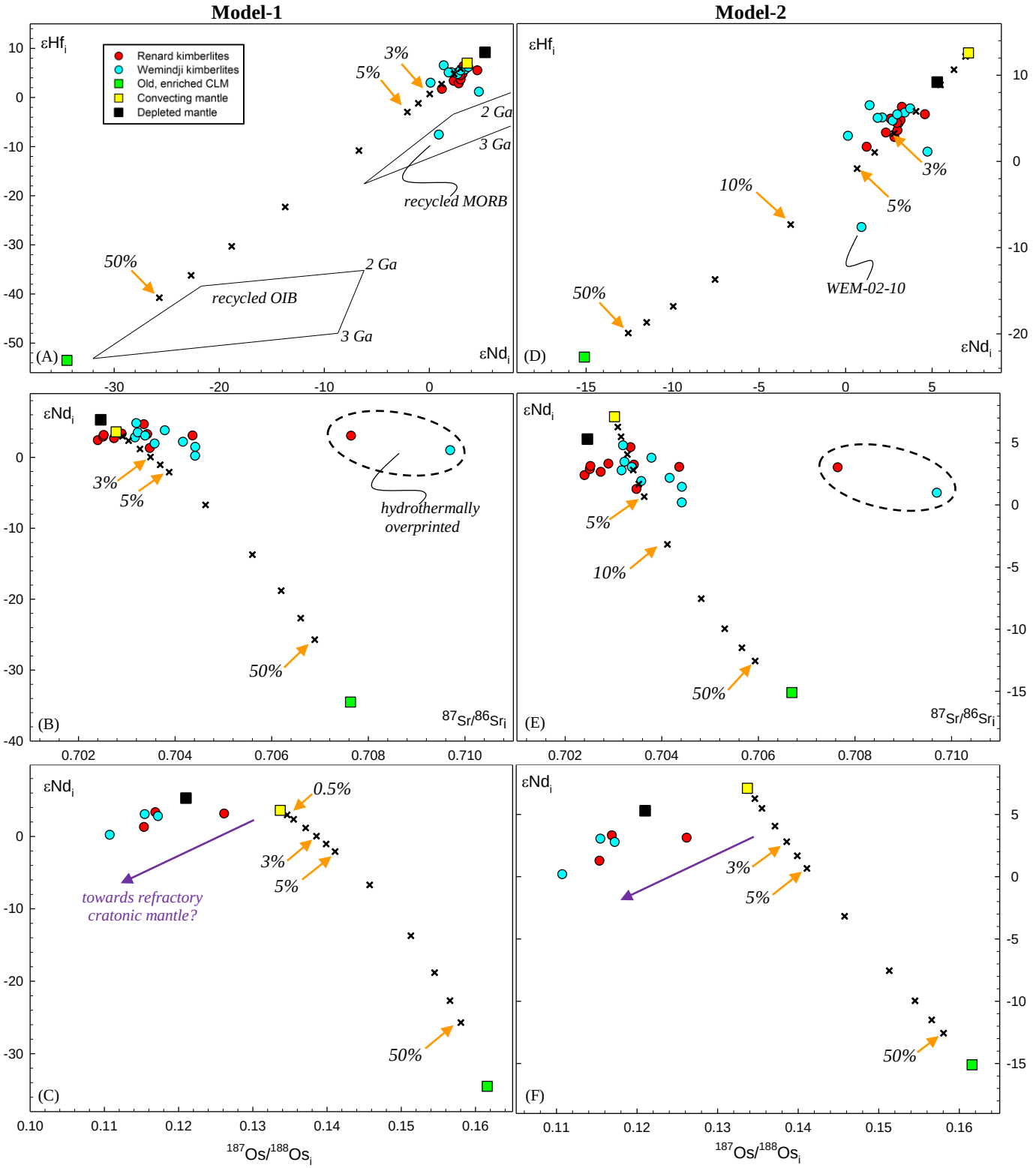

Figure 13: Magma mixing models in Hf-Nd-Sr-Os isotope space for Renard and Wemindji kimberlites. Binary mixing curves have been constructed between an isotopically enriched olivine lamproite and an isotopically depleted carbonatite proxy. A-C) Model-1; D-F) Model-2. See Table 7 for model parameters and text for details on choice of parameters. Also plotted are values for the depleted MORB mantle (time-integrated to 650 Ma) as another possible depleted component (Salters & Stracke, 2004; Workman & Hart, 2005). Fields for recycled OIB and MORB are plotted in A after Tappe *et al*. (2013) and Nowell *et al*. (2003), respectively. Increments labelled represent the fraction of the isotopically enriched component involved in mixing. Model-1 (A-C) suggests that no more than 3% input of an isotopically enriched component represented by a West Greenland lamproite is required to produce kimberlites of the Renard and Wemindji compositions. Model-2 (C-F) suggests that no more than 5% input of an isotopically enriched component represented by a Labrador lamproite is required to produce kimberlites of the Renard and Wemindji compositions. Panels C and F are modelled further in Figure 14, to explain the role of refractory cratonic mantle. Additional panels displaying Model-1 and Model-2 in Hf-Os isotopic space are provided in Appendix C (Fig. C6).

Osmium isotope compositions for the convecting mantle (i.e., moderately depleted) and metasomatic cratonic mantle (i.e., highly enriched) end-members were taken from the compositions of global OIBs (Day, 2013) and type kamafugites from the cratonic western branch of the East African rift (Rosenthal *et al*., 2009), respectively. Unfortunately, no Os isotope data are available for more regional, Laurentian potassic rock suites such as the olivine lamproites from the North Atlantic craton.

Model-1 (Fig. 13 A-C; Appendix C Fig. C6 A) uses as a starting point the Sr-Nd isotope compositions ($^{87}Sr/^{86}Sr$ = 0.70278; Sr =450 ppm; ε_{Nd} = +3.6; Nd =300 ppm) of the most depleted perovskite from a kimberlite dyke in the Sarfartoq region, North Atlantic craton, West Greenland (Tappe *et al*., 2012), with a projected mantle array (Chauvel *et al*., 2008) ε_{Hf} value of +7.0 and Hf concentration equal to 4 ppm. The $^{187}Os/^{188}Os$ composition and Os concentration for the isotopically depleted component is represented by a global average OIB composition ($^{187}Os/^{188}Os$ = 0.13370, Os =0.00021 ppm) from Day (2013) and references therein, given the similarity of worldwide OIBs and carbonatites in terms of Sr-Nd isotope compositions (Nelson *et al*., 1988).

The Sr-Nd isotope compositions of the enriched component ($^{87}Sr/^{86}Sr$ = 0.70763; Sr = 2500 ppm; εNd = -34.5; Nd =1000 ppm) in Model-1 is represented by a Mesoproterozoic olivine lamproite from West Greenland (Nelson, 1989), time integrated to 650 Ma, with a projected mantle array ε_{Hf} value of -53.5 and Hf concentration equal to 15 ppm. The $^{187}Os/^{188}Os$ composition and Os concentration of the enriched end-member ($^{187}Os/^{188}Os$ = 0.16158; Os = 0.00145 ppm) was taken from Ugandan kamafugite sample C6098 reported in Rosenthal *et al*. (2009).

Model-2 (Fig. 13 D-F; Appendix Fig. C6B) considers as a starting point the Sr-Nd components ($^{87}Sr/^{86}Sr$ = 0.70302; Sr = 600 ppm; εNd = +7.1; Nd = 200 ppm) of the isotopically most depleted carbonatite of the Kola Alkaline Province (Kramm, 1993), with an ε_{Hf} mantle array-projected value of +12.6 and concentration of Hf equal to 3 ppm. The respective $^{187}Os/^{188}Os$ compositions and Os concentrations for the isotopically depleted and enriched end-members are the same as in Model-

1. The isotopically enriched Sr-Nd ($^{87}Sr/^{86}Sr$ = 0.70669; Sr=2300 ppm; εNd = -15.1; Nd = 1550 ppm) components of Model-2 are represented by a Mesoproterozoic olivine lamproite from Labrador on the North Atlantic craton margin (Tappe *et al*., 2007), time integrated to 650 Ma, with an ε_{Hf} mantle array-projected value of -22.7 and Hf concentration of 35 ppm. In both Model-1 and Model-2, the depleted MORB mantle is plotted for comparative purposes, and has been time-integrated to 650 Ma.

In Model-1, the Renard and Wemindji kimberlites plot in close proximity to the isotopically mildly depleted end-member (proxy for the convecting upper mantle) in Sr-Nd-Hf isotope space (Fig. 13 A-B). Disregarding the crustally contaminated sample WEM-02-10 (Fig. 13 A; Section 4.1), this binary mixing model suggests that no more than 5% addition of the isotopically enriched end-member component (proxy for ancient metasomatized cratonic mantle) is required to explain the Sr-Nd-Hf isotope compositions of the Renard and Wemindji magmatic kimberlites. This mixing model, which is based on incompatible element isotope systems, reconciles well with the major element compositions of the Late Neoproterozoic kimberlites from the eastern Superior craton such as the generally low concentrations of K and P (Fig. 5 and 6). Discounting the spread in $^{87}Sr/^{86}Sr$ ratios (Fig. 13 B), which is believed to be largely due to hydrothermal overprinting (see Section 5.1), maximum input of the isotopically enriched "cratonic metasome" component to the convecting mantle-derived kimberlite magmas may be as little as 3%.

In the instance of the depleted MORB mantle (as opposed to the moderately depleted convecting upper mantle that contains recycled crustal components), acting as the isotopically depleted component, mixing of between 5% and 10% (not shown) of the enriched cratonic source component would have been required to produce the Sr-Nd-Hf isotope compositions of the Renard and Wemindji magmatic kimberlites.

The isolation of oceanic crust material of MORB composition over billions of years subsequent to subduction into deep Earth reservoirs has been suggested to result in Nd-Hf isotope compositions falling below the mantle array (Blichert-Toft

and Albarede, 1997; Salters and White, 1998). Various authors suggested that this isolation can be achieved by slab material undergoing subduction into the transition zone or lower mantle (Blichert-Toft and Albarede, 1997; Salters and White, 1998). A field for recycled and aged mid-ocean ridge basalt (MORB) is plotted in Figure 13 A to demonstrate the ε_{Hf}-ε_{Nd} evolution of such material after its isolation for billion-year timescales.

Values selected for the recycled MORB field after 2-3 Gyr of isotope evolution can be found in Stracke *et al*. (2003) which are used to describe and calculate the Lu/Hf and Sm/Nd partitioning behaviour in the formation of oceanic crust during melting of the depleted upper mantle in the garnet stability field. Clearly, long-term isolation in excess of 1 Gyr leads to unradiogenic Hf at a given Nd isotopic compositions. Nowell *et al*. (2004) observed such a pronounced Nd-Hf isotope decoupling in Mesozoic southern African kimberlites and their megacrysts, and these authors suggested that subducted MORB crust could represent an important source component to global Group-1 kimberlite magmatism, a model that had been advocated by Ringwood *et al*. (1992) on petrologic grounds.

Tappe *et al*. (2013) introduced a conceptual change to the recycled oceanic crust model as an important kimberlite magma source component in the deeper upper mantle to lower mantle. These authors noted that small degrees of partial melting of recycled oceanic crust preferentially melt OIB-type domains (e.g., seamount relicts) of MORB-dominated oceanic crust. The field for such recycled and stored OIB-type domains is also plotted in Figure 13 A after Tappe *et al*. (2013), following the same method by which the recycled and aged MORB field had been defined in previous studies (Stracke *et al*., 2003; Nowell *et al*., 2004). One of the main implications is that recycled and stored OIB-type domains are isotopically more enriched compared with their MORB counterparts, and they tend to develop even stronger Nd-Hf isotope decoupling. As a consequence, only small amounts of this component are required to explain the systematic shift of global kimberlite compositions below the Nd-Hf isotope mantle array (Tappe *et al*., 2013). Importantly, this isotopic constraint is much easier to reconcile with major element evidence and phase equilibria that suggest that the predominant

kimberlite magma source material is carbonated peridotite (Dalton and Presnall, 1998; Le Roex *et al*., 2003; Brey *et al*., 2008), and not transformed oceanic crust in the form of eclogite, pyroxenite, or garnetite (Ringwood *et al*., 1992).

Regarding the Late Neoproterozoic eastern Superior craton kimberlites studied here, it is interesting to note that all Renard samples fall slightly below the Nd-Hf isotope mantle regression line, but are still placed within the mantle array (Fig. 8 C, D). This subtle Nd-Hf isotope decoupling may suggest a minute contribution of ancient OIB-type recycled oceanic crust (<5%; cf. Tappe *et al*., 2013) to the Renard kimberlite magmas, which were predominately sourced from CO_2-fluxed convecting upper mantle peridotite (see above). Although there is significant overlap in the Nd-Hf isotope systematics between the Renard and Wemindji magmatic kimberlites, the latter show more scatter, which may be a function of a more carbonate-rich convecting upper mantle source region beneath Wemindji at 629 Ma, or due to the fact that the Wemindji kimberlite sills contain larger amounts of ilmenite (see Section 2.1.2 and Table 1). In any case, Wemindji sample WEM-02-10 has been demonstrated to have interacted with continental crust material (see Section 5), and its Nd-Hf isotope composition falls within the field of ancient recycled MORB-type oceanic crust (Fig. 13 A). As pointed out by Tappe *et al*. (2011), the effects of ancient continental and oceanic crustal components on the Nd-Hf isotope systematics of convecting mantle-derived kimberlite magmas are similar, and distinguishing between these options requires large, combined elemental and isotopic datasets (cf., Gaffney *et al*., 2007; Paton *et al*., 2009; Tappe *et al*., 2011, 2013, 2014).

Due to the proximity of the ancient recycled OIB-type oceanic crust field to the isotopically enriched ‘cratonic’ end-member component in Model-1 and Model-2, it would be possible for ancient recycled OIB to have contributed to the Renard and Wemindji kimberlites magmas. However, as demonstrated in Model-2, a contribution of ancient recycled OIB to the system is unnecessary due to the highly similar values produced by a lesser enriched component as shown in Model-1.

The isotopically depleted end-member in Model-2 (Fig. 13 D-E) is significantly

more depleted than the Renard and Wemindji kimberlites. When mixed with a metasomatic cratonic mantle component that is isotopically less enriched than in Model-1, the result is very similar to that of Model-1. Model-2 suggests that a maximum input value of 10% of the isotopically enriched cratonic mantle component is required to explain the isotopic compositions of the Renard and Wemindji magmatic kimberlites. Once again, the offset by the spread of data in $^{87}Sr/^{86}Sr$ vs εNd space reduces the required input from an enriched cratonic mantle source to a maximum of 5%. Using depleted MORB mantle (calculated at 650 Ma) as the isotopically depleted component, Model-2 would only require <1% input from the isotopically enriched cratonic mantle component based on the kimberlite Nd-Hf isotope systematics.

An apparent problem with Model-1 and Model-2 is the lack of reconciliation with the $^{187}Os/^{188}Os_i$ ratios with initial ε_{Nd} and ε_{Hf} (Fig. 13 C, F; Appendix C Fig. C6 A, B). In other words, the Renard and Wemindji kimberlites do not fall on or along binary mixing curves between depleted (convecting upper mantle and depleted MORB mantle) and long-term enriched cratonic mantle (i.e., ancient metasome) components. However, an apparent mixing relationship between the previously used depleted end-members (inferred to be variously depleted asthenospheric components) and a previously unrecognized ancient component with highly unradiogenic Os (<0.11 $^{187}Os/^{188}Os$) and moderately unradiogenic Nd and Hf (0 to -10 ε_{Nd} and ε_{Hf}) isotope compositions (note the positive correlation between initial ε_{Nd} and $^{187}Os/^{188}Os_i$ in Figure 13 C, F as well as initial ε_{Hf} and $^{187}Os/^{188}Os_i$ in Appendix C Fig. C6 A, B), has been identified. This end-member is most likely ancient and refractory cratonic mantle material (cf., Pearson and Wittig, 2014), and it was not detected in Sr-Nd-Hf isotope space due to the very low concentrations of these incompatible elements relative to the more fertile mantle end-member components. In other words, the third source component (i.e., ancient refractory cratonic mantle) influences the kimberlite magma Os isotope compositions by a disproportionately large amount without a significant effect on the Sr-Nd-Hf isotope compositions.

In terms of Os elemental concentrations and isotope compositions, a binary

mixing model between an average OIB ($^{187}Os/^{188}Os_i$ = 0.1331; Os = 0.2123 ppb, Day, 2013), as a proxy for mildly depleted convecting upper mantle material, and a refractory peridotite xenolith from the North Atlantic craton segment of the Laurentian Kimberlite Province, time integrated to 650 Ma ($^{187}Os/^{188}Os_i$ = 0.1088; Os = 1 ppb, Wittig *et al.*, 2010) is shown in Figure 14.

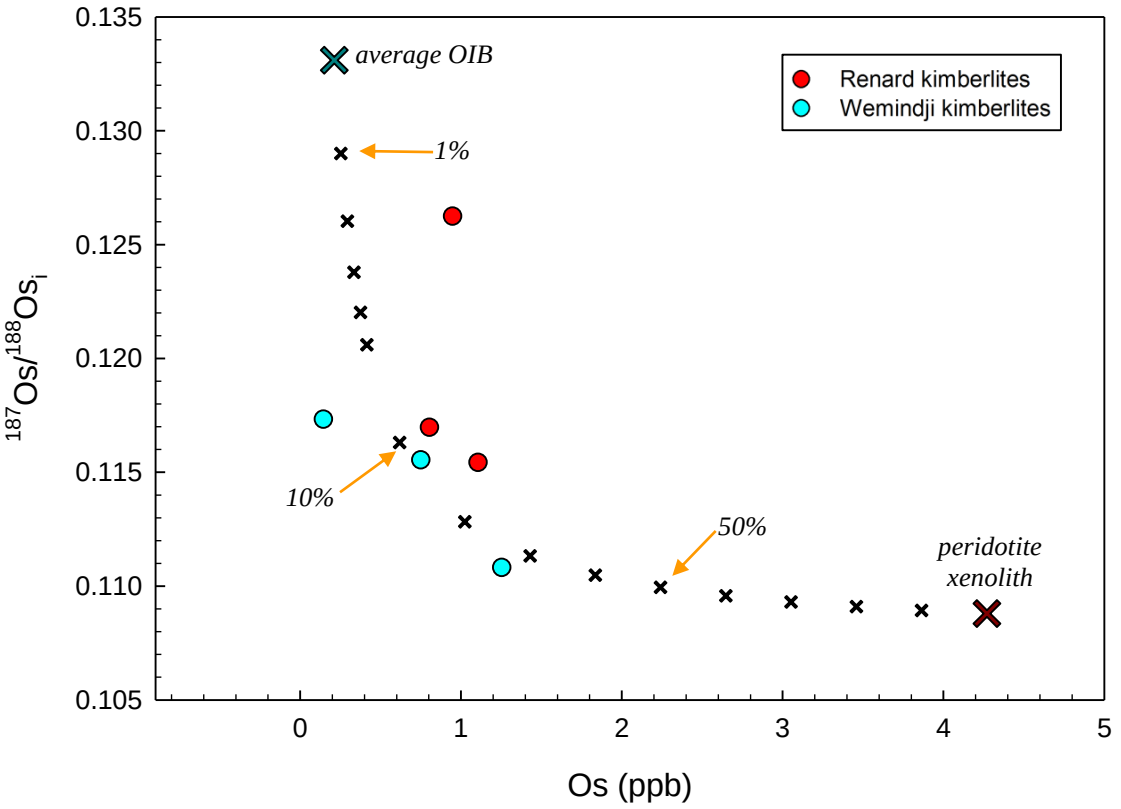

Figure. 14: Binary modelling using Os isotope and elemental compositions for an average ocean island basalt component (Day, 2013) and a mantle-derived peridotite xenolith (sample G-06-7C) from the North Atlantic craton (Wittig *et al.*, 2010). The average OIB composition is used as a proxy for mildly depleted convecting upper mantle material in the form of low-degree carbonatite melt, whereas the peridotite xenolith is used as a proxy for ancient refractory cratonic mantle material. Increments labelled represent the melt fraction from the refractory mantle component. A minimum input value of 2% and a maximum input value of 30% of the ancient refractory cratonic mantle component is required to produce the Renard and Wemindji kimberlite osmium isotope and elemental compositions.

Based on this model, a minimum input value of 2% and a maximum input value of 30% of the refractory cratonic mantle component is required to match the Os concentrations and isotope compositions of the Renard and Wemindji kimberlites.

Whether the refractory cratonic mantle component contributed to the kimberlite magmas in the form of melt (e.g., Russell *et al*., 2012; Pilbeam *et al*., 2013), or whether it is merely present as entrained xenoliths and xenocrysts (Patterson *et al*., 2009) remains uncertain, in particular because the carbonate-rich Wemindji sills only contain little cratonic mantle cargo, including diamond. This could possibly mean that the extensive differentiation of the Wemindji kimberlite sheets allowed for the loss of this cratonic material, and that only minor traces of it is present in the Os isotopic signature due to modal metasomatism of the ancient refractory cratonic material on ascent of the melt.

In summary, binary mixing Model-1 (Fig. 13 A-C; Appendix Fig. C6 A) suggests that <1% and no more than 3% addition of the isotopically enriched end-member component added to the isotopically depleted carbonatite is required to explain the Sr-Nd-Hf isotope compositions of the Renard and Wemindji hypabyssal kimberlites. Alternatively, if the isotopically depleted end-member is represented by a MORB-like melt, between 5 and 10 % addition of the isotopically enriched end-member would be required to explain these compositions. Model-2 (Fig. 13 D-F; Appendix Fig. C6 B) suggests that as little as 3% and no more than 5% addition of the isotopically enriched end-member component is required to explain the Sr-Nd-Hf isotope compositions of the Renard and Wemindji magmatic kimberlites. Alternatively, if the isotopically depleted end-member is represented by a MORB-like melt, less than 1 % addition of the isotopically enriched end-member would be required to explain these compositions. .Both Model-1 and Model-2 reflect the minor volume addition of ancient metasomatized cratonic mantle to a melt of the convecting upper mantle required to result in the Sr-Nd-Hf isotopic compositions found in the Renard and Wemindji kimberlites. Although both Model-1 and Model-2 are plausible models to explain the radiogenic isotopic compositions in the Renard and Wemindji kimberlites, Model-1 is favoured because it requires the less extreme end member components to be plausible. In other words, it is not necessary to have extremely enriched and depleted end member components to explain the isotopic compositions of these kimberlites. Further modelling in Os isotopic space (Fig. 14) suggests that a minimum input of 2% and a maximum input of 30% of a third component represented by refractory

cratonic mantle. This is a relatively wide range of possible input required to acquire such Os isotopic compositions, which could be representative of the residence time of the "kimberlite melt" in the refractory cratonic mantle (e.g. Konzette *et al*., 1998). Further Os isotopic sample analysis from both the Renard and Wemindji kimberlite suites, as well as from depleted and enriched mantle sources, would be useful to better test this hypothesis.

7. Further Discussion

7.1 Constraints on kimberlite petrogenesis from C and O isotope compositions

The $\delta^{13}C$ values of both the Renard (-8.64 to -4.20 ‰) and Wemindji (-4.63 to -3.88‰) kimberlites represent mantle values (-5‰). The hypabyssal features of the Renard and Wemindji kimberlites, including their macrocrystic character and primary carbonate constituents, indicate that carbon present in these samples in the form of carbonates is of mantle origin (Deines & Gold, 1973; Armstrong *et al*., 2004; Giuliani *et al*., 2014).

The $\delta^{13}C$ values of both Renard and Wemindji kimberlites fall in the vicinity of aillikites and kimberlites from the Laurentian Kimberlite Province including West Greenland examples (Fig. 10; Tappe *et al*., 2006, 2008, 2011). Besides one Renard outlier (RD-11646), the majority of samples fall in the range of -6 to -4 ‰ $\delta^{13}C$. The Renard outlier may have undergone incorporation of organic carbon material (Demeny *et al*., 1998; Deines, 2002), but the cause of this incorporation remains unclear. This sample contains the lowest CO_2 concentration (2.64 wt. %) out of the entire dataset, which suggests that complications during CO_2 extraction from the sample powder may have occurred. Although the SiO_2 and Al_2O_3 contents are elevated, RD-11646 has a contamination index of 0.98 (Table 2), which appears to exclude contamination by continental crustal materials.

The Renard and Wemindji kimberlites contain groundmass carbonates with elevated $\delta^{18}O$ values between 10 and 20 ‰. There is a subtle positive correlation

between $\delta^{13}C$ and $\delta^{18}O$ in the Wemindji kimberlites dataset, whereas the Renard dataset is divided into two clusters (Fig.10). The majority of mantle rocks fall mainly between 5.5 and 5.9 ‰ (Bindeman, 2008), therefore the Renard and Wemindji kimberlites clearly fall outside the range for mantle $\delta^{18}O$ compositions. For carbonates, the $^{18}O/^{16}O$ isotope ratios are more susceptible to low-temperature alteration than carbon isotope compositions (Bindeman, 2008). It has already been established that ε_{Hfi} and ε_{Ndi} values can be assumed to be of mantle origin, therefore the lack of correlation between $\delta^{18}O$ and ε_{Hfi} and ε_{Ndi} values (Appendix C Fig. C4) further reiterates that the $\delta^{18}O$ values of the Renard and Wemindji kimberlites do not represent mantle values.

A multitude of factors affect the stable isotopic composition of kimberlites, lamprophyres, and carbonatites, which have been described by Deines (1989), Demeny *et al*. (1998) and Giuliani *et al*. (2014), and references therein. These include crustal assimilation, interaction with low- and high-temperature meteoric fluids, and hydrothermal alteration. The large fractionation factors between carbonates and water at low temperatures can result in increasingly positive $\delta^{18}O$ values (Friedman and O'Neil, 1977; Chacko *et al*., 2001; Hoefs, 2005; Bindeman, 2008). There is a positive correlation between $\delta^{18}O$ and $^{87}Sr/^{86}Sr_i$ in the Renard and Wemindji kimberlites datasets (Appendix C Fig. C5). Such a correlation has been suggested by Taylor (1968, 1980) to indicate crustal assimilation. Based on the major and trace element data presented in this study, as well as Hf and Nd isotopic data (Figs. 4, 5 and 8), significant crustal assimilation can be excluded.

Oxygen isotopic compositions that plot outside of the mantle carbonate box in Figure 10 are indicative of either syn- or post-magmatic processes (Demeny *et al*., 1998). The data compilation in Figure 10 shows that global magmatic kimberlites are generally affected by magmatic fluid-related processes such as late-stage low-temperature hydrothermal activity. This is in good agreement with the above mentioned positive correlation between $\delta^{18}O$ and $^{87}Sr/^{86}Sr$, which also holds on a global scale. There is a 0.8 ‰ deviation for carbon isotopes from the average mantle carbonate value of -5 ‰ $\delta^{13}C$ in the Renard kimberlites (excluding sample RD-11646), whereas samples from Wemindji show a deviation of up to 1.1 ‰

$\delta^{13}C$. Post-emplacement alteration, including interaction with meteoric, deuteric and hydrothermal fluids as well as volatile degassing (Demeny and Harangy, 1996), can result in significant shifts in final carbon isotope compositions. $\delta^{13}C$ values of less than -5 ‰ are interpreted as having undergone Rayleigh fractionation by mantle fluids (Cartigny *et al*., 1998; Giuliani *et al*., 2014).

Rayleigh fractionation modelling was performed to determine the reason behind the larger deviation from the average mantle value in the Wemindji kimberlite carbon isotope dataset. In order to calculate this fractionation, a fractionation factor of 1.0143 was determined for 1200°C using equation [4] of Deines (2004), which is a thermochemically constrained process based on cations present in the samples:

$$1000 \ln \alpha_{\text{Melt-CO2}} = 5.14 \times \frac{\text{Mg + Fe + Mn + Ca + K}}{\text{Si + Al}} + 0.86$$

where $\alpha_{\text{Melt-CO2}}$ is the fractionation factor between the melt and CO_2. Assuming the mantle $\delta^{13}C$ value of -5 ‰ as starting composition, the Wemindji kimberlite magma would have undergone 2-3% fractionation of CO_2 in order to produce the slightly lower $\delta^{13}C$ values, whereas the Renard kimberlites magma would have undergone >2% fractionation. Experimentally constrained Rayleigh fractionation modelling following Chacko *et al*. (1991) yields similar results. This implies that the flow differentiation textures in the Wemindji kimberlites sills do not necessarily reflect significant amounts of CO_2-degassing, or fractionation in general, related to magma flow and filter-pressing processes upon emplacement at crustal levels.

The flow differentiation textures can therefore be attributed to a lower viscosity magma coming into contact with the Kapuskasing Structural Zone, allowing for rapid horizontal magma flow (Zurevinski and Mitchell, 2011). Importantly, the lack of significant magma fractionation, as suggested by the carbon isotope data (Fig. 10) and the Mg-number versus Ni content modelling (Fig. 12), points toward the presence of a very carbonate-rich parental magma to the Wemindji kimberlite sill complex. In other words, Late Neoproterozoic kimberlite melt generation may

have occurred under stronger CO_2-fluxing of convecting upper mantle peridotites beneath the Wemindji cluster compared to the Renard cluster of the eastern Superior craton, which suggests that the Kapuskasing Structural Zone may represent a reactivated tectonic zone translithospheric rift-like feature connected to the Midcontinent Rift System through the Superior craton (cf., Woolley and Bailey, 2012; Lee *et al*., 2016).

Gudfinnsson and Presnall (2005) have described the genetic links between carbonatite and kimberlite magmatism, which are in accordance with discovered geographical as well as temporal proximities of kimberlites and carbonatites in West Greenland (Larson *et al*., 1983; Secher *et al*., 2009; Tappe *et al*., 2009, 2011a, 2012). This suggests that kimberlite and carbonatite magmatism are effectively generated in similar ways, with different degrees of meting and mixing of magmatic sources.

7.2 Mantle source regions of Late Neoproterozoic eastern Superior craton kimberlite magmatism

Kimberlite and related alkaline magmatism has been seen globally to be associated with the onset of major tectonic events of the Wilson cycle (Heaman *et al*., 2004, Tappe *et al*., 2014). Late Neoproterozoic kimberlite and related magmatism accompanied the break-up of the Rodinia supercontinent, and these deeply sourced magmatic events were widespread across Laurentia and Baltica between 680 and 540 Ma (Doig, 1970; Larsen and Rex, 1992; Tappe *et al*., 2004, 2014; O'Brien *et al*., 2005). Whereas many occurrences of the Laurentian Kimberlite Province (kimberlites, UMLs, carbonatites) are situated in the vicinity of the breakout margins from Rodinia (e.g., the Greenland-Labrador Diamond Province, Amon kimberlite sills in northern Baffin Island, Coronation Gulf kimberlites and UMLs in the northern Slave Province; Tappe *et al*., 2014, and references therein), the 654 Ma Renard and 630 Ma Wemindji kimberlite clusters occur well within the interior of former Laurentia; i.e., within the eastern Superior craton (Fig. 1).

One of the most perplexing aspects of the Laurentian Kimberlite Province origin is whether the magmatism was related to active mantle plume upwelling beneath the rifting supercontinent (Puffer, 2002; Ernst and Bleeker, 2010), or whether passive decompression melting of the convecting upper mantle beneath incipient continental rift zones (Larsen and Rex, 1992; Birkett *et al*., 2004; Tappe *et al*., 2004, 2006, 2014) gave rise to kimberlite and related magmas in areas of thick cratonic lithosphere. Alternatively, hotspot track models have also been suggested to explain the Late Neoproterozoic kimberlite and related magmatism on the North Atlantic craton (Greenland and Labrador) and the Superior craton (Quebec), and a possible link to the Madeira hotspot was discussed (Morgan *et al*., 1983; Heaman *et al*., 2004). Some authors argue that mantle hotspots have remained stationary since at least the Early Paleozoic (Torsvik *et al*., 2014), and it appears plausible to link the emplacement of the Renard and Wemindji kimberlite clusters to passage of Rodinia/Laurentia over the Madeira hotspot.

With regard to active mantle plume upwelling, plume generation zones at the core-mantle boundary that lie along the margins of large-low-shear-wave-velocity provinces (LLSVPs) have been suggested to not only be the source to Large Igneous Provinces (e.g., continental flood basalts), but also to low-volume, volatile-rich mantle-derived magmatism such as kimberlites and carbonatites (Torsvik *et al*., 2010). Based on the paleogeography reconstructions created for kimberlites up to 542 Ma back in time, it is possible that a large majority of known Early Paleozoic kimberlites formed within plume generation zones along the Pacific LLSVP (Torsvik *et al*., 2010). However, without firm evidence of the existence of earlier LLSVPs and their correlation with Laurentian kimberlites during the Late Neoproterozoic, it cannot be concluded that active mantle plume impingement beneath Laurentia was responsible for Renard and Wemindji kimberlite magmatism.

Another model to explain the onset of Late Neoproterozoic magmatism of the Laurentian Kimberlite Province is the separation of Laurentia from the supercontinent Rodinia via stepwise rifting along its margins such as the opening of the Iapetus ocean between Laurentia and Baltica at ca. 615 Ma (Kamo *et al*.,

1989), which was associated with the emplacement of giant mafic dyke swarms, which have also been linked to mantle plume upwelling (Ernst and Bleeker, 2010). For the cratonic segments of Laurentia with thick lithosphere, Tappe *et al*. (2011) suggested that Late Neoproterozoic kimberlites and related rocks (including carbonatites) can be linked to a common sublithospheric carbonated silicate magma, and the convergence toward a moderately depleted end-member in Sr-Nd-Hf isotope space (Fig. 8) suggests convecting upper mantle peridotite as the ultimate mantle source (Tappe *et al*., 2008, 2011, 2014).

However, interactions of the carbonated silicate melts with cratonic mantle material, in particular long-term enriched K-rich metasomes, can lead to magma type modifications and isotopic diversification, and it was suggested that calcite kimberlites and aillikites (a carbonate-rich UML variety) may be linked by such reactive melt transport in the cratonic mantle lithosphere (Tappe *et al*., 2011). Importantly, the current knowledge of the distribution of kimberlites and related rocks within the Laurentian Kimberlite Province suggests that K-rich aillikites and other UML magmas are confined to the craton margins and ancient suture zones (Tappe *et al*., 2006, 2008, 2011; Nielsen *et al*., 2009), whereas K-poor kimberlites (Group-1 variety) occur toward the interiors of cratons further away from rift zones (Nielsen *et al*., 2009; Tappe *et al*., 2011, 2014).

In general, the Renard and Wemindji kimberlites appear to fit into this continent-scale tectonomagmatic framework. The Sr-Nd-Hf-Os isotope modelling suggests that less than 5% of long-term enriched metasomatic component from the cratonic mantle contributed to the asthenosphere-derived Renard and Wemindji kimberlite magmas (Fig. 13), and it has been determined that between 2 and 30% of refractory cratonic mantle input is required to produce these compositions (Fig. 14). The geochemical findings and stable carbon isotope modelling presented in this study suggest that the Wemindji kimberlite magmas may have been more carbonate-rich at mantle depths compared with their Renard analogues. This may suggest that the Kapuskasing structure is a tectonically reactivated rift-like deep fracture zone that facilitated CO_2-rich melting conditions of moderately depleted convecting upper mantle peridotite. It is noted that the Sr isotope compositions of

the Wemindji kimberlites are slightly more radiogenic compared with the Renard kimberlites, which may suggest slightly different mantle carbonate sources between the coeval occurrences. Regardless of this, the Wemindji kimberlites are extremely K-poor and show little to no evidence for interaction with long-term enriched cratonic mantle metasomes, which suggests that the northern extension of the Kapuskasing structure was only active for a short time period during Rodinia breakup.

7.3 Diminished diamond potential in the Wemindji kimberlites

The occurrence of minimal microdiamonds found in the Wemindji kimberlites (Moorhead *et al*., 2003; Zurevinski and Mitchell, 2011) is evidence of diamond present in the cratonic lithospheric mantle beneath Wemindji at the time of kimberlite emplacement. As previously discussed, the source for the Renard and Wemindji magmatism can be assumed to be identical; thus, the reason for the insignificant volume of diamond present in the Wemindji kimberlites compared to the diamond-rich Renard suite needs to be further explored. Experimentally, diamond has been seen to be resorbed by carbonatitic melt during metasomatism in the cratonic mantle (cf. Fedortdchouk *et al*., 2011; 2014), resulting in complex crystal morphologies. Due to the elevated CO_2 values seen in the Wemindji kimberlite samples (6-25 vol. % CO_2), resorption of potential significant diamond could have occurred before emplacement of the Wemindji kimberlite sheets. These increased levels of CO_2 within the Wemindji kimberlites can be attributed to the Kapuskasing Structural Zone acting as a failed translithospheric rift system, resulting in the development of a more CO_2-rich melt developing beneath Wemindji, because of the proximity of the Wemindji sheeted dykes to the inferred extension of the KSZ.

8. New U-Pb perovskite age constraints for the Renard kimberlite suite

Kimberlite Pipe-2 and Pipe-3 are only a few hundred meters apart, and they are nearest neighbours at the southern tip of the Renard kimberlite cluster. The SIMS- determined high-precision U-Pb perovskite ages suggest that these two pipes formed contemporaneously at ca. 655 Ma, predating the emplacement of Renard Pipe-1, which is located 1 km to the north, by approximately 20 million years (cf., Birkett *et al*., 2004).

Although there is no geological evidence that could support an apparent age difference (e.g., distinct pipe erosion levels, sedimentary xenoliths), the growing database of high-precision geochronology information for kimberlites and related rocks suggests that individual 'monogenetic' volcanic fields may have been active intermittently over 10 to 40 million year timescales (Creaser *et al*., 2004; Tappe *et al*., 2011, 2012; Donnelly *et al*., 2012; Januszczak *et al*., 2013; Sun *et al*., 2014; Heaman *et al*., 2015).

However, the notion that the Lynx kimberlite dyke may postdate the Renard kimberlite pipes by more than 100 million years (cf., McCandless *et al*., 2008) is challenged here. Based on the observed erosion levels and identical present-day radiogenic isotope ratios for hypabyssal kimberlites from the Renard pipes and the nearby dyke systems at Hibou and Lynx (see Section 4.5) it is assumed that these parts of the subvolcanic Renard kimberlite magmatic system formed penecontemporaneously between 655-630 Ma.

If correct, then kimberlite magmatic activity overlapped at Renard (655-630 Ma) and Wemindji (629 ± 29 Ma; Letendre *et al*., 2003) on the eastern Superior craton, approximately 400 km apart. However, the poorly constrained age for the Wemindji kimberlite sills does not allow for a more detailed assessment of the relative timing of magmatic events. Clearly, additional high-precision geochronology data are required to further improve

the understanding of the economically important Laurentian Kimberlite Province (680-540 Ma, Fig. 1, Tappe *et al*., 2014).

9. Tectonomagmatic model for the eastern Superior craton during the Late Neoproterozoic

Based on all aforementioned major and trace element data, as well as Sr-Nd-Hf-Os and C-O isotopic compositions, the following tectonomagmatic model is proposed for the Late Neoproterozoic geological history of the eastern Superior craton (Fig. 15).

Due to the lack of available evidence for plume-related magmatism throughout the Laurentian Kimberlite Province, a tectonomagmatic model following the distal breakaway of Laurentia from Rodinia is preferred. At the time of Renard (and therefore approximately Wemindji) kimberlite emplacement, the eastern Superior cratonic lithospheric mantle had a maximum thickness of 200 km combined with a geotherm of 38 mWm^{-2}, resulting in a diamond stability field from 130-200 km depth (Hunt *et al*., 2012). Production of an isotopically depleted melt occurred during the breakaway of Laurentia from Rodinia (Stage 1, Fig. 15). This melt could have been influenced by the reactivated Kapuskasing Structural Zone, imparting a CO_2-fluxed signature on the melt beneath Wemindji.

The melt entering the enriched, MARID-type metasomatised cratonic lithospheric mantle underwent metasomatism with no more than 5% of said metasome (Stage 2, Fig. 15). Contemporaneously, addition of between 2 and 30 % ancient refractory cratonic peridotite occurred, before emplacement of diamondiferous kimberlite pipes and dykes between 655 Ma and 630 Ma, making up the Renard kimberlite suite (Stage 3, Fig. 15). The Wemindji kimberlite sills were emplaced at 629 Ma, carrying inconsequential microdiamonds, with all other potential possibly resorbed by the CO_2-rich kimberlite melt developed due to the possible reactivation Kapuskasing Structural Zone into an extensional tectonic environment, which also resulted in the subhorizontal, sheeted nature of the Wemindji kimberlites (Stage 4, Fig. 15).

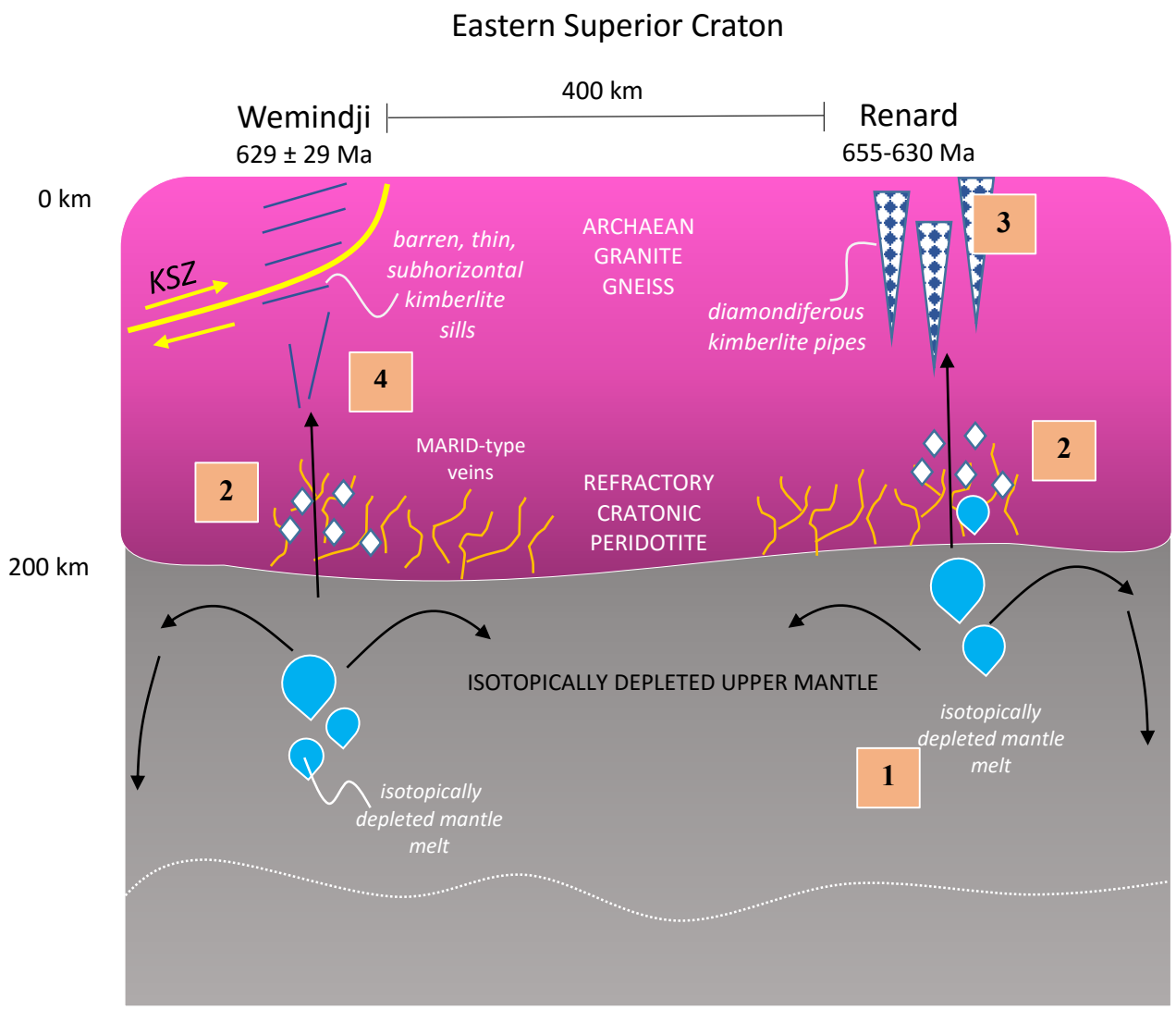

Figure 15: Schematic illustration (not to scale) of Late Neoproterozoic Renard and Wemindji kimberlite magmatism beneath the eastern Superior craton in Quebec, Canada. **1)** The onset of Late Neoproterozoic kimberlite and associated magmatism during the breakaway of Laurentia from Rodinia/mantle plume upwelling leads to the production of an isotopically depleted mantle melt beneath the eastern Superior craton. **2)** This melt enters the isotopically enriched, diamondiferous, MARID-hosting CLM and mixes at a low volume (maximum 5%), **3)** Diamondiferous Renard kimberlites are emplaced into Archean granite gneiss between 655 and 630 Ma. **4)** The reactivated KZS facilitated CO_2-rich melting conditions of moderately depleted convecting upper mantle peridotite beneath Wemindji. This now CO_2-rich, isotopically depleted melt (Stage 1) enters the enriched, diamondiferous CLM below Wemindji and is transported to the surface by fractures formed by the Kapuskasing Structural Zone, resorbing diamond in the metasomatic process and becoming highly differentiated.

10. Conclusion

There is no significant Sr-Nd-Hf-Os isotopic discordance between the Renard and Wemindji kimberlites of the eastern Superior carton, Quebec. Therefore, these kimberlites are deduced to be derived from the same mantle source with similar degrees of partial melting and magma mixing. Modelling suggests that mixing may have occurred between melts derived from isotopically depleted convecting upper mantle peridotite and small volumes of melt derived from old, enriched cratonic lithospheric mantle components.

Binary mixing calculations in the favoured Sr-Nd-Hf model, Model-1, suggest that the maximum input volume from the enriched MARID-type component to a mildly depleted melt of the convecting upper mantle is only 5%. Alternatively, the isotopically depleted end member could be represented by a MORB-type melt, requiring between 5 and 10 % addition of the enriched MARID-type metasome. The significant interaction between carbonate-rich sublithospheric melts and MARID-type metasomes, previously used to explain Sr-Nd-Hf isotopic trends in the Late Neoproterozoic kimberlites and related magmas from the North Atlantic craton segment of Laurentia (Tappe *et al*., 2008, 2011), can therefore not be supported by data from the Renard and Wemindji kimberlites. An additional component of the CLM (i.e., ancient refractory cratonic peridotite) would have had to contribute to the kimberlite magmas beneath the Renard and Wemindji clusters. This refractory component is mainly traced by the kimberlite Os isotope signature (i.e., its Sr-Nd-Hf concentrations are too low), and modelling suggests contributions between 2 and 30% to the convecting mantle derived carbonated silicate ‘proto-kimberlite’ melts. For the Wemindji kimberlite dataset, it remains unclear whether the refractory component is present in the form of xenocrysts, or whether it was incorporated into the carbonate-rich kimberlite melt by digestion-fractional crystallization. It is still unclear whether the onset of Renard and Wemindji kimberlite magmatism is related to the distal breakaway of Laurentia from Rodinia, or if this melt was plume-related, as both isotopically depleted model end members (carbonatite proxy and MORB-type) could result in the isotopic signatures in the Renard and Wemindji kimberlites.

Elevated $\delta^{18}O$ compositions, as well as more radiogenic $^{87}Sr/^{86}Sr_i$ patterns in both the Renard and Wemindji kimberlites can be attributed to low-temperature hydrothermal processes. Modelling of C isotopes in the Renard and Wemindji kimberlites reveal the occurrence of mantle carbon which has undergone >2% Rayleigh fractionation to depict a 0.8 ‰ and 1.1‰ deviation from the mantle $\delta^{13}C$ average value of -5 ‰, respectively. Therefore, the flow differentiation textures present in the Wemindji sills do not necessarily reflect fractionation, but occur rather due to rapid horizontal magma flow as the carbonate-rich parental magma came into contact with the Kapuskasing Structural Zone.

The barren nature of the Wemindji kimberlites, as well as the geochemical and isotopic results for the Wemindji kimberlite sills, suggests that the Kapuskasing Structural Zone may have been a short-lived reactivated rift-like feature, associated with the Midcontinental Rift System of the Superior craton, that promoted CO_2-rich melting conditions beneath Wemindji. If correct, then diamonds may have, subject to speculation, become unstable within the thermally disturbed and CO_2-fluxed mantle root of the eastern Superior craton near the Kapuskasing structure, which is in good agreement with the lack of macro-diamonds in the Wemindji kimberlite sills (Moorhead *et al*., 2003; Zurevinski and Mitchell, 2011). It can therefore be concluded that comprehensive multi-isotopic and geochemical studies on magmatic kimberlites, combined with geological datasets, can provide important insights into the diamond prospectivity of kimberlites and related rocks on a local and continental scale.

References

Agashev, A.M., Pokhilenko, N.P., Takazawa, E., McDonald, J.A., Vavilov, M.A., Watanabe, T. and Sobolev, N.V. (2008). Primary melting sequence of a deep (>250 km) lithospheric mantle as recorded in the geochemistry of kimberlite-carbonatite assemblages, Snap Lake dyke system, Canada. *Chemical Geology* 255, 317-328.

Alibert, C., Michard, A. and Albarede, F. (1983). The transition from alkali basalts to kimberlites: isotope and trace element evidence from melilitites. *Contrib. Mineral. Petrol.* 82, 176-186.

Armstrong, J.P., Wilson, M., Barnett, R.L., Nowicki, T., Kjarsgaard, B.A. (2004). Mineralogy of primary carbonate-bearing hypabyssal kimberlite, Lac de Gras, Slave Province, Northwest Territories, Canada. *Lithos* 76, 415–433.

Aulbach, S., Stachel, T., Creaser, R.A., Heaman, L.M., Shirey, S.B., Muehlenbachs, K., Eichenberg, D. and Harris, J.W. (2009). Sulphide survival and diamond genesis during formation of Archean subcontinental lithosphere. *Lithos,* 112S, 747-757.

Birck, J.L., Roy-Barman, M., Capmas, F. (1997). Re–Os isotopic measurements at the femtomole level in natural samples. *Geostand. Newslett*. 21 (1), 19–27.

Bindeman, I. (2008). Oxygen isotopes in mantle and crustal magmas as revealed by single crystal analysis. *Rev. Mineral. Geochem.* 69, 445–478.

Birkett, T.C., McCandless, T.E., Hood, C.T. (2004). Petrology of the Renard igneous bodies: host rocks for diamond in the northern Otish Mountains region, Quebec. *Lithos* 76, 475-490.

Blichert-Toft, J., Albarede, F. (1997). The Lu–Hf isotope geochemistry of chondrites and the evolution of the mantle-crust system. *Earth Planet.Sci.Lett.*148, 243–258.

Brey, G.P., Bulatov, V.K., Girnis, A.V. and Lahaye, Y. (2008) Experimental melting of carbonated peridotite at 6-10 GPa. *J. Petrol*. 49, 797-821.

Carlson, R.W., Czamanske, G., Fedorenko, V. and Ilupin, I. (2006). A comparison of Siberian meimechites and kimberlites: implications for the source of high-Mg alkalic magmas and flood basalts. *Geochem. Geophys. Geosyst.* 7, Q11014.

Carlson, R.W., Araujo, A.L.N., Junqueira-Brod, T.C., Gaspar, J.C., Brod, J.A., Petrinovic, I.A., Hollanda, M.H.B.M., Pimentel, M.M. and Sichel, S. (2007). Chemical and isotopic relationships between peridotite xenoliths and mafic-ultrapotassic rocks from Southern Brazil. *Chemical Geology,* 242, 415-434.

Caro, G., Kopylova, M.G., Creaser, R.A. (2004). The hypabyssal 5034 kimberlite gahcho kue cluster, Southeastern Slave Craton, Northwest Territories, Canada: a granite contaminated Group I kimberlite. *Can. Min.* 42, 183–207.

Cartigny, P., Harris, J.W., Javoy, M. (1998). Eclogitic diamond formation at Jwaneng: no room for a recycled component. Science 280, 1421–1424.

Chacko, T., Mayeda, T.K., Clayton, R. N., Goldsmith, J.R. (1991). Oxygen and carbon isotope fractionations between CO_2 and calcite. *Geochimica et Cosmochimica Acta* 55 (10), 2867-2882.

Chacko T, Cole DR, Horita J (2001). Equilibrium oxygen, hydrogen and carbon isotope fractionation factors applicable to geologic systems. *Rev Mineral Geochem* 43:1-81.

Chauvel, C., Lewin, E., Carpentier, M., Arndt, N.T. and Marini, J.C. (2008). Role of oceanic basalt and sediment in generating the Hf-Nd mantle array. *Nature Geoscience Letters*, 1, 64-67.

Chu, Z., Yan, Y., Chen, Z., Guo, J., Yang, Y., Li, C., Zhang, Y. (2014). A Comprehensive Methods for Precise Determination of Re, Os, Ir, Ru, Pt, Pd concentrations and Os Isotopic Compositions in Geological Samples. *Geostandards and Geoanalytical Research,* 1-19.

Clarke L. B., Le Bas M. J. and Spiro B. (1994) Rare earth, trace element and stable isotope fractionation of carbonatites at Kruidfontein, Transvaal, South Africa. In: *Kimberlites, Related Rocks and Mantle Xenoliths* (eds. H. O. A. Meyer and O. H. Leonardos). Companhia de Pesquisa de Recursos Minerais, Rio de Janeiro, Brazil, pp. 236–251.

Class, C. and Goldstein, S.L. (1997) Plume-lithosphere interactions in the ocean basins: Constraints from the source mineralogy. *EPSL* 150, 245-260.

Clement, C. R. (1982). A comparative geological study of some major kimberlite pipes in the Northern Cape and Orange Free State. PhD thesis, University of Cape Town, 728 p.

Cohen, A.S. and Waters, F.G. (1996). Separation of osmium from geological materials by solvent extraction for analysis by thermal ionisation mass spectrometry. *Analytica Chimica Acta,* 332, 269-275.

Collerson, K. D., Williams, Q., Ewart, A.E., Murphy, D.T. (2010). Origin of HIMU and EM-1 domains sampled by ocean island basalts, kimberlites and carbonatites: The role of CO_2- fluxed lower mantle melting in thermochemical upwellings. *Phys of the Earth and Plan Int,* 181, 112-131.

Corrigan, D., Pehrsson, S., Wodicka, N. and de Kemp, E. (2009). The Palaeoproterozoic Trans Hudson Orogen: a prototype of modern accretionary processes. In: Murphy, J. B., Keppie, J. D. and Hynes, A. J. (eds) A*ncient Orogens and Modern Analogues*. Geological Society, London, Special Publications 327, 457-479.

Creaser, R. A., Grütter, H., Carlson, J., & Crawford, B. (2004). Macrocrystal

phlogopite Rb–Sr dates for the Ekati property kimberlites, Slave Province, Canada: evidence for multiple intrusive episodes in the Paleocene and Eocene. *Lithos*, *76*(1), 399-414.

Crough, S.T., Morgan, W.J., Hargraves, R.B. (1980). Kimberlites: Their relation to mantle hotspots. *Earth and Planetary Science Letters,* 50, 260-274.

Dahlgren, S. (1994). Late Proterozoic and Carboniferous ultramafic magmatism of carbonatitic affinity in Southern Norway. Lithos 31, 141-154.

Dalton, J.A. and Presnall, D.C. (1998). The continuum of primary carbonatitic-kimberlitic melt compositions in equilibrium with lherzolite: data from the system CaO-MgO-Al_2O_3-SiO_2-CO_2 at 6 GPa. *J. Petrol*. 39, 1953-1964.

Dawson, J.B., Smith, J.W. (1977). The MARID (mica-amphibole-rutile-ilmenite-diopside) suite of xenoliths in kimberlite. *Geo et Cos. Act* 41, 309- 323.

Day, J.M.D. (2013). Hotspot volcanism and highly siderophile elements. *Chemical Geology*, 341, 50-74.

Debaille, V., Trønnes, R.G., Brandon, A.D., Waight, T.E., Graham, D.W., Lee, C.-T.A. (2009). Primitive off-rift basalts from Iceland and Jan Mayen: Os-isotopic evidence for a mantle source containing enriched subcontinental lithosphere. *Geochimica et Cosmochimica Acta* 73, 3423–3449.

Demeny, A., Harangi, S. (1996). Stable isotope studies and processes of carbonate formation in Hungarian alkali basalts and lamprophyres: evolution of magmatic fluids and magma–sediment interactions. *Lithos* 37, 335–349.

Demeny, A., Ahijado, A., Casillas, R. and Vennemann, T.W. (1998). Crustal contamination and fluid/rock interaction in the carbonatites of Fuerteventura (Canary Islands, Spain): a C, O, H isotopic study. *Lithos*, 44, 101-115.

Deines, P. (1989). Stable isotope variations in carbonatites. In: Bell, K. (Ed.), *Carbonatites: Genesis and Evolution.* Unwin Hyman, London, pp. 301–359.

Deines, P., Gold, D.P. (1973). The isotopic composition of carbonatite and kimberlite carbonates and their bearing on the isotopic composition of deep-seated carbon. *Geochimica et Cosmochimica. Acta* 37, 1709–1733.

Deines, P., 2002. The carbon isotope geochemistry of mantle xenoliths. Earth Sci. Rev. 58, 247–278.

Doig, R. (1970). An alkaline rock province linking Europe and North America. *Canadian Journal of Earth Sciences* 7(1), 22-28.

Donnelly, C.L., Griffin, W.L., Yang, J.H., O'Reilly, S.Y., Li, Q.L., Pearson, N.J. and Li, X.H. (2012) In situ U-Pb dating and Sr-Nd isotopic analysis of perovskite: constraints on the age and petrogenesis of the Kuruman kimberlite province, Kaapvaal craton, *S.A. J. Petrol*. 53, 2497 2522.

Ernst, R and Bleeker, W. (2010). Large igneous provinces (LIPs), giant dyke swarms, and mantle plumes: significance for breakup events within Canada and adjacent regions from 2.5 Ga to the Present. *Canadian Journal of Earth Sciences,* 47 (5), 695-739.

Fedortchouk Y, Manghnani MH, Hushur A, Shiryaev A, Nestola F (2011). An atomic force microscopy study of diamond dissolution features: the effect of H_2O and CO_2 in the fluid on diamond morphology. *Am. Mineral.* 96:1768–1775.

Fedortdchouk, Y., Schmidt, M.W., Liebske, C. (2014). Experimental study of diamond resorption during mantle metasomatism, EGU General Assembly, *Geophysical Research Abstracts*, 16.

Fischer-Gödde, M., Becker, H., Wombacher, F. (2010). Rhodium, gold and other

highly siderophile element abundances in chondritic meteorites. *Geochimica et Cosmochimica Acta* 74 (1), 356–379.

Fitzgerald, C.E., Hetman, C.M., Lepine, I., Skelton, D.S. and McCandless, T.E. (2009). The internal geology and emplacement history of the Renard 2 kimberlite, Superior Province, Quebec, Canada. Proceedings of the 9th International Kimberlite Conference. *Lithos* 112S, 513–528.

Friedman I, O'Neil JR (1977). Compilation of stable isotope fractionation factors of geochemical interest (Geological Survey Professional Paper 440-KK. In: *Data of Geoch*. 6th Ed. Fleischer M (ed) Washington, D.C., U.S. Gov. Print Off p. 1-12.

Gaffney, A. M., Blichert-Toft, J., Nelson, B. K., Bizzarro, M., Rosing, M. and Albarede,F. (2007). Constraints on source-forming processes of West Greenland kimberlites inferred from Hf-Nd isotope systematics. *Geochimica et Cosmochimica Acta* 71, 2820-2836.

Giuliani, A., Philips, D., Kamenetsky, V.S., Fiorentini, M.L., Farquhar, J and Kendrick, M.A. (2014). Stable isotope (C, O, S) compositions of volatile-rich minerals in kimberlites: A review. *Chem Geol*, 374-375, 61-83.

Giuliani, A., Phillips, D., Woodhead, J.D., Kamenetsky, V.S., Fiorentini, M.L., Maas, R., Soltys, A. and Armstrong, R.A. (2015). Did diamond-bearing orangeites originate from MARID-veined peridotites in the lithospheric mantle? *Nat. Commun*. 6, 1-10.

Griffin, W.L., O'Reilly, S.Y., Abe, N., Aulbach, S., Davies, R.M., Pearson, N.J., Doyle, B.J and Kivi, K. (2003*b*). The origin and evolution of Archean lithospheric mantle. *Precambrian Research* 127, 19-41.

Griffin, W.L., O'Reilly, S.Y., Doyle, B.J., Pearson, N.J., Coopersmith, H., Kivi, K., Malkovets, V., Pokhilenko, N. (2004). Lithosphere mapping beneath

the North American plate. *Lithos*, 77, 873-922.

Griffin, W.L., Batumike, J.M., Greau, Y., Peasron, N.J., Shee, S.R., O'Reilly, S.Y. (2014). Emplacement ages and sources of kimberlites and related rocks in southern Africa: U-Pb ages and Sr-Nd isotopes of groundmass perovskite. *Contribution to Mineral Petrology*, 168, 1032.

Gudfinnsson, G.H. and Presnall, D.C. (2005). Continuous gradations among primary carbonatitic, kimberlitic, melilititic, basaltic, picritic, and komatiitic melts in equilibrium with garnet lherzolite at 3-8 Gpa. *Journal of Petrology*, 46(8), 1645-1659.

Haggerty, S.E. (1994). Superkimberlites: A geodynamic diamond window to the Earth's core. *Earth and Planetary Science Letters*, 122, 57-69.

Heaman, L.M. (1989). The nature of the subcontinental mantle from Sr-Nd-Pb isotopic studies on kimberlitic perovskite. *EPSL* 92, 323-334.

Heaman, L.M. and Kjarsgaard, B.A. (2000). Timing of North American kimberlite magmatism: continental extension of the Great Meteor hotspot track? *Earth and Planetary Science Letters* 178, 253-268.

Heaman, L.M., Kjarsgaard, B.A. and Creaser, R.A. (2004). The temporal evolution of North American kimberlites. *Lithos* 76, 377-379.

Heaman, L.M. (2009). The application of U–Pb geochronology to mafic, ultramafic and alkaline rocks: An evaluation of three mineral standards. *Chemical Geology* 261, 42-51.

Hoefs, J. (2005) *Stable Isotope Geochemistry*, Springer, 5th edition.

Hoffman, P. F. (1988). United Plates of America, the birth of a craton - Early Proterozoic assembly and growth of Laurentia. *Annual Review of Earth and Planetary Sciences* 16, 543-603.

Horan, M.F., Walker, R.J., Morgan, J.W., Grossman, J.N., Rubin, A.E. (2003).

Highly siderophile elements in chondrites. *Chem. Geol.* 196, 5–20.

Hunt, L., Stachel, T., Grütter, H., Armstrong, J., McCandless, T.E., Simonetti, A., Tappe, S. (2012). Small mantle fragments from the Renard kimberlites, Quebec: Powerful recorders of mantle lithosphere formation and modification beneath the eastern Superior craton. *J. Pet* 53, 1597-1635.

InfoMine (2011). Mine Sites: Renard. Available from: http://www.infomine.com/minesite/minesite.asp?site=renard (Accessed 27 March 2014).

Ireland, T.R., Compston, W., Williams, I.S. and Wendt, I. (1990) U-Th-Pb systematics of individual perovskite grains from the Allende and Murchison carbonaceous chondrites. *EPSL* 101, 379-387.

Irvine, G.J., Pearson, D.J., Kjarsgaard, B.A., Carlson, R.W., Kopylova, M.G. and Dreibus, G. (2003). A Re-Os isotope and PGE study of kimberlite-derived peridotite xenoliths from Somerset Island and a comparison to the Slave and Kaapvaal cratons. *Lithos*, 71, 461-488.

Jackson, M.G., Shirey, S.B. (2011). Re-Os isotope systematics in Samoan shield lavas and the use of Os-isotopes in olivine phenocrysts to determine primary magmatic compositions. *EPSL* 312, 91–101.

Janney, P.E., le Roex, A.P., Carlson, R.W. and Viljoen, K.S. (2002). A chemical and multi-isotope study of the Western Cape Olivine Melilitite Province, South Africa: Implications for the sources of kimberlites and the origin of the HIMU signature in Africa. *Journal of Petrology*, 45(12), 2339-2370.

Januszczak, N., Seller, M.H., Kurszlaukis, S., Murphy, C., Delgaty, J., Tappe, S., Ali, K., Zhu, J. and Ellemers, P. (2013). A multidisciplinary approach to the Attawapiskat kimberlite field, Canada: Accelerating the discovery-to-production pipeline, in: Pearson, D.G. (Ed.), Special Issue of the Journal of the Geological Society of India, *Proceedings of the 10th ICK* Springer,

Bangalore, pp. 157-171.

Jelsma, H., Barnett,W., Richards, S., Lister, G. (2009). Tectonic setting of kimberlites. *Lithos* 112, 155–165.

Kamenetsky, V.S., Kamenetsky, M.B., Sharygin, V.V., Faure, K., Golovin, A.V. (2007).Chloride and carbonate immiscible liquids at the closure of the kimberlite magma evolution (Udachnaya-East kimberlite, Siberia). *Chem Geo* 237, 384–400.

Kamo, S.L., Gower, C.F and Krogh, T.E. (1989). Birthdate for the Iapetus ocean? A precise U-Pb zircon and baddeleyite age for the Long Range dikes, southeast Labrador. *Geology*, 17, 602-605.

Kinny, P.D., Griffin, B.J., Heaman, L.M., Brakhfogel, F.F. and Spetsius, Z.V. (1997) SHRIMP U-Pb ages of perovskite from Yakutian kimberlites, in: Sobolev, N.V., Mitchell, R.H. (Eds.), *Proceedings of the Sixth International Kimberlite Conference*. Allerton Press, New York, United States, pp. 97-105.

Kjarsgaard, B.A., Pearson, D.G., Tappe, S., Nowell, G.M., Dowall, D. (2009). Geochemistry of hypabyssal kimberlites from Lac de Gras, Canada: comparisons to a global database and applications to the parent magma problem. *Lithos* 112, 236–248.

Konzett, J. (1998). The timing of MARID metasomatism in the Kaapvaal mantle: An ion probe study of zircons from MARID xenoliths. *Earth and Planetary Science Letters* 160, 133-145.

Kopylova, M. G., Nowell, G. M., Pearson, D. G. and Markovic, G. (2009). Crystallization of megacrysts from protokimberlitic fluids: geochemical evidence from high-Cr megacrysts in the Jericho kimberlite. *Lithos* 112, 284-295.

Kramers, J.D. and Smith, C.B. (1983). A feasibility study of U-Pb and Pb-Pb dating of kimberlites using groundmass mineral fractions and whole-rock samples. *Chemical Geology* 41, 23-38.

Kramm U. (1993) Mantle components of carbonatites from the Kola alkaline province, Russia and Finland: a Nd–Sr study. *European Journal of Mineralogy*. 5, 985–989.

Larsen, L.M., Rex, D.C. (1992). A review of the 2500 Ma span of alkaline-ultramafic, potassic and carbonatitic magmatism in West Greenland. *Lithos* 28, 367–402.

Leclair, A.D., Percival, J.A., Green, A.G. and Wu, J. (1994). Seismic reflection profiles across the central Kapuskasing uplift. *Can. J. of Earth Sci*, 31, 1016-1026.

Lee, H., Muirhead, J.D., Fischer, T.B., Ebinger, C.J., Kattenhorn, S. A., Sharp, Z.D., Kianji, G. (2016). Massive and prolonged deep carbon emissions associated with continental rifting. *Nature Geoscience* 9, 145-149.

le Roex, A.P., Lanyon, R. (1998). Isotope and trace element geochemistry of Cretaceous Damaraland lamprophyres and carbonatites, northwestern Namibia: evidence for plume-lithosphere interactions. *J. Pet.* 39 (6), 1117–1146.

le Roex, A. P., Bell, D. R. and Davis, P. (2003). Petrogenesis of Group I kimberlites from Kimberley, South Africa: evidence from bulk rock geochemistry. *Journal of Petrology* 44, 2261-2286.

Letendre J, L'Heureux ML, Nowicki T and Creaser R (2003). The Wemindji kimberlites: exploration and Geology. In: *8th International Kimberlite Conference*, extended abstract.

Li, Q.L., Li, X.H., Liu, Y., Wu, F.Y., Yang, J.H. and Mitchell, R.H. (2010) Precise U-Pb and Th-Pb age determination of kimberlitic perovskites by secondary ion mass spectrometry. *Chemical Geology* 269, 396-405.

Ludwig, K.R. (2000) Isoplot/Ex version 2.2. - a geochronological toolkit for Microsoft Excel. Berkeley Geochronology Center Special Publication No. 1a, Berkeley, California.

Maier, W.D., Peltonen, P., McDonald, I., Barnes, S.J., Hatton, C. and Viljoen, F. (2012). The concentration of platinum group elements and gold in Southern African and Karelian kimberlite-hosted mantle xenoliths: Implications for noble metal content of the Earth's mantle. *Chemical Geology*, 302-303,119-135.

Malarkey, J., Pearson, D. G., Kjarsgaard, B. A., Davidson, J. P., Nowell, G. M., Ottley, C. J., & Stammer, J. (2010). From source to crust: tracing magmatic evolution in a kimberlite and a melilitite using microsample geochemistry. *Earth and Planetary Science Letters*, *299*(1), 80-90.

McCandless, T.E. (1999). Kimberlites: Mantle expressions of deep-seated subduction, in: Gurney, J.J., Gurney, J.L., Pascoe, M.D., Richardson, S.H. (Eds.), *Proceedings of the VIIth International Kimberlite Conference.* Red Roof Design, Cape Town, pp. 545-549.

McCandless, T., Schulze, D., Bellis, A., Taylor, L.A., Liu, Y., van Rythoven, A.D., (2008). Morphology and chemistry of diamonds from the lynx kimberlite dyke complex, Northern Otish Mountains, Quebec. Extended Abstracts of the 9th IKC, Frankfurt, Germany. August, 2008.

Meert, J.G., Walderhaug, H.J., Torsvik, T.H. and Hendriks, B.W.H. (2007). Age and paleomagnetic signature of the Alno carbonatite complex (NE Sweden): Additional controversy for the Neoproterozoic paleoposition

of Baltica. *Precambrian Research* 154, 159-174.

Meisel, T., Walker, R.J., Irving, A, J. and Lorand, J.P. (2001). Osmium isotopic compositions of mantle xenoliths: A global perspective. *Geochimica et Cosmochimica Acta*, 65(8), 1311-1323.

Mitchell, R.H. (1986). *Kimberlites: Mineralogy, Geochemistry, and Petrology.* Plenum Press, New York. 442 pp.

Moorhead, J., Beaumier, M., Girard, R., Heaman, L.M. (2003). Distribution, structural controls and ages of kimberlite fields in the Superior Province of Quebec. 8th International Kimberlite Conference, extended abstract.

Morgan, W.J. (1983). Hotspot tracks and the early rifting of the Atlantic. *Tectonophysics* 94, 123–139.

Münker, C., Weyer, S., Scherer, E. and Mezger, K. (2001) Separation of high field strength elements (Nb, Ta, Zr, Hf) and Lu from rock samples for MC ICPMS measurements. *Geochemistry, Geophysics, Geosystems* 2, 2001GC000183.

Muntener, C. and Scott-Smith, B.H. (2013). Economic geology of Renard 3, Québec, Canada: A diamondiferous, multi-phase pipe infilled with hypabyssal and tuffisitic kimberlite, in: Pearson, D.G. (Ed.), *Special Issue of the Journal of the Geological Society of India, Proceedings of the 10th International Kimberlite Conference*. Springer, Bangalore, pp. 241-256.

Nelson, D.R. and McCulloch, M.T. (1988). Enriched mantle components and mantle recycling of sediments. 4th Int. Kimberlite Conf., Perth, W.A., 1986. *Geological Society of Australia Special Publication.*

Nielsen, T.F.D., Sand, K.K., 2008. The Majuagaa kimberlite dyke, Maniitsoq, region, West Greenland: constraints on a Mg-rich silicocarbonatitic melt

composition from groundmass mineralogy and bulk compositions. *Canadian Mineralogist* 46, 1043–1061.

Nowell, G.M., Pearson, D.G., Bell, D.R., Carlson, R.W., Smith, C.B., Kempton, P.D., Noble, S.R. (2004). Hf Isotope systematics of kimberlites and their megacrysts: new constraints on their source regions. *J. Pet.* 45, 1583–1612.

O'Brien, H.E. and Tyni, M. (1999). Mineralogy and geochemistry of kimberlites and related rocks from Finland, in: Gurney, J.J., Gurney, J.L., Pascoe, M.D., Richardson, S.H. (Eds.), *Proceedings of the VIIth International Kimberlite Conference*. Red Roof Design, Cape Town, pp. 625-636.

O'Brien, H.E, Peltonen, P., Vartainen, H. (2005). Kimberlites, carbonatites, and alkaline rocks. In: Lehtinen, M., Nurmi, P.A., Ramo, O.T. (Eds.) *Precambrian Geology of Finland – Key to the Evolution of the Fennoscandian Shield*, Elsevier B.V., Amsterdam, 605-644.

Palme, H. and O'Neill, H. S. C. (2003). Cosmochemical estimates of mantle composition. In: Carlson, R. W. (ed.) *T. on Geochem*. Elsevier, pp. 1-38.

Patterson, M., Francis, D., McCandless, T. (2009). Kimberlites: magmas or mixtures? *Lithos* 112, 191-200.

Paton, C., Hergt, J.M., Phillips, D., Woodhead, J.D. and Shee, S.R. (2007) New insights into the genesis of Indian kimberlites from the Dharwar craton via in situ Sr isotope analysis of groundmass perovskite. *Geology* 35, 1011-1014.

Paton, C., Hergt, J.M., Woodhead, J.D., Phillips, D., Shee, S.R. (2009). Identifying the asthenospheric component of kimberlite magmas from the Dharwar Craton, India. *Lithos* 112, 296–310.

Pearson, D. G., Parman, S. W., & Nowell, G. M. (2007). A link between large

mantle melting events and continent growth seen in osmium isotopes. *Nature*, 449 (7159), 202-205.

Pearson, D. G., & Wittig, N. (2014). The formation and evolution of cratonic mantle lithosphere—Evidence from mantle xenoliths. *Treatise on Geochemistry*, *2*, 255-292.

Percival, J.A. and Card, K.D. (1983). Archean crust as revealed in the Kapuskasing uplift, Superior province, Canada. *Geology* 11, 323-326.

Percival, J.A, Sanborn-Barrie M, Skulski T, Stott GM, Helmstaedt H, White DJ (2006) Tectonic evolution of the western Superior Province from NATMAP and Lithoprobe studies. *Can J. of Earth Sci*, 43, 1085–1117.

Percival, J.A., Skulski, T., Sanborn-Barrie, M., Stott, G.M., Leclair, A.D., Corkery, M.T., and Boily, M. (2012). Geology and tectonic evolution of the Superior Province, Canada. Chapter 6 *in:* Tectonic Styles in Canada: The Lithoprobe Perspective. *Edited by* J.A.Percival, F.A. Cook, and R.M. Clowes. Geological Ass. of Canada, Special Paper 49, 321- 378.

Perry, H.K.C., Jaupart, C., Mareschal, J.-C., Rolandone, F., Bienfait, G. (2004). Heat flow in the Nipigon arm of the Keweenawan rift, Northwestern Ontario, Canada. *Geophysical Research Letters*, 31.

Pilbeam, L.H., Nielsen, T.F.D. and Waight, T.E. (2013) Digestion Fractional Crystallization (DFC): An important process in the genesis of kimberlites. Evidence from olivine in the Majuagaa kimberlite, southern West Greenland. *J. Petrol*. 54, 1399-1425.

Puffer, J.H. (2002). A late Neoproterozoic eastern Laurentian superplume: Location, size, chemical composition and environmental impact. *American Journal of Science*, 302, 1-27.

Rao, N.V.C., Creaser, R.A., Lehmann, B. and Panwar, B.K. (2013). Re-Os isotope study of Indian kimberlites and lamproites: Implications for mantle source regions and cratonic evolution. *Chemical Geology* 363, 36-47.

Ringwood, A.E., Kesson, S.E., Hibberson, W.O. and Ware, N. (1992) Origin of kimberlites and related magmas. *EPSL* 113, 521-538.

Roeder, P.L., Schulze, D.J. (2008). Crystallization of groundmass spinel in kimberlite. *Journal of Petrology* 49 (8), 1473–1495.

Russell, J.K., Porritt, L.A., Lavallee, Y. and Dingwell, D.B. (2012) Kimberlite ascent by assimilation-fuelled buoyancy. *Nature* 481, 352-357.

Rogers, N.W. (1992). Potassic magmatism as a key to trace-element enrichment processes in the upper mantle. *J. of Volc and Geotherm Re.* 50, 85- 99.

Rogers, N.W., Hawkesworth, C.J. and Palacz, Z.A. (1992) Phlogopite in the generation of olivine melilitites from Namaqualand, South Africa and implications for element fractionation processes in the upper mantle. *Lithos* 28, 347-365.

Rosenthal, A., Foley, S.F., Pearson, D.G., Nowell, G.M. and Tappe, S. (2009). Petrogenesis of strongly alkaline primitive rocks at the propagating tip of the western branch of the East African Rift. *EPSL,* 284, 236-248.

Salters, V.J.M., White, W.M. (1998). Hf isotope constraints on mantle evolution. *Chem. Geol.* 145, 447–460.

Salters, V.J.M. and Stracke, A. (2004). Composition of the depleted mantle. *Geochemistry Geophysics Geosystems* 5(5), Q05B07.

Sand, K.K., Waight, T.E., Pearson, D.G., Nielsen, T.D>F., Makovivky, E. and

Hutchison, M.T. (2009). The lithospheric mantle below southern West Greenland. A geothermobaromic approach to diamond potential and mantle stratigraphy. *Proceedings of the 9th IKC*, 1155-1166.

Scott-Smith, B.H. (2008). Canadian kimberlites: Geological characteristics relevant to emplacement. *J. of Volc and Geotherm Research*, 174, 9-19.

Secher, K., Heaman, L.M., Nielsen, T.F.D., Jensen, S.M., Schjøth, F., Creaser, R.A. (2009). Timing of kimberlite, carbonatite, and ultramafic lamprophyre emplacement in the alkaline province located 64°–67°N in southern West Greenland. *Lithos* 112, 400–406.

Smith, C. B. (1983). Pb–Sr and Nd isotopic evidence for sources of southern African Cretaceous kimberlites. *Nature* 304, 51–54.

Snyder, D.B. and Lockhart, G.D. (2005). Kimberlite trends in NW Canada. *Journal of the Geological Society*, 162, 737-740.

Snyder, D. B., Berman, R. G., Kendall, J. M. and Sanborn-Barrie, M. (2013). Seismic anisotropy and mantle structure of the Rae craton, central Canada, from joint interpretation of SKS splitting and receiver functions. *Precambrian Research* 232, 189-208.

Stacey, J.S. and Kramers, J.D. (1975) Approximation of terrestrial lead isotope evolution by a two-stage model. *EPSL* 26, 207-221.

Steiger, R.H. and Jäger, E. (1977) Subcommission on geochronology: Convention on the use of decay constants in geo- and cosmochronology. *Earth and Planetary Science Letters* 36, 359-362.

Stein, C. A., Stein, S., Merino, M., Keller, R.G., Flesch, L.M. and Jurdy, D.M (2014). Was the Midcontinent Rift part of a successful seafloor-spreading episode? *Geophys. Res. Lett*., 41.

Stracke, A., Bizimis, M., Salters, V.J.M. (2003). Recycling oceanic crust: quantitative constraints. *Geochem. Geophys. Geosyst*. 4, Q8003.

Sun, J., Liu, C.-Z., Tappe, S., Kostrovitsky, S.I., Wu, F.-Y., Yakovlev, D., Yang, Y.H. and Yang, J.H. (2014). Repeated kimberlite magmatism beneath Yakutia and its relationship to Siberian flood volcanism: Insights from in situ U-Pb and Sr-Nd perovskite isotope analysis. *EPSL* 404, 283-295.

Tachibana, Y., Kaneoka, I., Gaffney, A. and Upton, B. (2006). Ocean-island basalt-like source of kimberlites magmas from West Greenland revealed by high $^{3}He/^{4}He$ ratios. *Geology*, 4, 273-276.

Tappe, S., Jenner, G.A., Foley, S.F., Heaman, L., Besserer, D., Kjarsgaard, B. and Ryan, B. (2004). Torngat ultramafic lamprophyres and their relation to the North Atlantic Alkaline Province. *Lithos* 76, 491-518.

Tappe, S., Foley, S.F., Jenner, G.A., Heaman, L.M., Kjarsgaard, B.A., Romer, R.L., Stracke, A., Joyce, N. and Hoefs, J. (2006) Genesis of ultramafic lamprophyres and carbonatites at Aillik Bay, Labrador: A consequence of incipient lithospheric thinning beneath the North Atlantic craton. *J. Petrol*. 47, 1261-1315.

Tappe, S., Foley, S. F., Stracke, A., Romer, R. L., Kjarsgaard, B. A., Heaman, L. M. and Joyce, N. (2007). Craton reactivation on the Labrador Sea margins: $^{40}Ar/^{39}Ar$ age and Sr-Nd-Hf-Pb isotope constraints from alkaline and carbonatite intrusives. *Earth and Planetary Science Letters* 256, 433-454.

Tappe, S., Foley, S.F., Kjarsgaard, B.A., Romer, R.L., Heaman, L.M., Stracke, A., Jenner, G.A. (2008). Between carbonatite and lamproite-diamondiferous Torngat ultramafic lamprophyres formed by carbonate-fluxed melting of cratonic MARID-type metasomes. *Geo et Cosmo Acta* 72 (13), 3258–3286.

Tappe, S., Pearson, D. G., Nowell, G. M., Nielsen, T. F. D., Milstead, P. and Muehlenbachs, K. (2011). A fresh isotopic look at Greenland kimberlites: cratonic mantle lithosphere imprint on deep source signal. *EPSL* 305, 235-248.

Tappe, S. and Simonetti, A. (2012) Combined U-Pb geochronology and Sr-Nd isotope analysis of the Ice River perovskite standard, with implications for kimberlite and alkaline rock petrogenesis. *Chem Geol* 304-305, 10-17.

Tappe, S., Pearson, D. G., Kjarsgaard, B. A., Nowell, G., & Dowall, D. (2013). Mantle transition zone input to kimberlite magmatism near a subduction zone: Origin of anomalous Nd–Hf isotope systematics at Lac de Gras, Canada. *Earth and Planetary Science Letters*, *371*, 235-251.

Tappe, S., Kjarsgaard, B., Kurszlaukis, S., Nowell, G. and Phillips, D. (2014). Petrology and Nd-Hf isotope geochemistry of the Neoproterozoic Amon kimberlite sills, Baffin Island, Canada: Further insights on supercontinent cycles. *Journal of Petrology* 55, 2003-2042.

Taylor HP (1968). The oxygen isotope geochemistry of igneous rocks. *Contribution to Mineral Petrology 19:1-71.*

Taylor HP Jr. (1980). The effects of assimilation of country rocks by magmas on ^{18}O-^{16}O and $^{87}Sr/^{86}Sr$ systematics in igneous rocks. *Earth and Planetary Science Letters* 47:243-254

Torsvik, T.H., Burke, K., Steinberger, B., Webb, S.J. and Ashwal, L.D (2010). Diamonds sampled by plumes from the core-mantle boundary. *Nature, Letters*, 466, 352-357.

Wachter, E. A., & Hayes, J. M. (1985). Exchange of oxygen isotopes in carbon dioxide-phosporic acid systems. *Chemical Geology 52*(3), 365-374.

Waters F. G. (1987). A suggested origin of MARID xenoliths in kimberlites by high pressure crystallization of an ultrapotassic rock such as lamproite. *Contrib. Mineral. Petrol*. 95, 523–533.

Whitehouse, M.J., Claesson, S., Sunde, T. and Vestin, J. (1997) Ion microprobe U-Pb zircon geochronology and correlation of Archaean gneisses from the Lewisian Complex of Gruinard Bay, northwestern Scotland. *Geochim. Cosmochim. Acta* 61, 4429-4438.

Williams, I.S., (1998). U–Th–Pb geochronology by ion microprobe. In: McKibben, M.A., Shanks III, W.C., Ridley, W.I. (Eds.), Applications of Microanalytical Techniques to Understanding Mineralizing Processes: *Reviews in Economic Geology*, vol. 7, pp. 1–35.

Wilson, M., Rosenbaum, J.M. and Dunworth, E.A. (1995) Melilitites: Partial melts of the thermal boundary layer? *Contrib. Mineral. Petrol*. 119, 181-196.

Wittig, N., Webb, M., Pearson, D.G., Dale, C.W., Ottley, C.J., Hutchison, M., Jensen, S.M. and Luguet, A. (2010) Formation of the North Atlantic Craton: Timing and mechanisms constrained from Re-Os isotope and PGE data of peridotite xenoliths from S.W Greenland. *Chemical Geology*, 276, 166-187.

Woolley, A.R. and Bailey, D.K. (2012). The crucial role of lithospheric structure in the generation and release of carbonatites: Geological evidence. *Mineralogical Magazine* 76, 259-270.

Wu, F.Y., Yang, Y.H., Mitchell, R.H., Li, Q.L., Yang, J.H. and Zhang, Y.B. (2010) In situ U-Pb age determination and Nd isotopic analysis of perovskites from kimberlites in southern Africa and Somerset Island, Canada. *Lithos* 115, 205-222.

Wu, F.-Y., Arzamastsev, A.A., Mitchell, R.H., Li, Q.-L., Sun, J., Yang, Y.H. and Wang, R.C. (2013) Emplacement age and Sr–Nd isotopic compositions of the Afrikanda alkaline ultramafic complex, Kola Peninsula, Russia. *Chemical Geology* 353, 210-229.

Yang, Y-H., Wu., F-Y., Wilde, S.A., Liu, X-M., Zhang, Y-B. (2009). In situ

perovskite Sr-Nd isotopic constraints on the petrogenesis of the Ordovician Mengyin kimberlites in the North China Craton. *Chemical Geology*, 264, 24-42.

Yaxley, G. M., Kamenetsky, V. S., Nichols, G. T., Maas, R., Belousova, E., Rosenthal, A. and Norman, M. (2013). The discovery of kimberlites in Antarctica extends the vast Gondwanan Cretaceous province. *Nature Communications* 4, 1-7.

Zurevinski, S.E., Mitchell, R.H. (2011). Highly evolved hypabyssal kimberlite sills from Wemindji, Quebec, Canada: insights into the process of flow differentiation in kimberlite magmas. *Contributions to Mineralogy and Petrology* 161, 765-776.

APPENDIX A

PETROGRAPHIC AND DETAILED GEOCHEMICAL OVERVIEW OF THE RENARD KIMBERLITE SUITE

RD-R2-3

Sample RD-R2-3 is a hypabyssal sample from Renard Pipe 2 which was one of the samples selected for Os and HSE analysis. It contains the highest volume of fresh olivine macrocrysts up to 5 mm in diameter (~9 vol. %) out of all the samples analysed in this study, as well as the highest abundance of groundmass spinel and ilmenite (~30 vol. %) (Figs. A1 and A2). Fresh and serpentinized olivine is present as rounded macrocrysts approximately 1 mm in diameter on average. Groundmass phlogopite (<200 μm) is also present in this sample in a minor proportion (~5 vol. %). Primary groundmass carbonate makes up ~30 vol. % of this sample, with prominent secondary calcite veining through the section. This sample falls consistently in the range with the other Renard sample major elements, except that it falls on the higher end of the MgO content, and in the lower end of the LOI and CO_2 contents. It has the lowest Ir, Ru and Pr contents out of the measured Renard samples, and the highest W. It has the highest εNd_i calculated (3.3), apart from the Lynx outlier (see RD-L221-3). It has the highest εHf_i value (6.3) out of the Renard samples. It also has the lowest $\delta^{18}O$ out of the entire sample set.

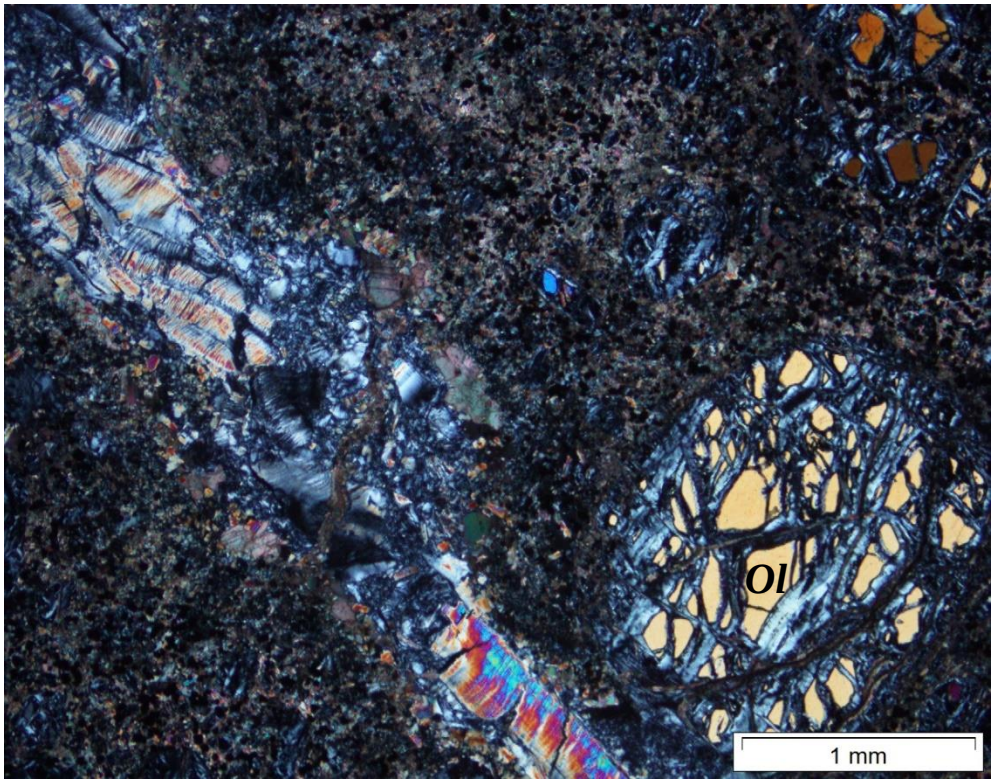

Fig. A1: Sample RD-R2-3 in XPL depicting fresh olivine macrocrysts in a groundmass of phlogopite, spinel, ilmenite and calcite with secondary carbonate veins running through the sample.

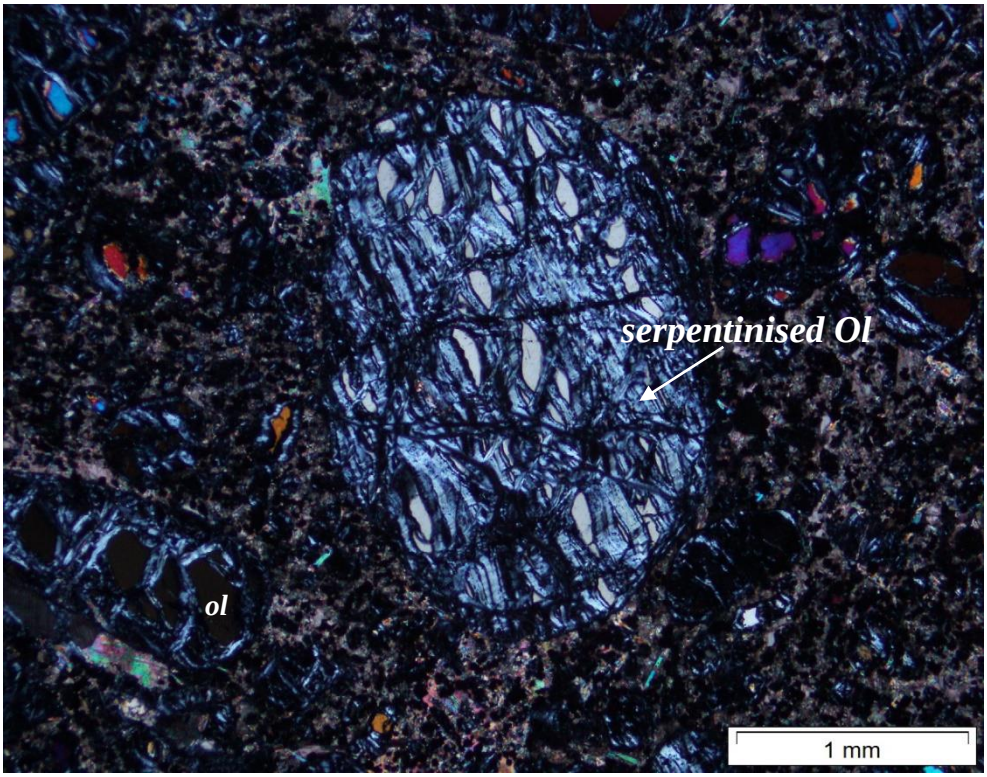

Fig. A2: Sample RD-R2-3 in XPL depicting a serpentinized olivine macrocryst with relict olivine in a groundmass of phlogopite, spinel, ilmenite and calcite.

RD-R2-19

Sample RD-R2-3 is a hypabyssal sample from Renard Pipe 2. This sample was unsuitable for bulk-rock geochemical analysis due to the high abundance of crustal xenoliths in sample material, but useful for geochronological analysis due to the abundance of euhedral perovskite grains (30-40 μm), included in phlogopite microphenocrysts (>200 μm). It contains fresh rounded olivine fragments (~5 vol. %) in a groundmass of spinel and ilmenite (~30 vol. %) (Fig. A3). Serpentinized (20 vol. %) and carbonated (5 vol. %) olivine is present as rounded macrocrysts approximately 1 mm in diameter on average. Primary groundmass carbonate makes up ~25 vol. % of this sample, with minor secondary calcite veining through the section.

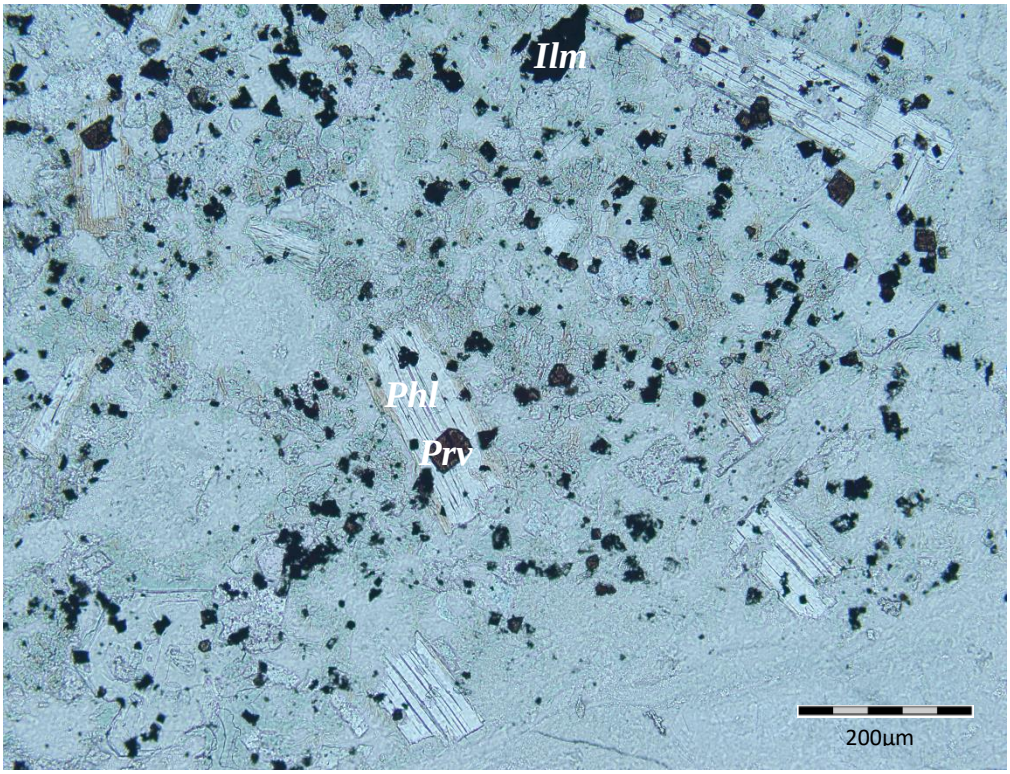

Fig. A3: Sample RD-R2-19 in PPL depicting perovskite inclusions in phlogopite microphenocrysts in a calcite-ilmenite-spinel groundmass

RD-R3-07

Sample RD-R3-07 is a Renard Pipe 3 sample which was one of the samples selected for Os and HSE analysis. It contains a high volume of fresh olivine (~5 vol. %) (Fig. A4). It contains large primary, euhedral calcite grains that host/partially host large euhedral phlogopite microphenocryst laths and euhedral perovskite grains (Fig. A4). Serpentinised (20 vol. %) olivine macrocrysts are present up to 3 mm in diameter, set in a calcite-spinel-ilmenite groundmass. There are also secondary calcite veins running thorough this sample. This sample falls consistently in the range with the other Renard sample major elements, except that it is on the higher end of the K_2O content, and in the lower end of the CO_2 content. It contains the highest Cs, Rb, Ba contents. It contains the highest Os, Ir, Ru and Pd contents out of all the measured Renard samples. It has the lowest εNd_i calculated (1.2). It has the lowest εHfi value (1.7) out of the Renard samples. It also has the lowest $\delta^{18}O$ out of the entire sample set. It has the lowest calculated γOs_i out of the Renard samples.

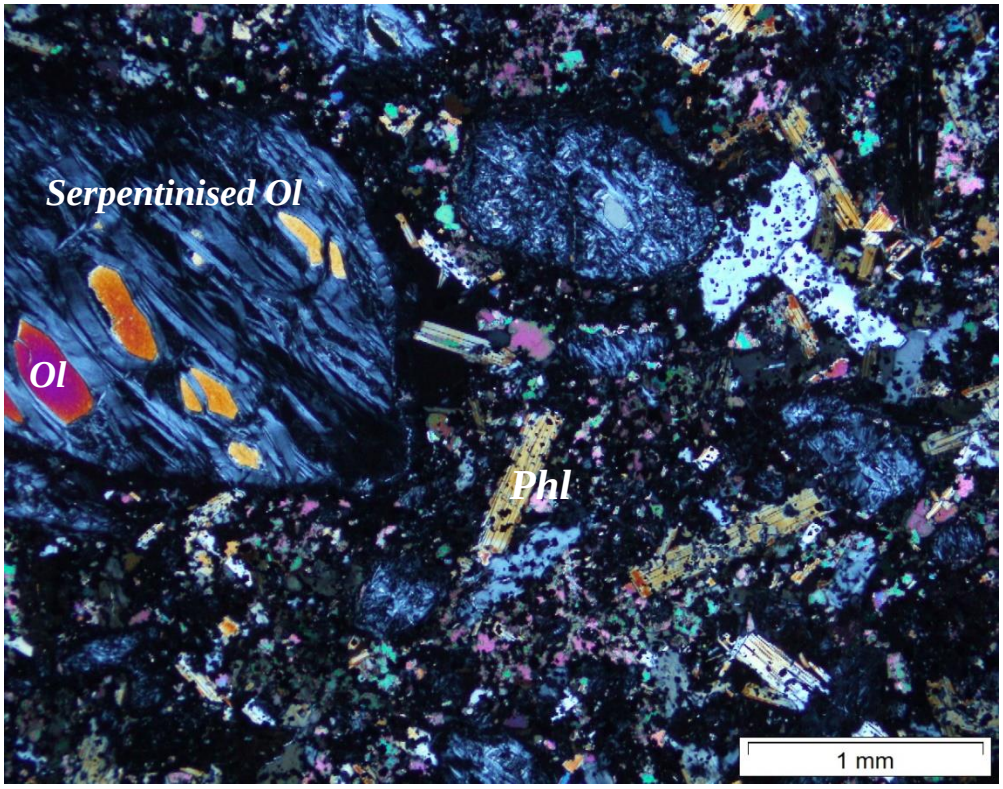

Fig. A4: Sample RD-R3-07 in XPL showing serpentinized olivine macrocrysts with relict olivine, with phlogopite laths in a groundmass of calcite, phlogopite, spinels, ilmenite and perovskite.

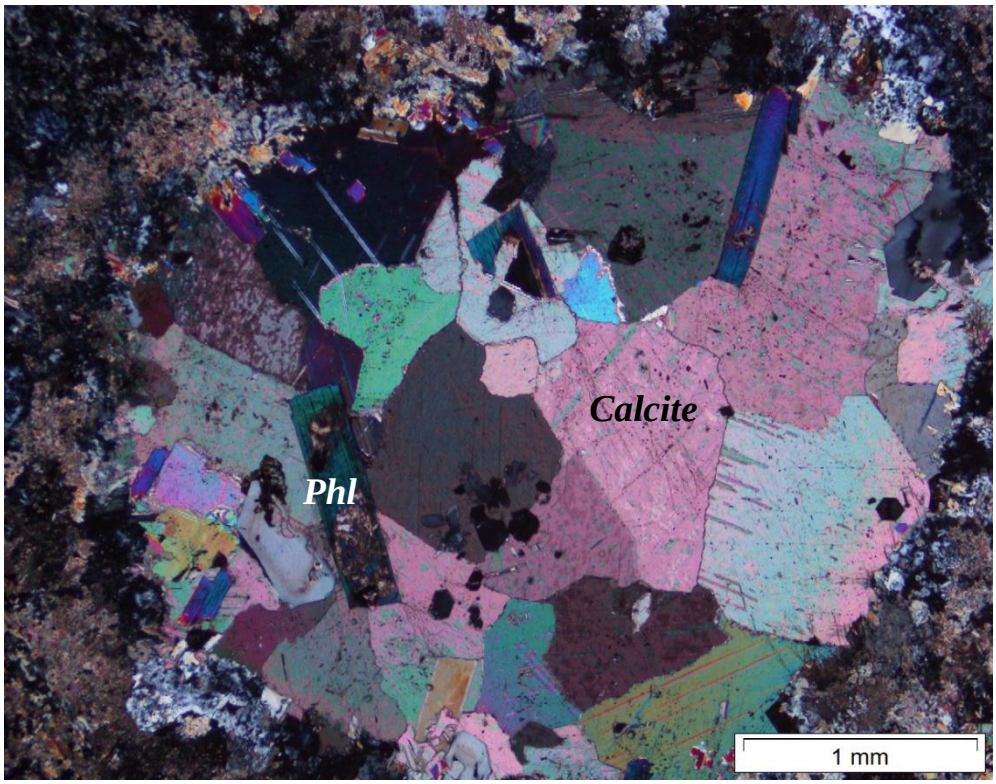

Fig. A5: Sample RD-R3-07 in XPL showing primary calcite with large phlogopite laths and minor perovskite inclusions

RD-11646

Sample RD-11646 is a Renard Pipe 3 sample. It contains the second highest volume of fresh olivine (~8 vol. %) in the sample suite analysed (Fig. A6). Serpentinised (20 vol. %) olivine macrocrysts are present at an average of 2 mm in diameter, set in a calcite (~30 vol. %)- phlogopite-spinel-ilmentite groundmass. Groundmass perovskite is present as subhedral grains ~40 μm in size. It falls consistently in the range with the other Renard sample major elements, except that it has the highest SiO_2 content of the Renard samples, the highest Al_2O_3, MgO, K_2O contents of the entire data set and the lowest LOI and CO_2 contents of the entire dataset. It has the lowest initial Sr calculated value and the lowest $\delta^{13}C$ value out of the entire dataset.

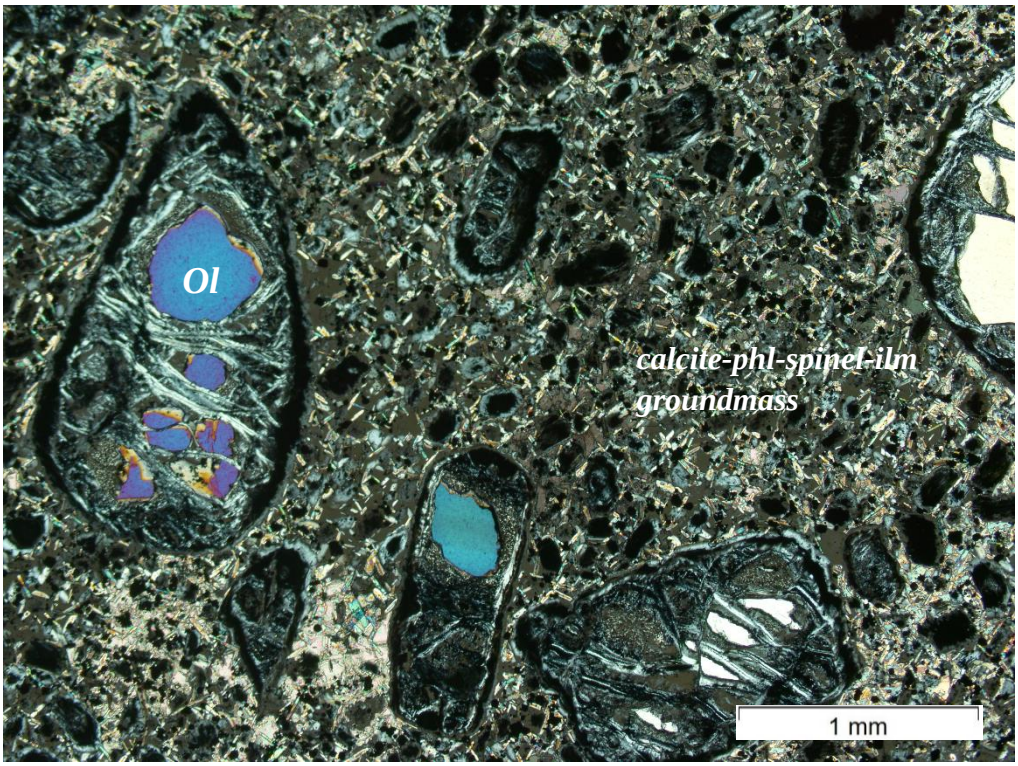

Fig. A6: Sample RD-11646 in XPL showing fresh olivine macrocrysts in a calcite-phlogopite-spinel-ilmenite groundmass

RD11649

Sample RD11649 is a Renard Pipe-3 sample. It contains the highest abundance of olivine macrocrysts in the Renard samples, replaced by secondary calcite (~20 vol. %) as well as serpentine (~25 vol. %). Large phlogopite microphenocryst laths, ~500 μm on average are also present throughout the sample along with altered olivine macrocrysts in a groundmass of ilmenite, spinel, calcite, phlogopite and minor (~1 vol. %) perovskite (Fig. A7 and A8). Primary carbonate content makes up approximately 20 vol. % of this sample, with secondary veining cross-cutting relict olivine macrocrysts (Fig. A7). This sample falls consistently in the range with the other Renard sample major elements. It has one of the highest concentrations of Cs, Rb in the Renard cluster. It has one of the lowest εHf_i values (2.8) and one of the highest $\delta^{18}O$ values out of the Renard kimberlites.

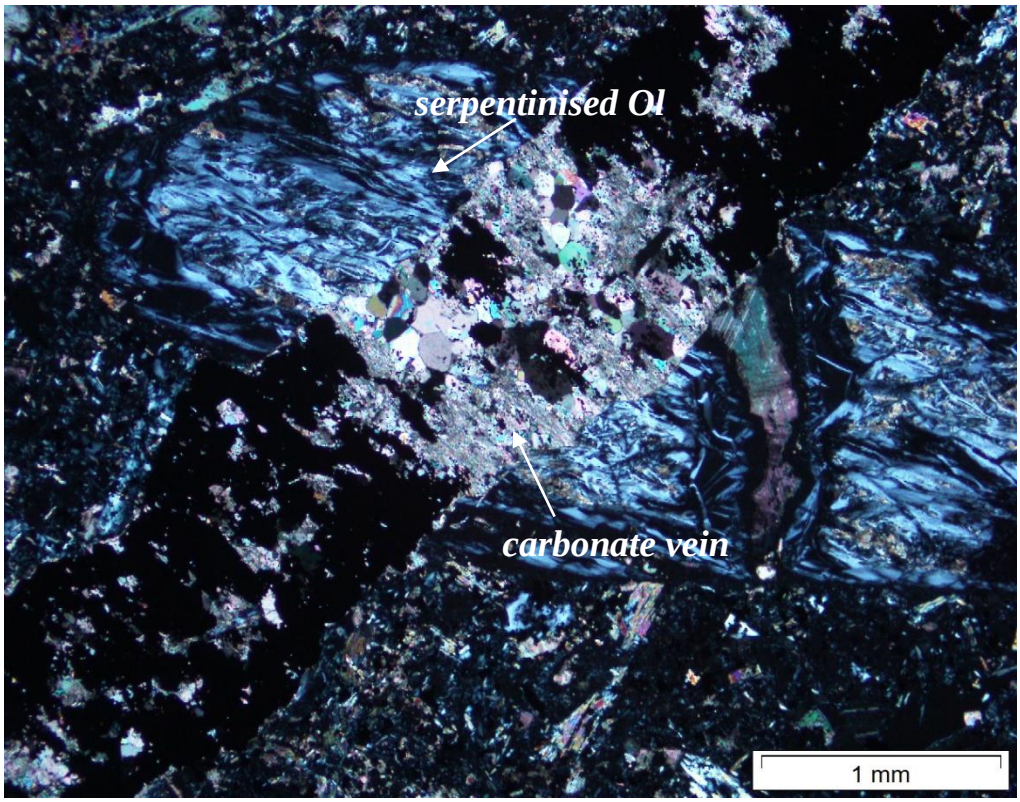

Fig. A7: Sample RD11649 in XPL showing a serpentinized olivine macrocryst, cross-cut by a vein formed from a carbonate-rich fluid.

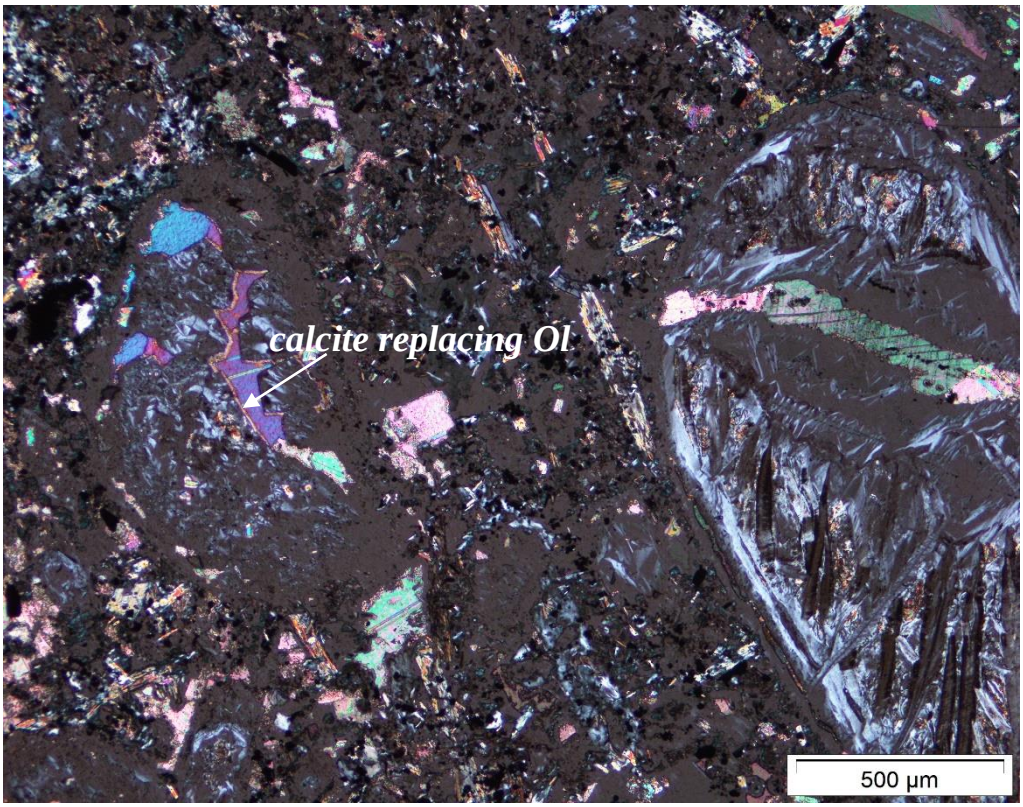

Fig. A8: Sample RD11649 in XPL showing olivine grains replaced by calcite, with subhedral phlogopite laths in a groundmass of spinel and ilmenite.

RD-11650

Sample RD-11650 is a Renard Pipe-3 sample and was selected for analysis of Os and HSE. It is the final sample in the list of Renard suite hosting fresh olivine (~2 vol. %). Olivine macrocrysts up to 5 mm in diameter in this sample are highly altered and replaced by calcite (8 vol. %) and serpentine (25 vol. %). This sample contains large primary, euhedral calcite grains. The groundmass is predominantly primary calcite (30 vol. %) with lesser phlogopite, ilmenite and perovskite (Figs. A9 and A10). This sample falls consistently in the range with the other Renard sample major elements. It contains the highest concentration of Cs and Mo in the Renard sample set. It contains the highest concentration of Re (0.106 ppb) in all of the samples measured. This sample also contains the highest measured $^{187}Os/^{188}Os$ value (0.132075) and therefore highest γOs_i (1.634) out of the entire measured dataset.

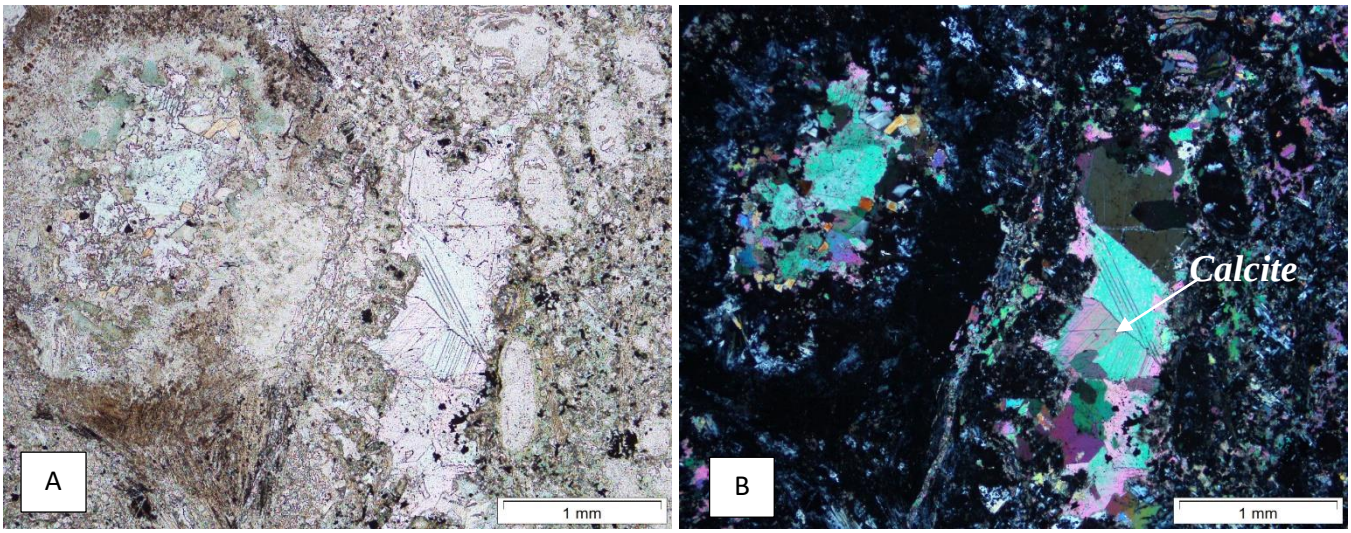

Fig. A9: Sample RD11650 in PPL (A) and XPL (B) showing primary subhedral carbonate grains in a groundmass of carbonate, spinel, ilmenite and phlogopite.

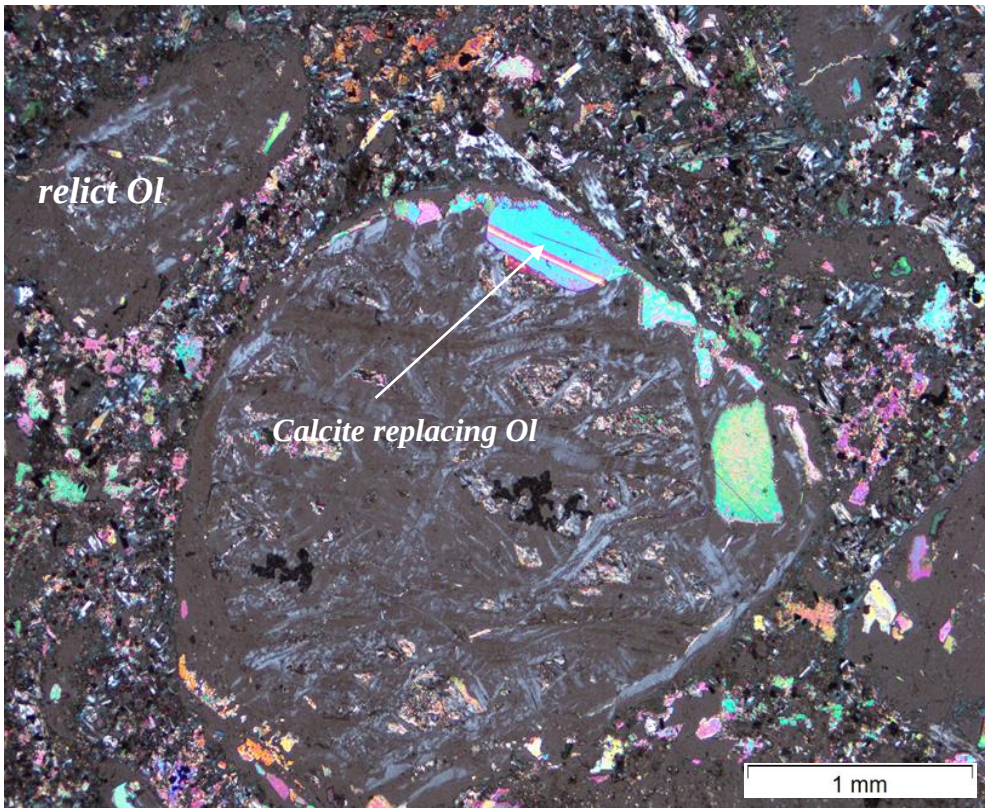

Fig. A10: Sample RD11650 in XPL showing olivine macrocrysts replaced by calcite.

RD-L221-3

Sample RD-L221-3 is a Renard sample from the Lynx dyke. It contains subhedral calcite microphenocrysts (>200 μm), in a groundmass comprising serpentinized olivine (<200 μm), calcite and ilmenite (Fig. A11). Minor (~10 vol. %) phlogopite

is also present, along with secondary calcite veining. This is the most anomalous sample out of the Renard suite, with the lowest Si concentration (19.5 wt. % SiO_2), highest Ti content (5.76 wt. % TiO_2), highest Al content (6.11 wt. % Al_2O_3), highest MnO content (out of the entire data set) and overall highest Fe concentration. It has the lowest Na_2O concentration out of the entire dataset (b.d). It also has the lowest K and highest P and Cr out of the entire dataset. Even with all of these anomalous values taken into account, the contamination index of this sample remains 0.99. It contains the lowest concentration of Cs in the entire dataset, and the lowest Rb in the Renard dataset. It also contains the highest Th, U, Nb, Ta, Hf, Pr, Nd and Ga in the entire datatset, and is elevated in all other trace elements compared to other samples in the Renard Suite. It has the highest εNd_i calculated in the Renard suite (4.6) and the second highest εHf_i calculated (5.4). The $\delta^{18}O$ is the second lowest in the Renard sample set.

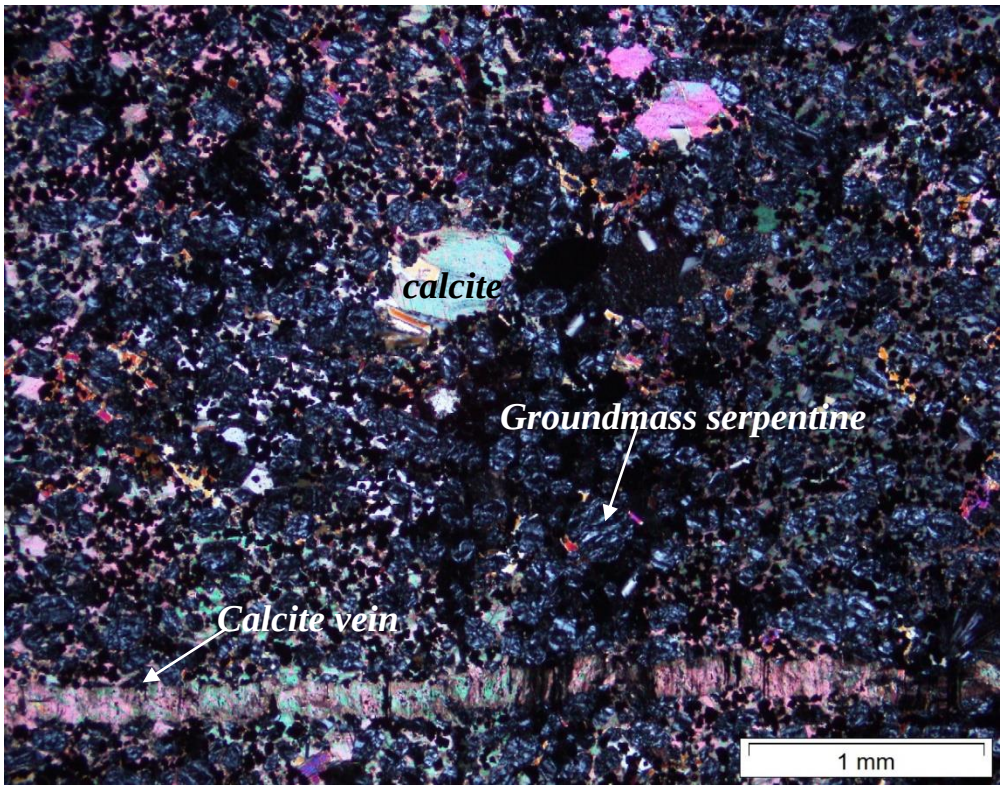

Fig. A11): Sample RD-L221-3 in XPL showing primary calcite grains in a groundmass of serpentinized olivine, calcite and ilmenite. Also pictured is a secondary calcite vein running though the sample.

RD-L221-7

Sample RD-L221-7 is a Renard sample from the Lynx dyke. It consists of microphenocrystic serpentinized olivine (~34 vol. %) and minor phlogopite microphenocrysts (200-400 μm) in a calcite-ilmenite-spinel groundmass (Figs. A12 and A13).

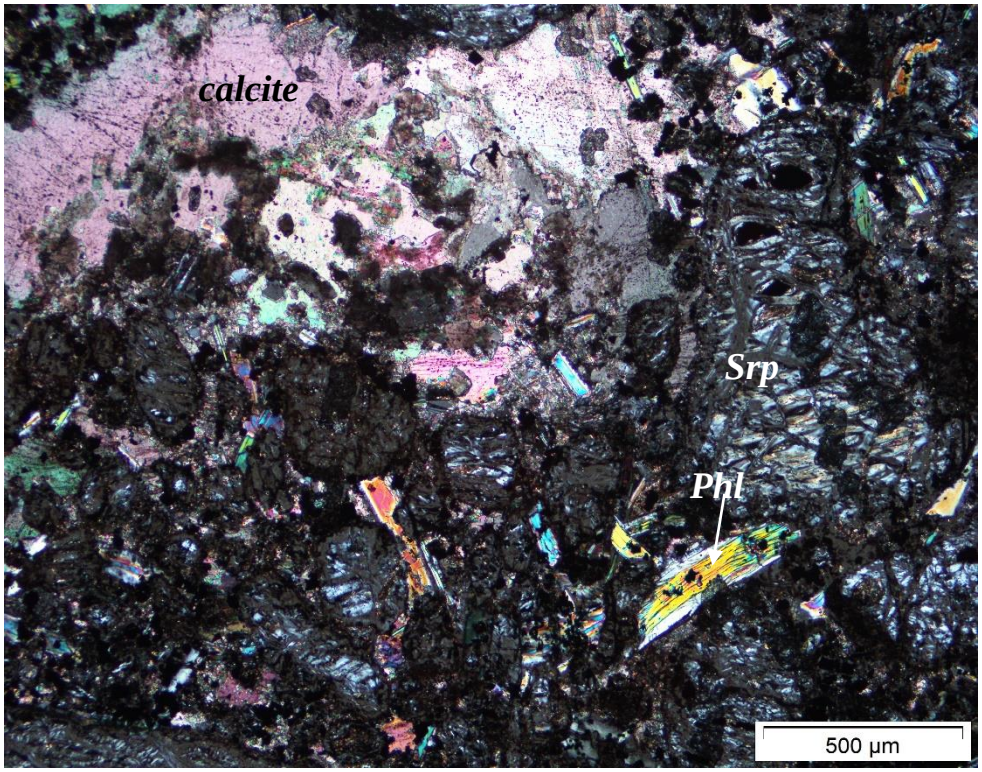

Fig. A12: Sample RD-L221-7 in XPL showing primary calcite grains, phlogopite microphnocrysts and serpentinised rounded olivine microphencrysts

It contains an abundance of primary and secondary carbonate groundmass (~30 vol. %) and as vein material. These veins occur on average at 500 μm thickness (Fig. A13). This sample falls consistently in the range with the other Renard sample major elements. It has the highest LOI (19.9%) and second highest CO_2 concentrations on the Renard cluster (10.44 wt. %). It contains the highest Co concentration out of the Renard suite.

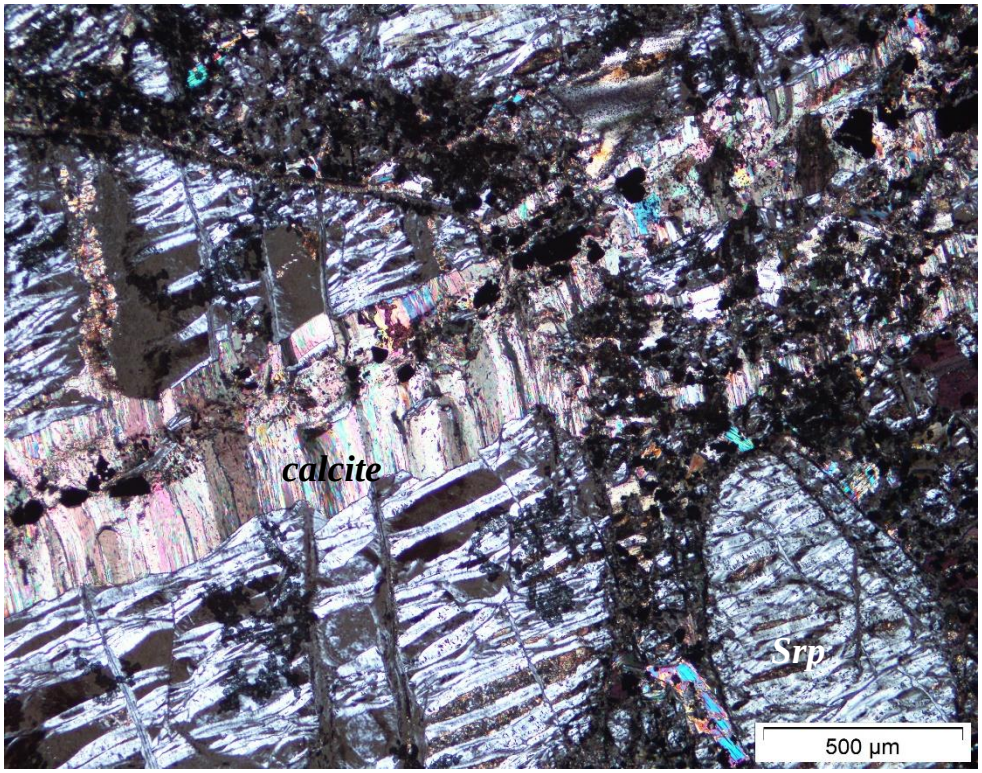

Fig. A13: Sample RD-L221-7 in XPL showing serpentinized olivine macrocrysts cross-cut by a ~500 µm calcite vein.

RD-L230-5

Sample RD-L230-5 is a Renard sample from the Lynx dyke. It is petrographically similar to the previous sample (RD-L221-7). The olivine macrocrysts present in this sample are serpentinized and carbonated, reaching up to 5 mm in diameter. Rounded groundmass olivine (~100 µm) is serpentinized. It contains a visibly higher abundance of spinel and ilmenite (~20 vol. %), as well as a slightly higher volume of primary carbonate (~30 vol. %) (Fig. A14). This sample is a kimberlite of the Lynx dyke. It falls consistently in the range with the other Renard sample major elements. It contains the second highest overall Fe content in the Renard cluster and the highest CO_2 (10.85 wt. % CO_2). It has the highest Li content out of the Renard set.

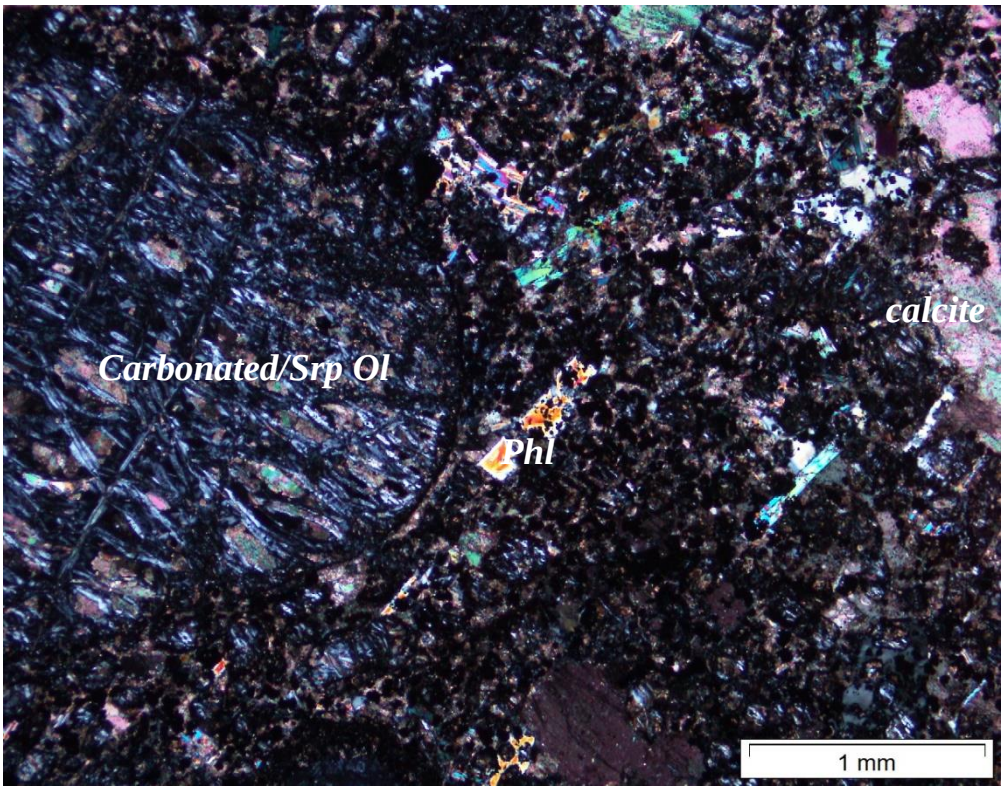

Fig. A14: Sample RD-L230-5 in XPL showing a serpentinized and carbonated olivine macrocryst in a groundmass of spinel, ilmenite and phlogopite

RD-L230-6

Sample RD-L230-6 is a Renard sample form the Lynx dyke. It contains a higher volume (~45 vol. %) of serpentinized olivine as compared to the ~20-30 vol. % from the previous two Lynx dyke kimberlite samples (Fig. A15). Phlogopite laths are present as subhedral microphenocrysts, which act as oikocrysts to spinel and ilmenite grains. It contains a small volume (~10 vol. %) of ilmenite and spinel in the groundmass, with the remainder of the groundmass made up by primary calcite (~25 vol. %). This sample falls consistently in the range with the other Renard sample major elements. It contains the highest concentration of Pb in the Renard suite (64.7 ppm). It has the highest initial Sr calculated value (0.70765).

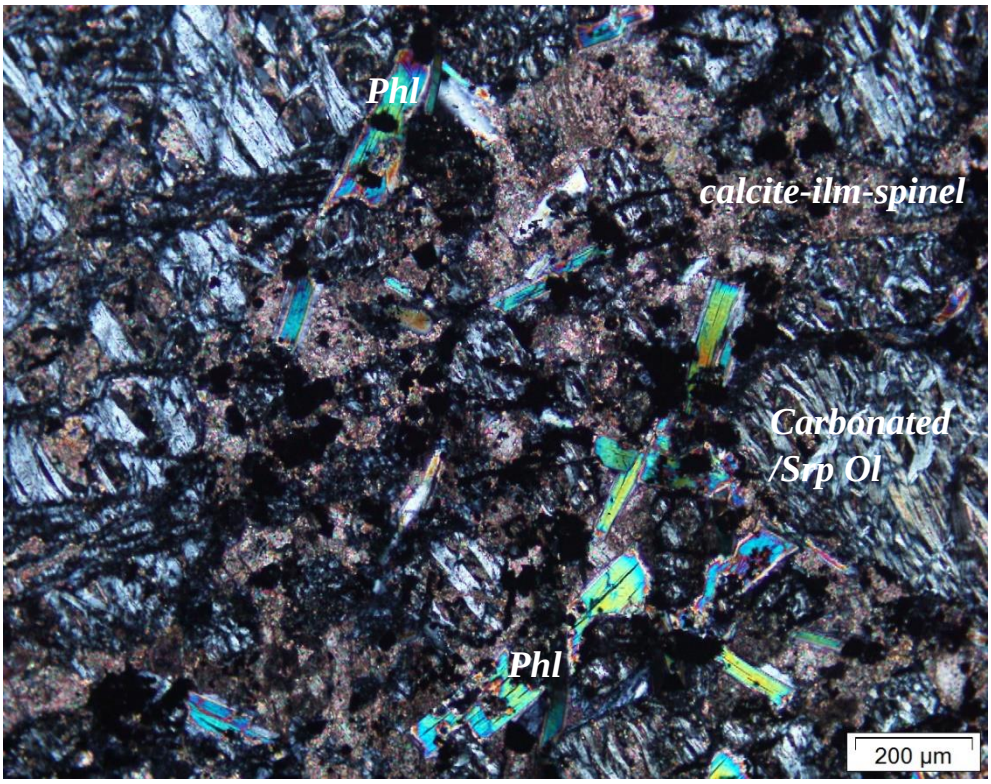

Fig. A 15: Sample RD-L230-6 in XPL showing serpentinized and carbonated olivine grains and subhedral phlogopite laths in a groundmass of spinel, ilmenite and calcite.

RD-H5

Sample RD-H5 is a Renard sample from the Hibou dyke. It is petrographically similar to the Renard hypabyssal pipe and the Lynx dyke material. This sample contains the largest serpentinised olivine macrocrysts out of all samples analysed, reaching up to 7 mm in diameter (Figs. A16 and A17). Phlogopite macrocrysts (500 µm) are present, hosting spinel and ilmenite grains. The groundmass consists of ~35 vol. % calcite and ~10 vol. % ilmenite and spinel, as well as rounded serpentinized olivine. Minor (~1 vol. %) perovskite grains are also present, and are ~30 µm in diameter. This sample falls consistently in the range with the other Renard sample major elements. Within the Renard sample set, this sample contains the lowest concentration of La, Ce, Pr, Nd, Sm, Eu, Gd, Tb, Dy, Ho, Er, Zn, and V.

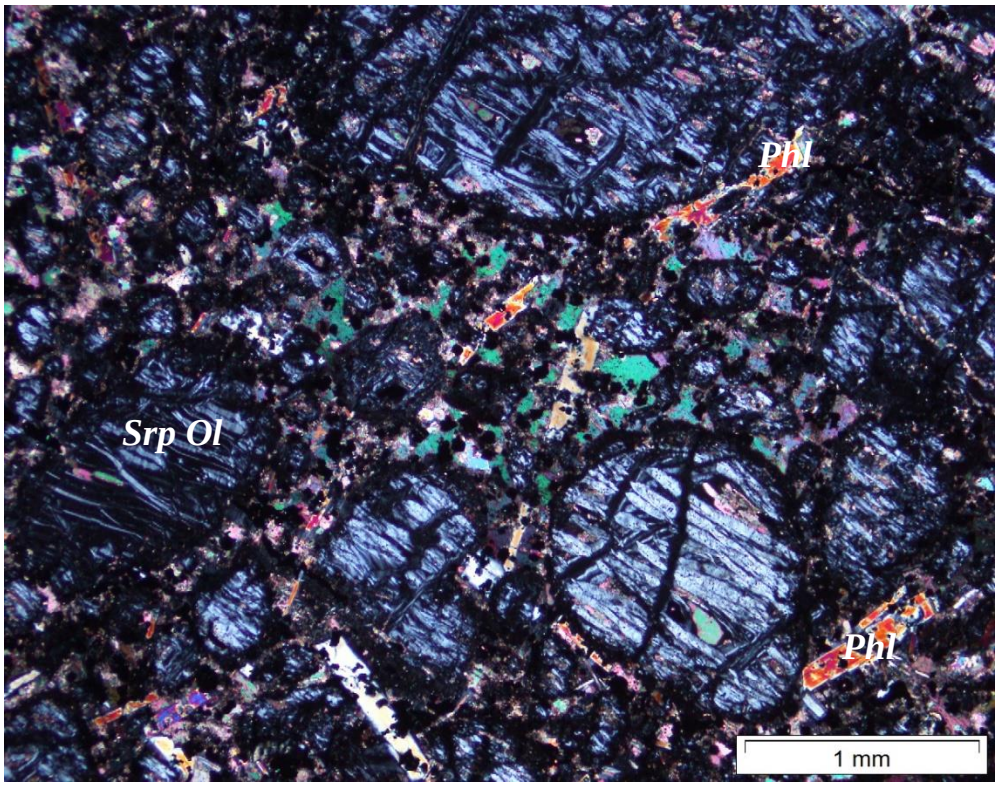

Fig. A16: Sample RD-H5 in XPL showing serpentinized and carbonated olivine macrocrysts and subhedral phlogopite laths in a groundmass of spinel, ilmenite and calcite.

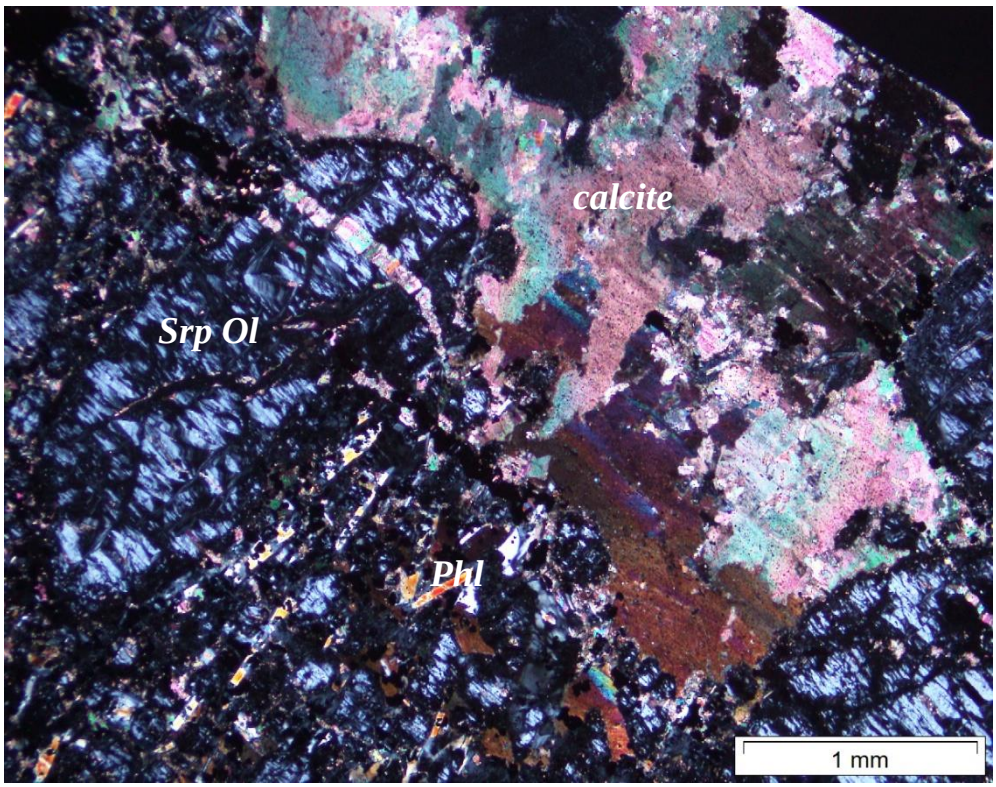

Fig. A17: Sample RD-L230-6 in XPL showing serpentinized and carbonated olivine macrocrysts and primary calcite grains, with secondary calcite veins running through the sample.

APPENDIX B

PETROGRAPHIC AND DETAILED GEOCHEMICAL OVERVIEW OF THE WEMINDJI KIMBERLITE SUITE

Wemindji kimberlite sheet samples analysed in this study are visibly more differentiated in terms of flow textures, as well as, in general, being more altered than the Renard kimberlites.

WEM-02-09 10/1A

Sample WEM-02-09 10/1A consists of serpentinised olivine macrocrysts, 2 mm in diameter, in a groundmass of calcite (~30 vol. %), ilmenite and spinel (Fig. B1 and B2). Olivine in this sample has been completely replaced by serpentine or calcite or both (Fig. B2). This sample falls consistently in the range of major elements for Wemindji kimberlite sheets, except that it contains the highest concentration of Al_2O_3 out of the Wemindji sample set. It also contains the highest concentration of Zr (out of the entire dataset), Hf and V in the Wemindji sample set. It also has the highest calculated εHf_i in the entire dataset (6.5).

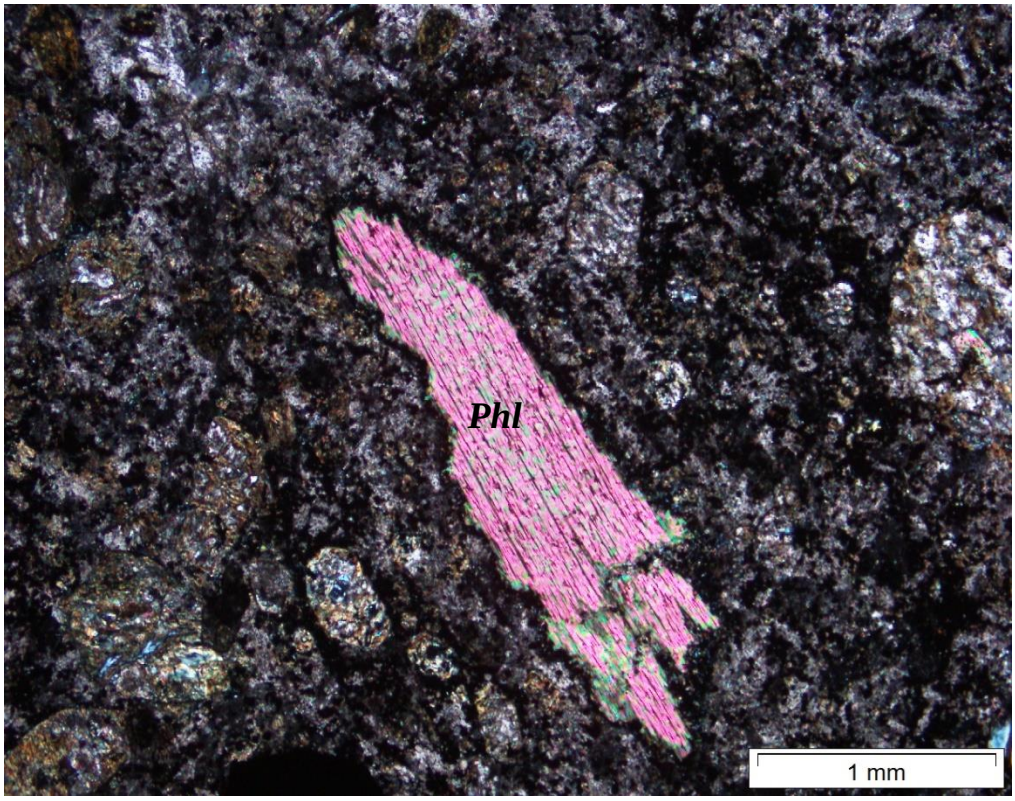

Fig. B1: Sample WEM-02-09 10/1A in XPL showing relict olivine grains completely serpentinized/ carbonated with a phlogopite phenocryst.

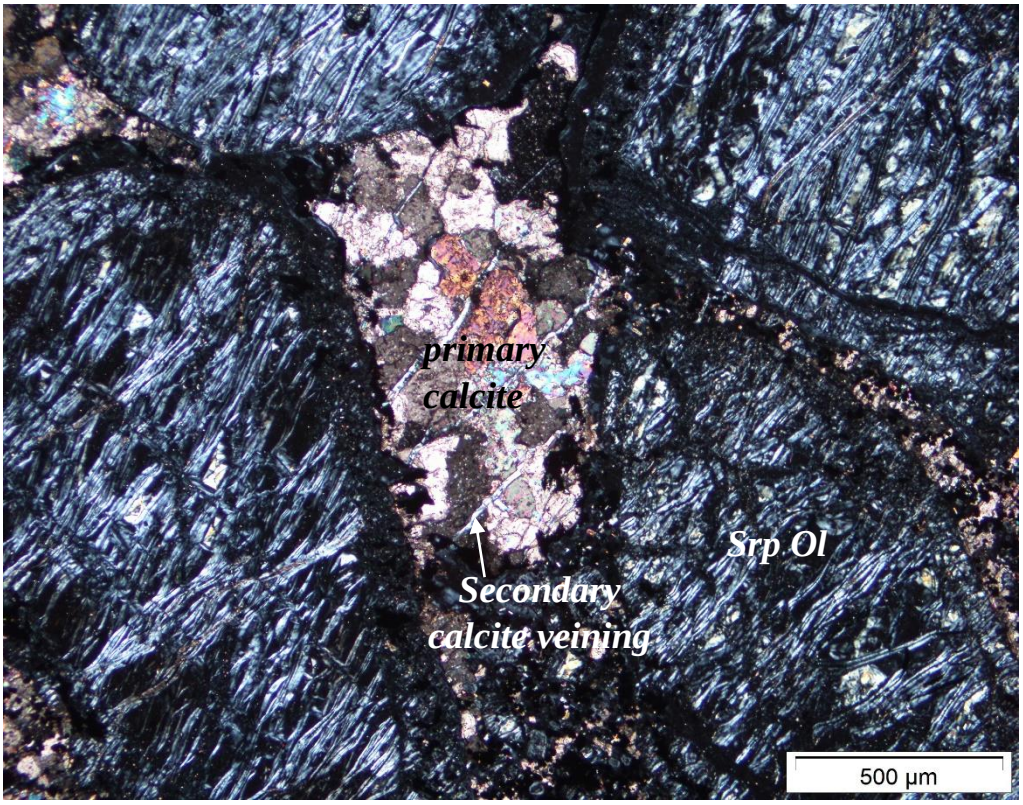

Fig. B2: Sample WEM-02-09 10/1A in XPL showing serpentinized olivine macrocrysts surrounding a cluster of primary calcite grains with secondary calcite veins.

WEM-02-09 10/3

Sample WEM-02-09 10/3 contains ~30 vol. % of a primary calcite groundmass which is host to serpentinized olivine macrocrysts up to 5 mm in diameter and accessory garnet (Fig. B3). There is no apparent groundmass phlogopite. This sample falls consistently in the range of major elements for Wemindji kimberlite sheets. It contains the highest concentration of Ba, Pr, Nd, Sm, Sc, V out of the Wemindji kimberlites and the highest Sr (1720ppm) and Pb (79.8ppm) and La (344ppm) and Co, Cu concentration in the entire dataset.

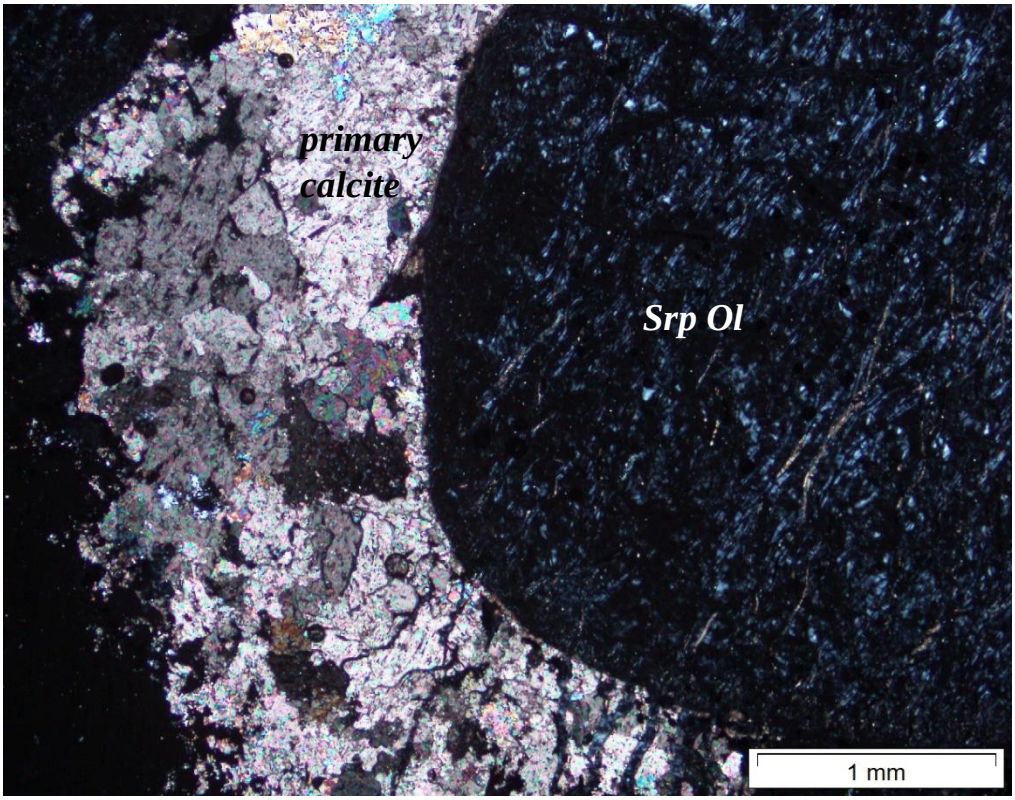

Fig. B3: Sample WEM-02-09 10/3 in XPL showing a serpentinized olivine macrocryst in a primary calcite groundmass

WEM-02-09 10/6

Sample WEM-02-09 10/6 contains serpentinized (20 vol. %) and carbonated (15 vol. %) olivine macrocrysts up to 3 mm in diameter, set in an ilmenite/spinel-rich calcite (30 vol. %) groundmass (Fig. B4). This sample falls consistently in the range of major elements for Wemindji kimberlite sheets, except that it contains the highest abundance of K_2O out of the Wemindji dataset. It also contains the highest Ce out of the entire dataset and the highest Pr and Nd out of the Wemindji kimberlites, as well as the lowest Ga concentration in the Wemindji set and the highest W concentration in the entire dataset.

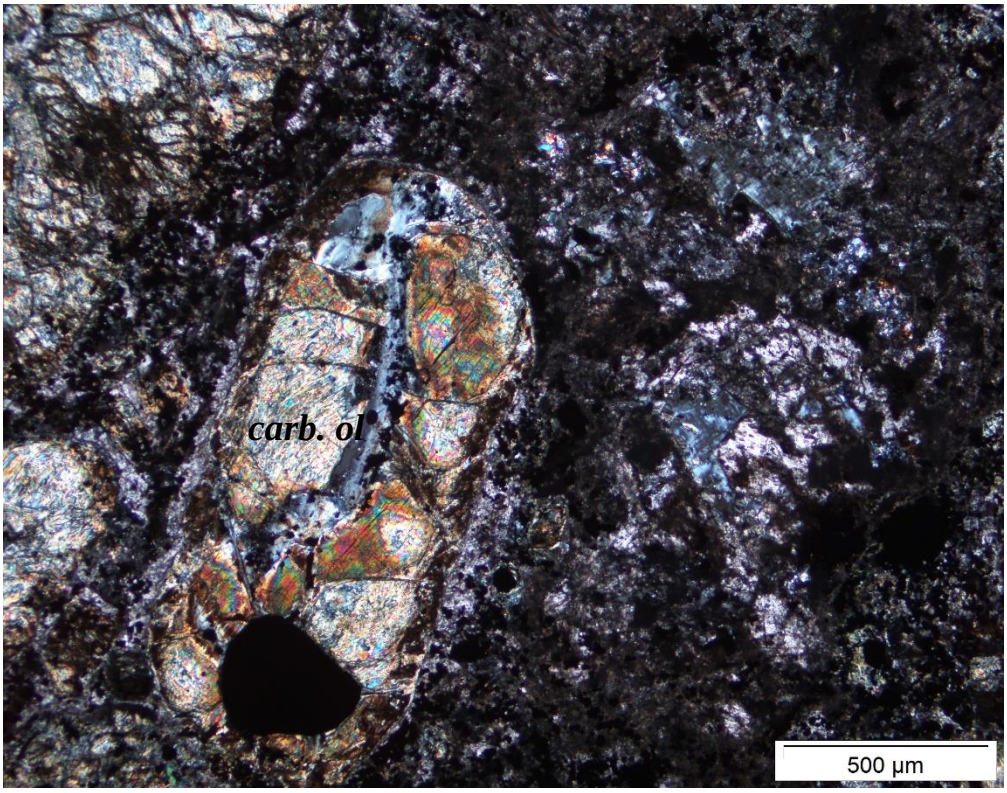

Fig. B4: Sample WEM-02-09 10/6 in XPL showing a carbonated olivine macrocryst with an ilmenite macrocryst inclusion in an ilmenite/spinel -rich calcite groundmass

WEM-02-09 10/10

Sample WEM-02-09 10/10 represents an example of the flow differentiation textures observed in many of the Wemindji kimberlite samples (Fig. B5).Serpentinized olivine macrocrysts are present as ~10 vol. %, in a groundmass dominated by calcite (~60 vol. %), with lesser ilmenite and spinel. Groundmass ilmenite and spinel grains are concentrated along these physical flow planes. This sample falls consistently in the range of major elements for Wemindji kimberlite sheets, except that it contains the lowest concentration of Si (15.2 wt. % SiO_2) and Cr (0.07 wt. % Cr_2O_3) and Ni 0.02 wt. % NiO_2) in the entire dataset and the highest Ti content out of the Wemindji kimberlites (1.45 wt. % TiO_2). It also yielded the highest LOI value (31.6) and the highest CO_2 value (31.6 wt. %) in the entire dataset. It contains the highest concentration of Th, Sm, Eu, Gd, Tb, Dy, Ho, Er, and Y in the entire dataset and the highest Nb and Ga in the Wemindji dataset. It also contains the lowest Ta, W and Zn concentration of the entire

dataset, while it has the lowest Pb, and Hf in the Wemindji dataset. It has the highest εNd_i calculated value (4.8) out of the entire dataset as well as the lowest calculated εHf_i (1.1) in the entire dataset apart from the clearly crustally contaminated sample (see next sample WEM-02-10). It also contains the lowest $\delta^{18}O$ value in the Wemindji dataset.

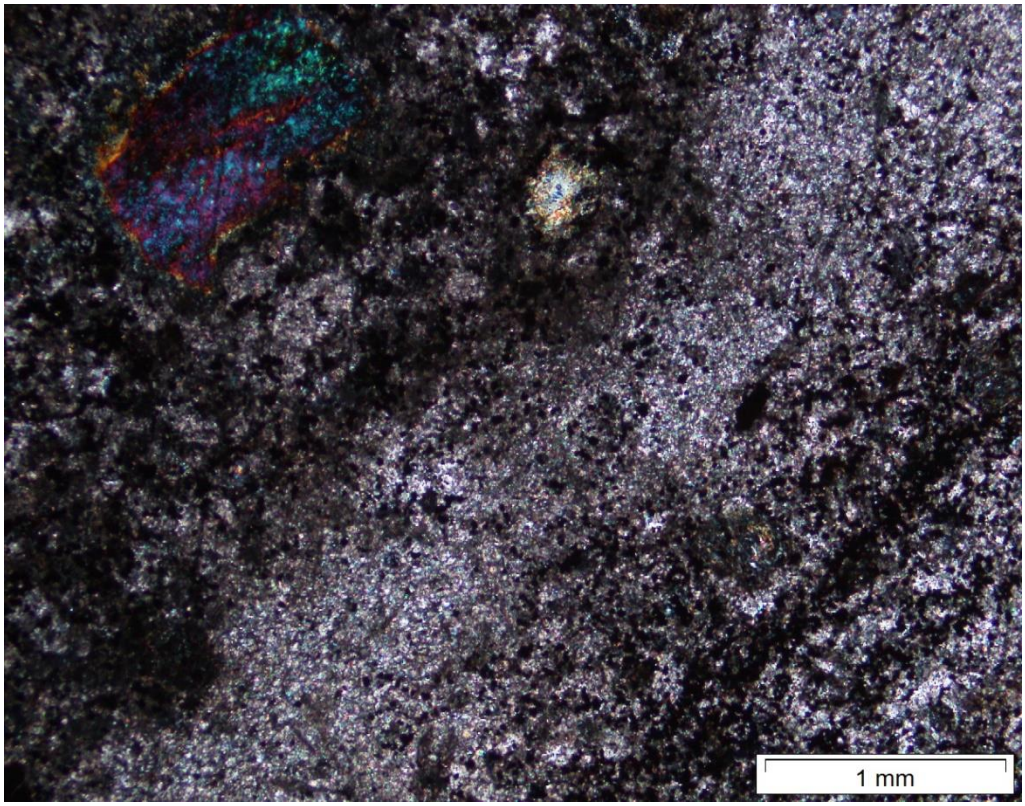

Fig. B5: Sample WEM-02-09 10/10 in XPL demonstrating flow textures observed throughout many of the Wemindji samples, with ilmenite and spinels concentrating on flow planes

WEM-02-10

Sample WEM-02-10 consists of serpentinized (25 vol. %) and carbonated (10 vol. %) olivine macrocrysts with sparse, highly altered xenocrysts, in a groundmass comprising 45 vol. % primary calcite, and 5 vol. % spinel and ilmentite (Fig. B6 and B7). It contains the lowest MnO and MgO contents out of the entire dataset, and the highest CaO content (31.8 wt. % CaO) out of the entire dataset. It has a contamination index value of 2.55. This sample contains the highest concentrations of U in the entire dataset and the lowest Pb in the Wemindji dataset. It has the highest measured Sr value (0.710043) and therefore the highest initial Sr calculated ration (0.70970) out of the entire dataset. It also has the lowest

measured $^{176}Hf/^{177}Hf$ value (0.282338) and therefore the lowest calculated $^{176}Hf/^{177}Hf_i$ value (0.28217). It has the lowest calculated εHf_i value (-7.7). It also has the highest $\delta^{13}C$ value of the entire dataset (-3.88 ‰) and the highest $\delta^{18}O$ in the Wemindji dataset.

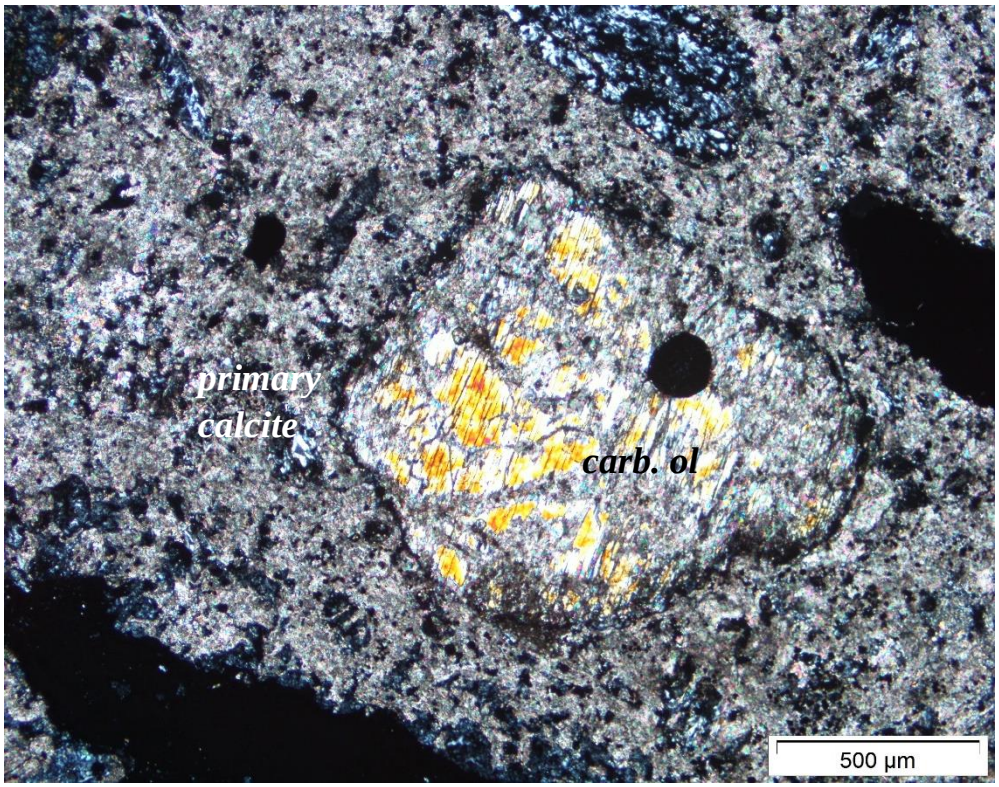

Fig. B6: Sample WEM-02-10 in XPL as an example of the characteristic carbonated Wemindji kimberlite samples

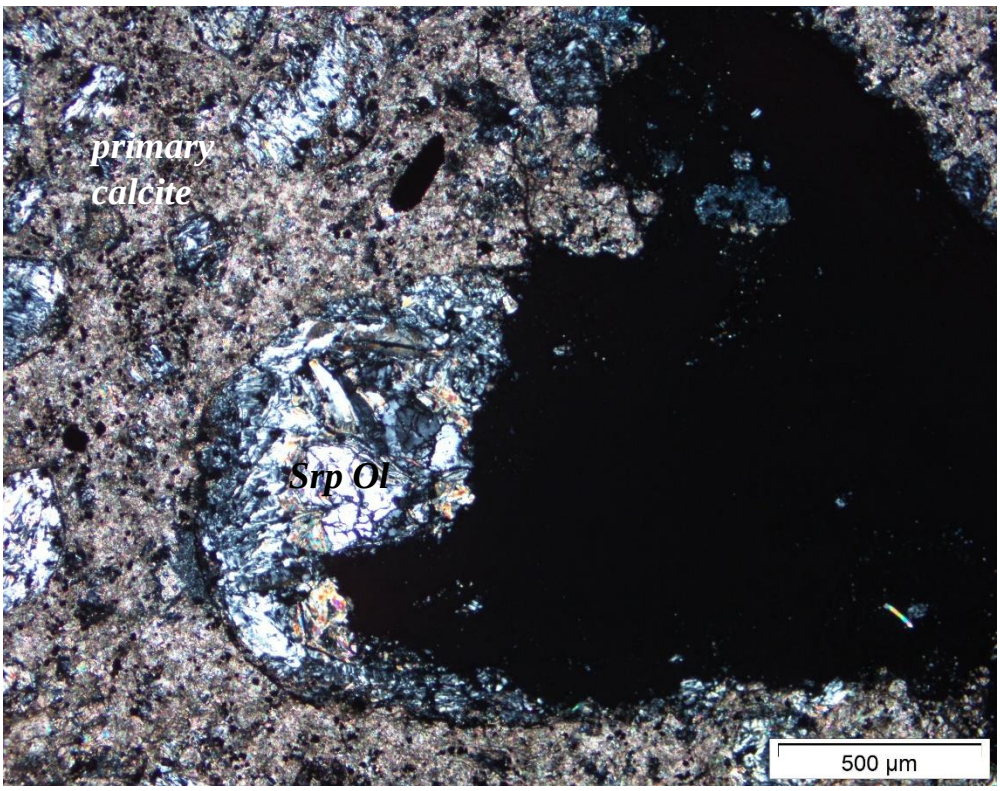

Fig. B7: Sample WEM-02-10 in XPL as an example of the characteristic carbonated Wemindji kimberlite samples, with serpentinized olivine macrocrysts

WEM-02-22 24

Sample WEM-02-22 24 is texturally gradational in hand sample, from fine-grained to coarser-grained olivine macrocrysts (30 vol. %), in a groundmass of calcite and ilmenite, with minor phlogopite. Fresh olivine can be distinguished in macrocrysts of ~ 500 μm diameter, making up ~2 vol. % of the sample (Fig. B8). This sample was measured for Os and HSE. This sample falls consistently in the range of major elements for Wemindji kimberlite sheets, except that it contains the lowest concentration of K_2O in the entire dataset. It also contains the lowest concentration of Cs and Li in the Wemindji dataset and the lowest concentration of Rb in the entire dataset. This sample contains the lowest concentration of Re (0.016 ppb) and Os (0.150 ppb). It has the lowest Sr initial value of the Wemindji samples.

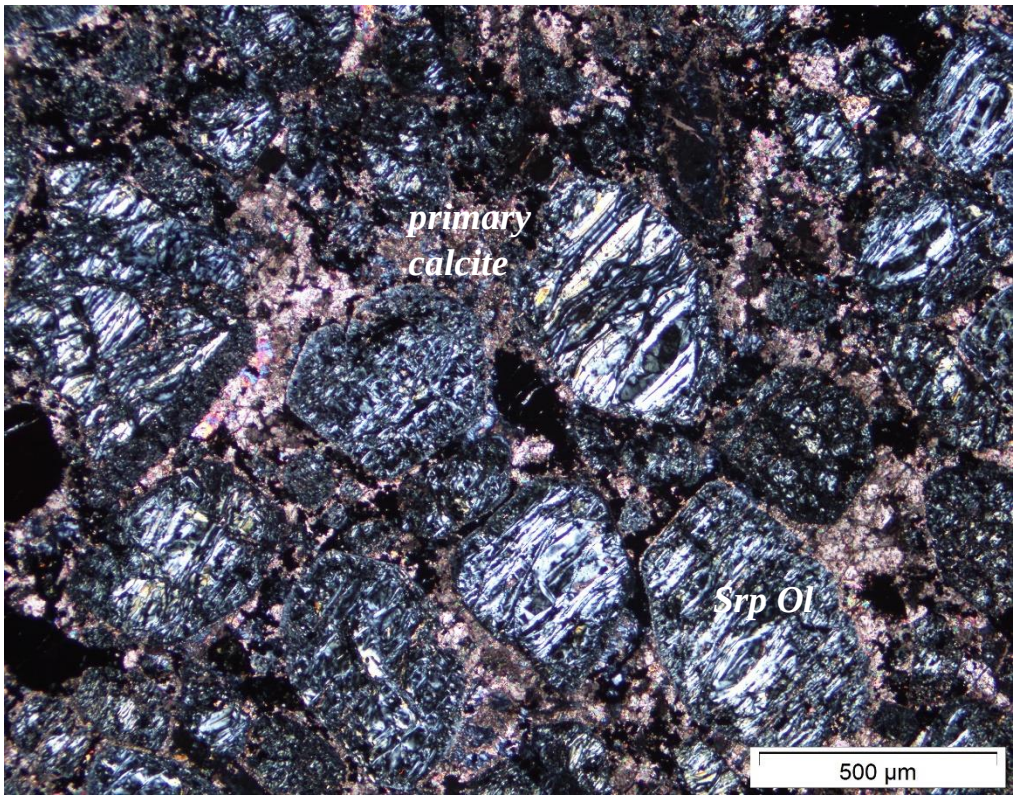

Fig. B8: Sample WEM-02-22 24 in XPL with serpentinized olivine macro- and microcrysts with minor fresh olivine in a calcite-dominated groundmass

WEM-02-22 25

Sample WEM-02-22 25 is composed of serpentinized olivine macrocrysts (25 vol. %) with minor garnet xenocrysts (~2 mm) in a carbonate-rich groundmass, with lesser groundmass spinel and ilmenite (16 vol. %) (Fig. B9). This sample falls consistently in the range of major elements for Wemindji kimberlite sheets, except that it contains the highest NiO content out of the Wemindji samples.

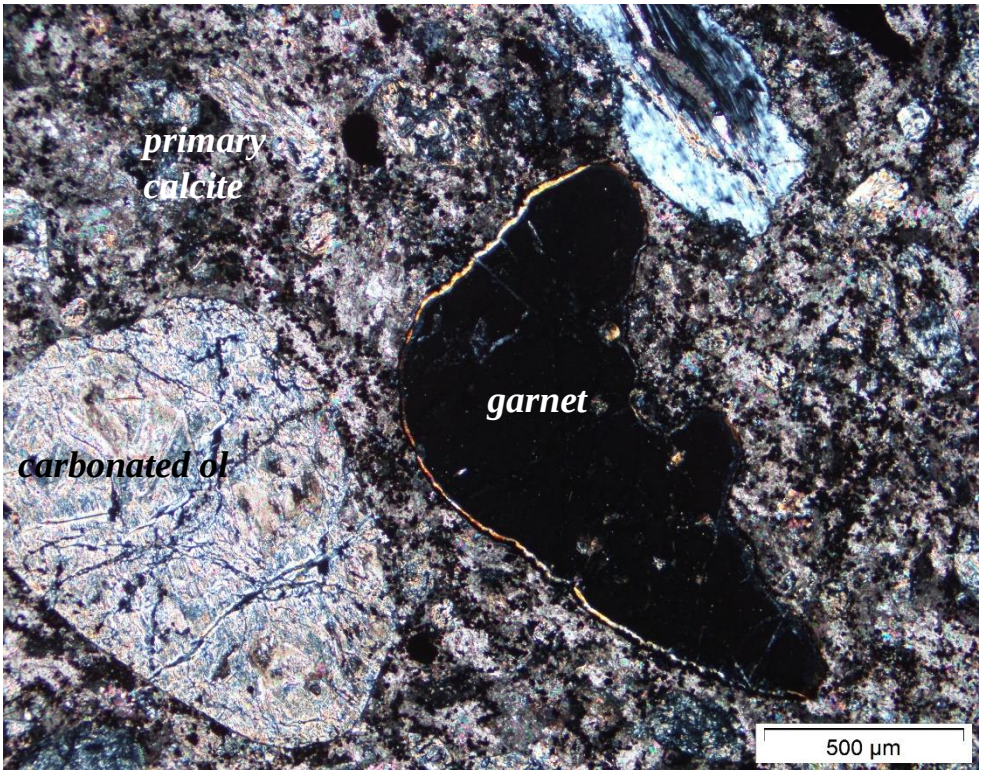

Fig. B9: Sample WEM-02-22 25 in XPL showing a garnet xenocryst and carbonated olivine macrocryst in a calcite-dominated groundmass

WEM-02-26 1

Sample WEM -02-26 1 contains minimal fresh olivine (~2 vol. %) preserved in macrocrysts averaging 1 mm in diameter, which have been serpentinized (Fig. B10). These macrocrysts are set in a calcite, spinel and ilmenite groundmass. This sample was measured for Os and HSE. This sample falls consistently in the range of major elements for Wemindji kimberlite sheets, except that it contains the highest MgO content and the lowest K_2O out of the Wemindji samples. It contains the lowest concentration of Cs, Nb and Mo out of the Wemindji Samples. It

contains the highest concentration of Re, Ru, Pd and Pt sampled set. It also has the lowest γOs_i value out of the entire dataset measured (-13.65).

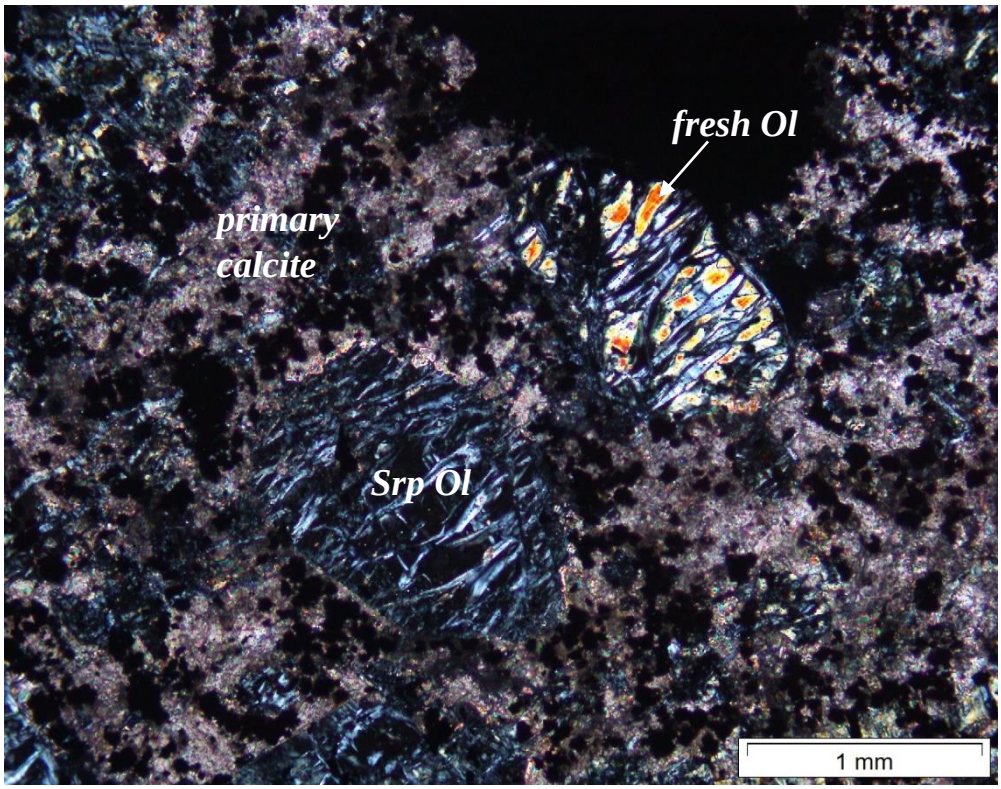

Fig. B10: Sample WEM-02-26 1 in XPL showing fresh olivine in partially serpentinized macrocrysts in a calcite-ilmenite-spinel groundmass

WEM-02-26 2

Sample WEM-02-26 2 contains minimal fresh olivine (~2 vol. %) preserved in macrocrysts which have been carbonated, set in a calcite-dominated groundmass (Fig. B11). This sample was measured for Os and HSE. This sample falls consistently in the range of major elements for Wemindji kimberlite sheets, except that it contains the highest concentration of Si (37.2 wt. % SiO_2) and Na_2O in the entire sample set, the lowest concentration of Al_2O_3 in the Wemindji sample set. It contains the highest concentration of Cs, Li and Mo in the entire dataset. It contains the highest concentration of Os (1.259 ppb) out of all the samples measured. It also has the highest Ir concentration out of all of the samples measured. It has the lowest εNd_i calculated value out of the entire dataset (0.2).

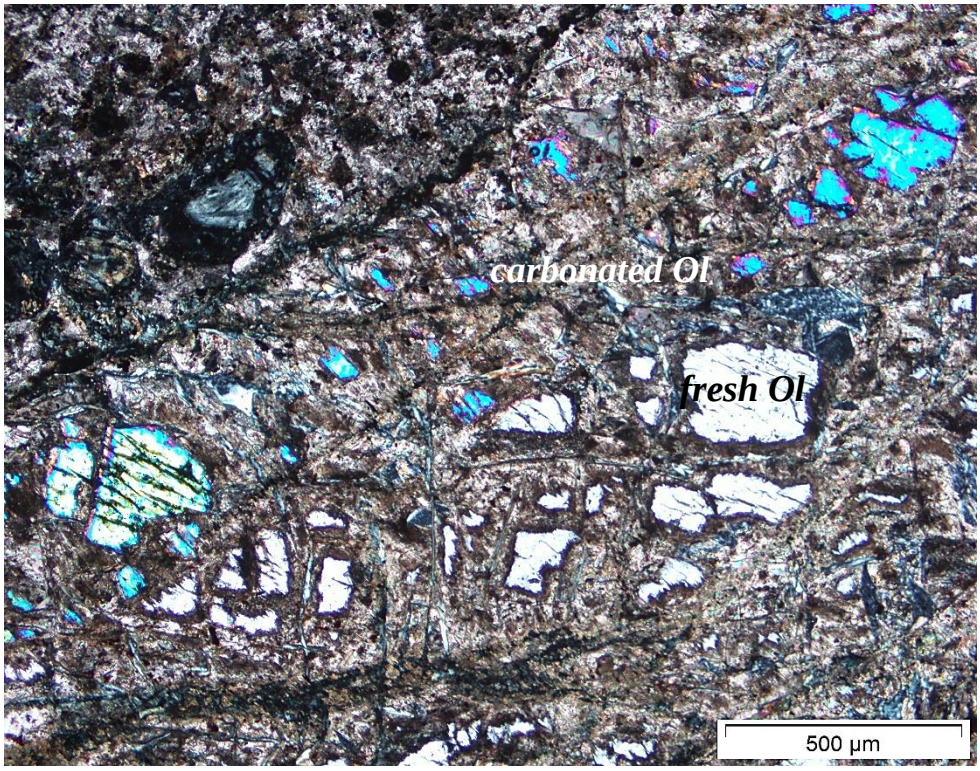

Fig. B11: Sample WEM-02-26 2 in XPL showing fresh olivine in carbonated macrocrysts in a calcite-rich groundmass

WEM-02-26 3

A thin section for sample WEM-02-26 3 was not prepared. This sample falls consistently in the range of major elements for Wemindji kimberlite sheets, except that it contains the highest TiO_2 and overall Fe concentration out of the entire dataset. It has the lowest NaO_2, P_2O_5 and K_2O and CO_2 in the Wemindji dataset. It has the lowest concentrations of Sr, Th, and U in the Wemindji dataset. It has the highest concentration of Ta in the Wemindji dataset and lowest Y, La, Ce, Pr, Nd, Sm, Eu, Tb, Dy, Ho, Er, Tm, Yb, Lu and Sc in the entire dataset.

APPENDIX C

ADDITIONAL FIGURES AND PLOTS

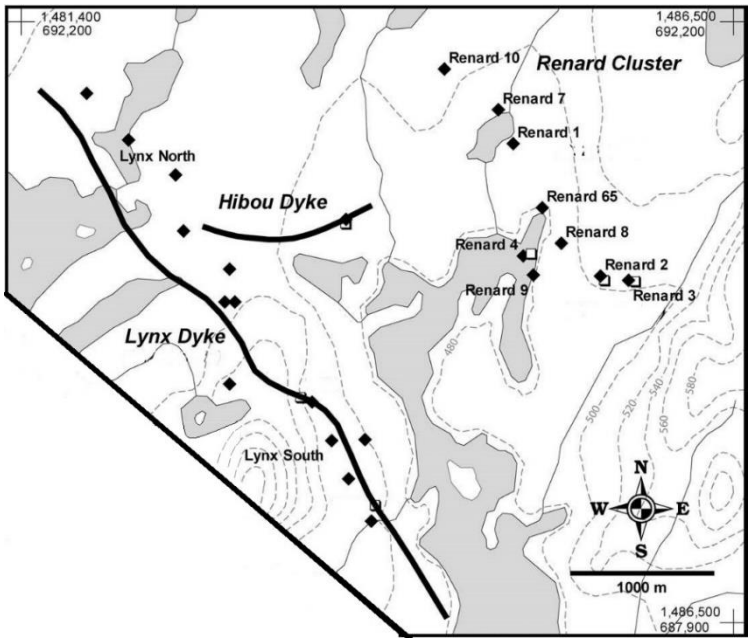

Fig. C1: Simplified geological map of the Renard kimberlite suite, which includes pipes 1, 2,3,4, 65, 7, 8, 9, and 10, the Lynx dyke and the Hibou dyke (after Patterson *et al.*, 2009)

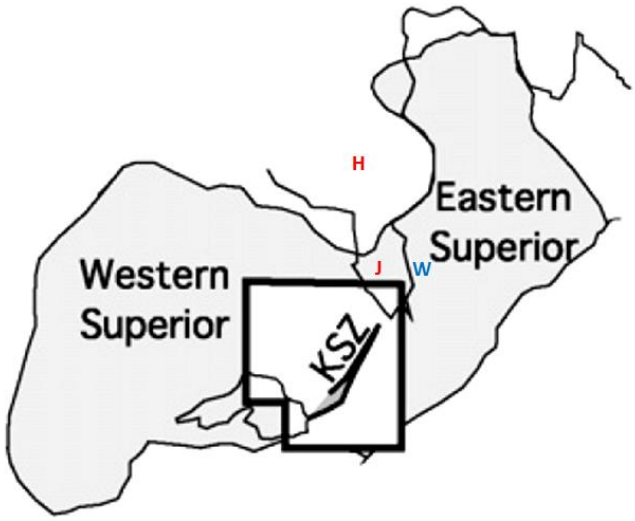

Fig. C2: Simplified map of the Superior Craton, transected by the Kapuskasing Structural Zone (KSZ) (modified after Evans & Halls, 2010). H = Hudson Bay, J = James Bay, W = approximate location of the Wemindji Kimberlite sheets. The Wemindji area appears to lie on the extension of the KSZ

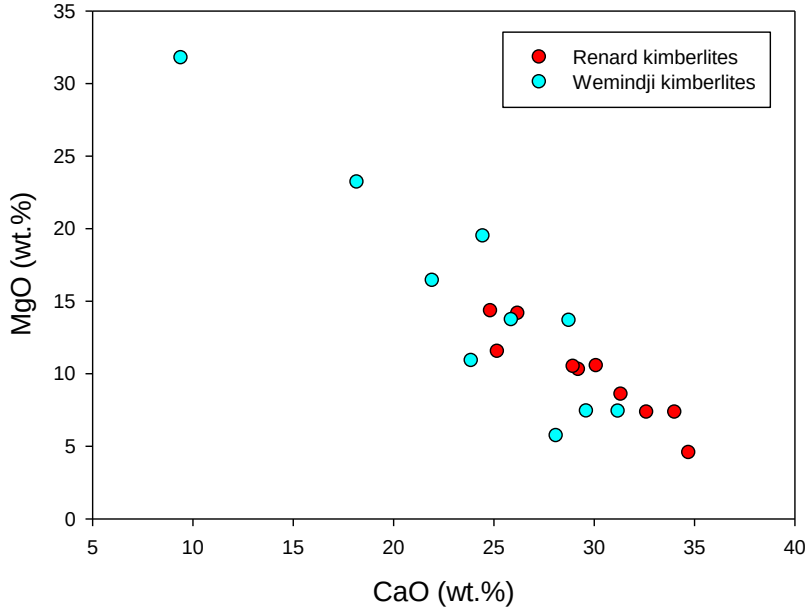

Fig. C3: Plot depicting the inversely proportional relationship between MgO and CaO in the Renard and Wemindji kimberlites.

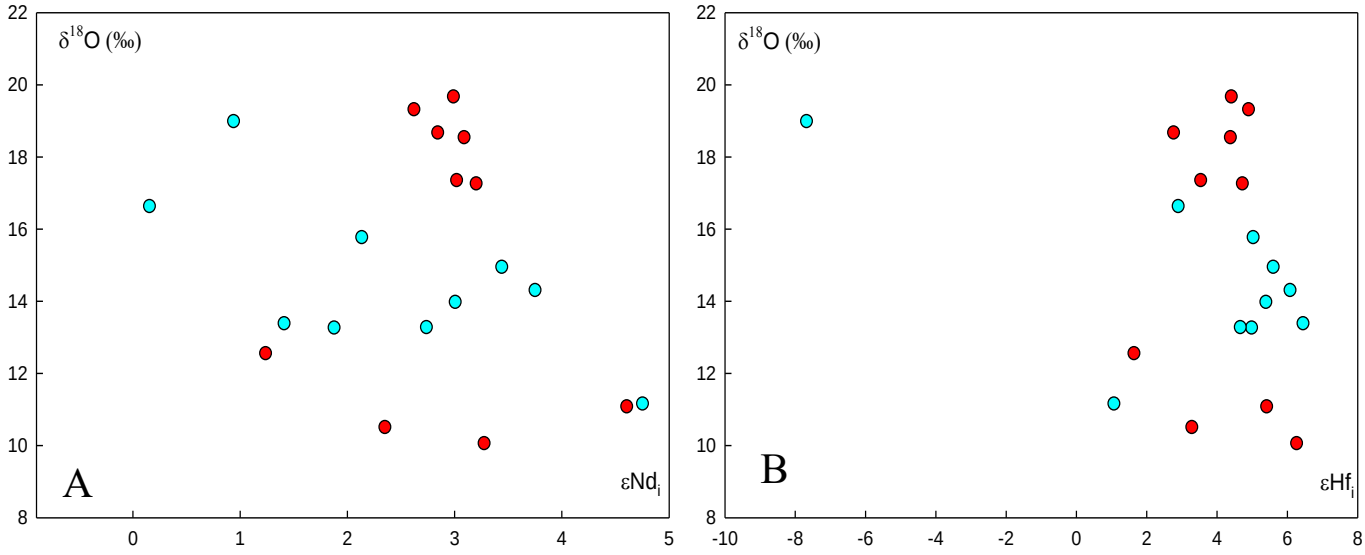

Fig. C4: $\delta^{18}O$ vs ε_{Ndi} (A) and $\delta^{18}O$ vs ε_{Hfi} (B) plots to demonstrate the lack of correlation between the radiogenic and stable $\delta^{18}O$ isotopic systems.

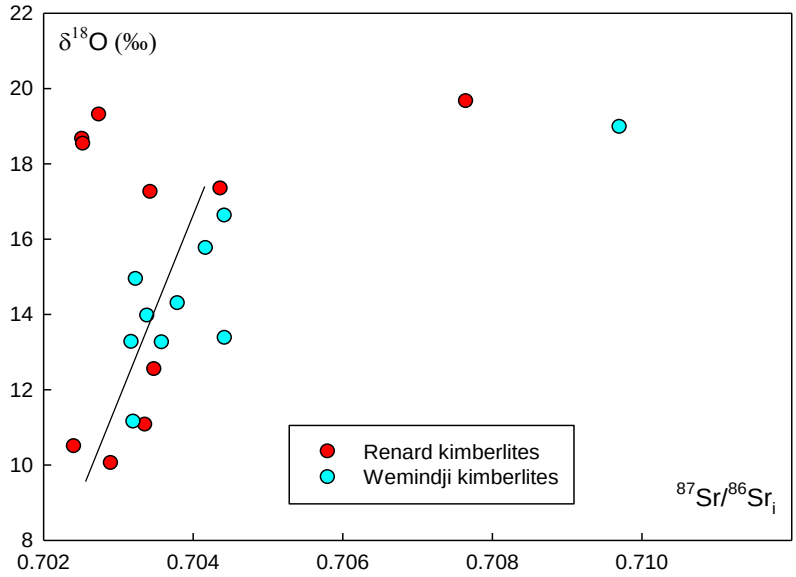

Fig. C5: $\delta^{18}O$ vs $^{87}Sr/^{86}Sr_i$ plot to demonstrate the correlation between these two isotopic systems.

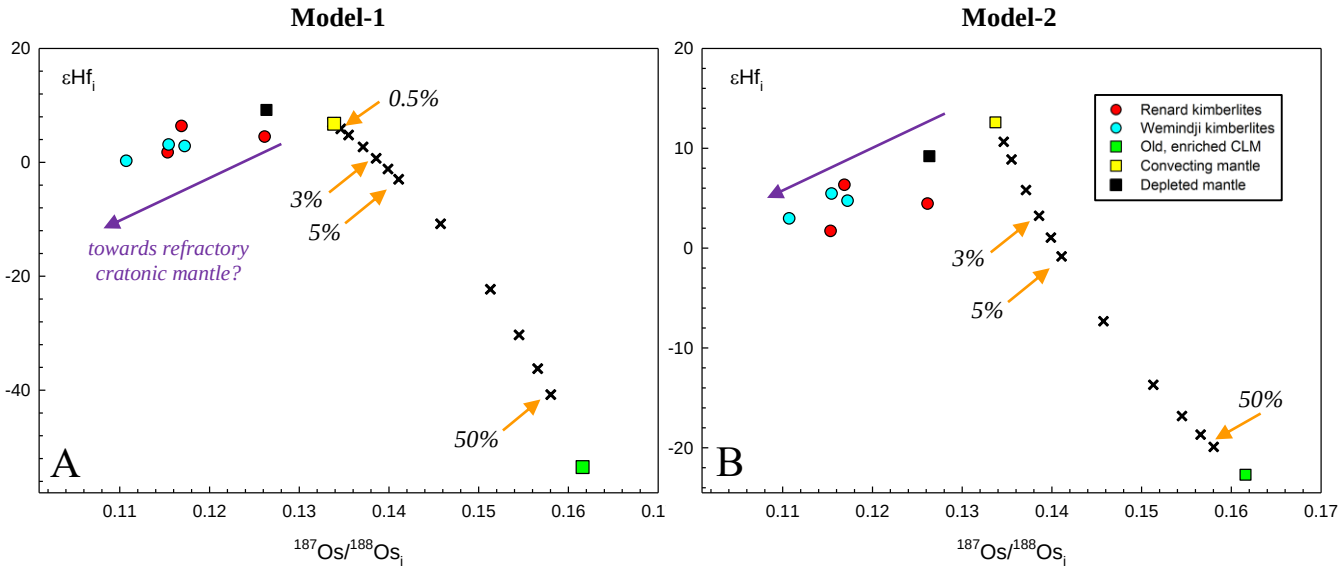

Fig. C6: Magma mixing models in Hf-Os isotope space for Renard and Wemindji kimberlites. Binary mixing curves have been constructed between an isotopically enriched olivine lamproite and an isotopically depleted carbonatite proxy. A) Model-1; B Model-2. See main text for model parameters and discussion.

APPENDIX D

GEOCHRONOLOGY

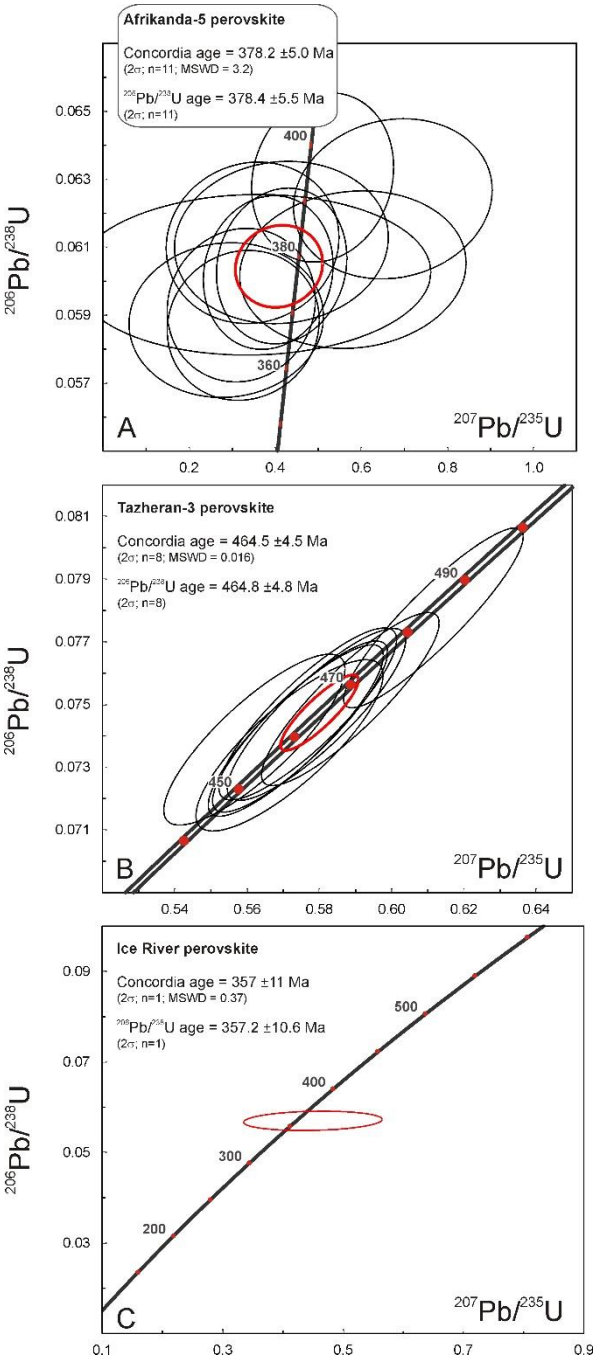

Fig. D1: U-Pb Concordia diagrams for standard samples measured with Renard kimberlite samples

Supplementary Data Table 1: SIMS U-Pb perovskite age results for hypabyssal kimberlite samples from Renard Pipe-2 and Renard Pipe-3, Superior craton, Quebec, Canada.

Sample ID / Spot#	SIMS Session	Apparent Ages (Ma)						U (ppm)	Th (ppm)	Th/U	$^{206}Pb/^{204}Pb$(m)	f_{206}%	Wetherill Concordia (TCPb corrected)					Tera-Wasserburg Concordia (TCPb corrected)				Tera-Wasserburg Concordia (TCPb uncorrected)			
		$^{207}Pb/^{206}Pb$	±σ	$^{207}Pb/^{235}U$	±σ	$^{206}Pb/^{238}U$	±σ						$^{207}Pb/^{235}U$	±σ %	$^{206}Pb/^{238}U$	±σ %	rho	$^{238}U/^{206}Pb$	±σ %	$^{207}Pb/^{206}Pb$	±σ %	$^{238}U/^{206}Pb$	±σ %	$^{207}Pb/^{206}Pb$	±σ %
Renard Pipe-2																									
WA $^{206}Pb/^{238}U$ Age = 655.8±6.0 Ma (2s)																									
RD-R2-19@1	25/26 Nov. 2014	422.2	362.5	609.2	87.5	660.7	9.7	83	3280	39.7	144.0	13.0	0.8221	18.3	0.1079	1.6	0.0848	9.266	1.6	0.0552	18.2	8.062	1.5	0.1566	1.5
RD-R2-19@3	25/26 Nov. 2014	644.4	185.0	648.6	45.4	649.8	9.3	126	4201	33.3	188.4	9.9	0.8942	9.3	0.1061	1.5	0.1625	9.428	1.5	0.0611	9.1	8.492	1.5	0.1380	1.4
RD-R2-19@4	25/26 Nov. 2014	913.1	168.6	717.7	46.2	656.7	9.5	108	7687	71.5	179.6	10.4	1.0275	8.8	0.1072	1.5	0.1724	9.324	1.5	0.0695	8.7	8.354	1.5	0.1493	1.3
RD-R2-19@6	25/26 Nov. 2014	909.9	192.8	724.5	53.6	666.1	9.7	94	10956	116.3	156.1	12.0	1.0412	10.1	0.1088	1.5	0.1517	9.187	1.5	0.0694	10.0	8.086	1.6	0.1612	1.4
RD-R2-19@7	25/26 Nov. 2014	526.5	247.4	639.5	60.2	672.0	10.3	109	11473	105.2	145.4	12.9	0.8773	12.3	0.1099	1.6	0.1306	9.102	1.6	0.0579	12.2	7.931	1.6	0.1580	1.8
RD-R2-19@8	25/26 Nov. 2014	575.3	244.2	641.5	59.9	660.5	9.5	96	8853	92.6	146.9	12.7	0.8810	12.2	0.1079	1.5	0.1233	9.269	1.5	0.0592	12.1	8.088	1.5	0.1581	1.4
RD-R2-19@9	25/26 Nov. 2014	676.4	223.2	636.1	55.0	624.8	9.2	123	11173	90.5	139.4	13.4	0.8709	11.3	0.1018	1.5	0.1362	9.826	1.5	0.0621	11.2	8.508	1.6	0.1658	1.2
RD-R2-19@11	25/26 Nov. 2014	411.9	247.4	606.4	56.6	659.7	9.4	110	10585	95.9	151.5	12.4	0.8170	12.1	0.1077	1.5	0.1246	9.281	1.5	0.0550	12.0	8.135	1.5	0.1514	1.4
RD-R2-19@12	25/26 Nov. 2014	248.0	290.6	563.4	62.0	644.6	9.3	107	11221	105.3	142.9	13.1	0.7418	13.9	0.1052	1.5	0.1085	9.510	1.5	0.0512	13.8	8.265	1.5	0.1538	1.6
RD-R2-19@13	25/26 Nov. 2014	743.1	138.1	664.4	34.7	641.4	9.2	151	10623	70.1	224.7	8.3	0.9239	7.0	0.1046	1.5	0.2147	9.558	1.5	0.0640	6.8	8.763	1.5	0.1283	1.2
RD-R2-19@14	25/26 Nov. 2014	240.9	294.2	566.9	63.1	651.4	9.3	105	11251	107.5	138.0	13.6	0.7478	14.1	0.1063	1.5	0.1065	9.404	1.5	0.0510	14.0	8.130	1.5	0.1573	1.5
Ice-River@3	25/26 Nov. 2014	502.0	212.6	377.3	33.5	357.2	5.3	140	2372	16.9	278.3	6.7	0.4500	10.4	0.0570	1.5	0.1464	17.550	1.5	0.0573	10.3	16.370	1.5	0.1096	1.9
Tazheran-3@1	25/26 Nov. 2014	493.1	15.3	484.6	6.4	482.8	7.0	6281	8819	1.4	1073.9	1.7	0.6116	1.7	0.0778	1.5	0.9074	12.860	1.5	0.0570	0.7	12.636	1.5	0.0706	0.3
Tazheran-3@2	25/26 Nov. 2014	462.2	19.4	463.9	6.5	464.3	6.7	5134	5642	1.1	855.0	2.2	0.5792	1.7	0.0747	1.5	0.8619	13.390	1.5	0.0562	0.9	13.097	1.5	0.0733	0.3
Tazheran-3@3	25/26 Nov. 2014	452.5	19.5	462.4	6.5	464.4	6.7	5081	5341	1.1	882.9	2.1	0.5768	1.7	0.0747	1.5	0.8614	13.387	1.5	0.0560	0.9	13.103	1.5	0.0725	0.3
Tazheran-3@4	25/26 Nov. 2014	462.9	23.3	459.1	6.9	458.4	6.7	4735	9932	2.1	819.6	2.3	0.5717	1.8	0.0737	1.5	0.8190	13.569	1.5	0.0563	1.1	13.260	1.5	0.0741	0.4
Tazheran-3@5	25/26 Nov. 2014	455.5	18.6	460.3	6.4	461.2	6.7	4677	5997	1.3	1039.5	1.8	0.5735	1.7	0.0742	1.5	0.8725	13.483	1.5	0.0561	0.8	13.240	1.5	0.0701	0.3
Tazheran-3@6	25/26 Nov. 2014	419.3	22.7	452.9	6.7	459.5	6.7	5017	5061	1.0	743.9	2.5	0.5620	1.8	0.0739	1.5	0.8269	13.536	1.5	0.0552	1.0	13.195	1.5	0.0748	0.4
Tazheran-3@7	25/26 Nov. 2014	483.2	17.9	470.0	6.4	467.2	6.8	4013	20375	5.1	1257.1	1.5	0.5886	1.7	0.0752	1.5	0.8791	13.303	1.5	0.0568	0.8	13.105	1.5	0.0684	0.4
Tazheran-3@8	25/26 Nov. 2014	456.3	18.7	461.0	6.4	462.0	6.7	4924	6512	1.3	962.8	1.9	0.5747	1.7	0.0743	1.5	0.8707	13.460	1.5	0.0561	0.8	13.198	1.5	0.0712	0.3

Supplementary Data Table 1 Continued: SIMS U-Pb perovskite age results for hypabyssal kimberlite samples from Renard Pipe-2 and Renard Pipe-3, Superior craton, Quebec, Canada.

Sample ID / Spot#	SIMS Session	Apparent Ages (Ma)						U (ppm)	Th (ppm)	Th/U	$^{206}Pb/^{204}Pb$(m)	f_{206}%	Wetherill Concordia (TCPb corrected)					Tera-Wasserburg Concordia (TCPb corrected)				Tera-Wasserburg Concordia (TCPb uncorrected)			
		$^{207}Pb/^{206}Pb$	±σ	$^{207}Pb/^{235}U$	±σ	$^{206}Pb/^{238}U$	±σ						$^{207}Pb/^{235}U$	±σ %	$^{206}Pb/^{238}U$	±σ %	rho	$^{238}U/^{206}Pb$	±σ %	$^{207}Pb/^{206}Pb$	±σ %	$^{238}U/^{206}Pb$	±σ %	$^{207}Pb/^{206}Pb$	±σ %
Renard Pipe-3																									
WA $^{206}Pb/^{238}U$ Age = 653.8±5.9 Ma (2s)																									
RD-11646@1	8/9 March 2012	806.5	141.7	694.3	37.1	660.1	9.4	153	426	2.8	275.2	6.8	0.9813	7.2	0.1078	1.5	0.2074	9.274	1.5	0.0660	7.1	8.679	1.5	0.1183	1.4
RD-11646@3	8/9 March 2012	956.2	205.5	737.9	58.6	668.1	9.6	68	2854	41.7	177.6	10.5	1.0683	10.9	0.1092	1.5	0.1387	9.158	1.5	0.0710	10.7	8.247	1.5	0.1515	1.7
RD-11646@4	8/9 March 2012	494.6	248.4	620.0	58.7	654.9	9.4	87	4657	53.4	171.2	10.9	0.8416	12.3	0.1069	1.5	0.1222	9.351	1.5	0.0571	12.2	8.386	1.5	0.1421	1.5
RD-11646@5	8/9 March 2012	491.1	247.2	613.1	57.9	646.6	9.3	89	1092	12.2	190.4	9.8	0.8290	12.2	0.1055	1.5	0.1231	9.478	1.5	0.0570	12.1	8.599	1.5	0.1334	1.7
RD-11646@6	8/9 March 2012	933.0	136.8	721.4	37.5	655.3	9.4	147	5967	40.6	281.7	6.6	1.0350	7.1	0.1070	1.5	0.2105	9.347	1.5	0.0702	7.0	8.760	1.5	0.1210	1.4
RD-11646@9	8/9 March 2012	590.1	243.6	636.7	59.6	649.8	9.3	94	3809	40.6	177.9	10.5	0.8720	12.2	0.1061	1.5	0.1230	9.428	1.5	0.0596	12.1	8.492	1.5	0.1412	1.6
RD-11646@10	8/9 March 2012	*infinite*	333.1	520.9	64.6	649.2	9.4	110	9375	85.3	160.9	11.6	0.6704	15.4	0.1060	1.5	0.0991	9.438	1.5	0.0459	15.3	8.401	1.5	0.1376	1.5
RD-11646@11	8/9 March 2012	629.4	282.9	642.5	71.3	646.2	9.3	92	1314	14.3	170.9	10.9	0.8828	14.5	0.1054	1.5	0.1040	9.484	1.5	0.0607	14.4	8.503	1.5	0.1455	1.7
RD-11646@12	8/9 March 2012	953.2	207.7	721.4	58.3	649.2	9.3	117	8848	75.4	221.0	8.5	1.0350	11.0	0.1059	1.5	0.1374	9.439	1.5	0.0709	10.9	8.684	1.5	0.1356	1.6
RD-11646@13	8/9 March 2012	822.5	200.0	697.5	53.5	659.4	9.4	114	650	5.7	212.1	8.8	0.9876	10.3	0.1077	1.5	0.1456	9.285	1.5	0.0665	10.2	8.512	1.5	0.1344	1.7
Afrikanda-5@1	8/9 March 2012	*infinite*	353.4	329.9	46.2	377.2	5.6	130	806	6.2	166.0	11.3	0.3839	16.0	0.0603	1.5	0.0958	16.596	1.5	0.0462	16.0	14.785	1.6	0.1351	1.6
Afrikanda-5@2	8/9 March 2012	185.7	313.0	352.5	45.4	378.3	5.7	150	783	5.2	154.4	12.1	0.4151	14.9	0.0604	1.5	0.1039	16.543	1.5	0.0498	14.8	14.603	1.5	0.1449	1.5
Afrikanda-5@3	8/9 March 2012	*infinite*	489.7	282.9	55.5	371.3	5.6	140	903	6.5	143.6	13.0	0.3213	21.9	0.0593	1.6	0.0713	16.865	1.6	0.0393	21.8	14.739	1.5	0.1429	1.9
Afrikanda-5@4	8/9 March 2012	*infinite*	489.2	286.4	56.8	367.7	5.5	146	922	6.3	174.2	10.7	0.3259	22.1	0.0587	1.5	0.0694	17.036	1.5	0.0403	22.1	15.265	1.5	0.1256	2.6
Afrikanda-5@5	8/9 March 2012	555.7	262.8	418.6	46.3	394.2	6.2	135	818	6.1	246.2	7.6	0.5103	13.2	0.0631	1.6	0.1222	15.860	1.6	0.0587	13.1	14.693	1.6	0.1177	2.3
Afrikanda-5@6	8/9 March 2012	*infinite*	716.1	255.8	75.5	368.6	5.7	137	768	5.6	158.8	11.8	0.2865	32.2	0.0589	1.6	0.0491	16.991	1.6	0.0353	32.1	15.053	1.5	0.1295	2.4
Afrikanda-5@7	8/9 March 2012	156.3	489.6	352.2	75.6	382.5	5.9	139	926	6.6	166.8	11.2	0.4146	24.5	0.0611	1.6	0.0652	16.356	1.6	0.0492	24.4	14.580	1.5	0.1374	2.7
Afrikanda-5@8	8/9 March 2012	*infinite*	917.7	302.7	136.3	376.8	5.9	105	1274	12.1	89.6	20.9	0.3473	48.7	0.0602	1.6	0.0329	16.615	1.6	0.0418	48.7	13.256	1.6	0.2075	3.2
Afrikanda-5@9	8/9 March 2012	1152.7	253.8	522.8	58.9	390.4	5.8	148	806	5.4	469.7	4.0	0.6734	14.0	0.0624	1.5	0.1103	16.019	1.5	0.0782	13.9	15.401	1.6	0.1084	4.3
Afrikanda-5@10	8/9 March 2012	921.9	338.9	464.8	71.4	377.7	5.8	133	997	7.5	178.1	10.5	0.5806	18.5	0.0603	1.6	0.0849	16.573	1.6	0.0698	18.4	14.887	1.5	0.1503	2.7
Afrikanda-5@11	8/9 March 2012	*infinite*	510.9	302.9	63.7	382.5	5.9	134	940	7.0	148.0	12.6	0.3476	23.6	0.0611	1.6	0.0673	16.358	1.6	0.0412	23.5	14.357	1.5	0.1416	1.6

U/Pb ages were calculated using Isoplot 2.2 (Ludwig, 2000); TCPB - total initial common Pb.

Uncertainties are quoted at 1-sigma except for the final age results, where uncertainties are given at the 2-sigma level; WA - weighted average.

The f_{206}% values denote the percentage of initial common ^{206}Pb on Pb mass 206 as estimated from the measured ^{204}Pb contents and the terrestrial Pb evolution model of Stacey & Kramers (1975).

Natural perovskite mineral standards (Ice River, Tazheran-3, Afrikanda-5) were analyzed as secondary reference materials to ensure accuracy of the in-situ SIMS method (Cameca IMS-1280; Li et al., 2010).

Photomicrographs of Renard hypabyssal kimberlite samples RD-R2-19 (Pipe-2) and RD-11646 (Pipe-3) are shown in Figure 3 to document the petrographic context of the analyzed groundmass perovskite grains.

References:

Li, Q.L. et al., 2010. Precise U-Pb and Th-Pb age determination of kimberlitic perovskites by secondary ion mass spectrometry. Chemical Geology, 269(3-4): 396-405.

Ludwig, K.R., 2000. Isoplot/Ex version 2.2: A geochronological toolkit for Microsoft Excel. Berkeley Geochronology Center Special Publication No. 1a: Berkeley, California.

Stacey, J.S., Kramers, J.D., 1975. Approximation of terrestrial lead isotope evolution by a two-stage model. Earth and Planetary Science Letters, 26(2): 207-221.